



UNIVERSITÀ DEGLI STUDI DI TRIESTE
XXVIII CICLO DEL DOTTORATO DI RICERCA IN
NANOTECNOLOGIE

**MORPHOLOGY CONTROL OF TIO₂-BASED
NANOMATERIALS FOR SUSTAINABLE ENERGY
AND ENVIRONMENTAL APPLICATIONS**

Settore scientifico-disciplinare: CHIM/03

DOTTORANDO
Ismael ROMERO OCAÑA

COORDINATORE
PROF. Lucia PASQUATO

Lucia Pasquato

SUPERVISORE DI TESI
PROF. Paolo FORNASIERO

Paolo Fornasiero

CO-SUPERVISORE DI TESI
PROF. Tiziano MONTINI
PROF. Juan José DELGADO JAÉN

ANNO ACCADEMICO 2015/2016

with all the love, to my daughter Milagrosa

INDEX

iii Abstract

3 1. Introduction

33 2. Methodology

63 3. Anatase/Brookite nanocomposite

97 4. TiO₂ nanosheets for photocatalytic production of H₂

143 5. TiO₂ nanosheets as a self-cleaning building materials

167 6. Conclusions

Abstract

It is unquestionable that one of the most important challenges of our society is the development of new energy strategies to tackle global warming and the exhaustion of fossil fuels generation. In this sense, it is of vital importance the production of less contaminating energy with positive effects on the reduction of greenhouse gas emissions. The conversion of solar energy into chemical energy in the form of so-called "solar fuels" as hydrogen is one of the main strategies today to solve the energy problem we face in the near future. Nanotechnology is a key area that can help solving this issue. In fact, by using the tools offered by nanotechnology, it is possible to obtain photocatalytic nanomaterials that offer solutions to these problems.

The main aim of this thesis was to design new photocatalysts based on TiO₂ with improved harvesting of visible light, which covers 43% of sunlight. The main focus of this PhD thesis was the evaluation of the effect of different transitions metals on the absorption properties of TiO₂ samples with controlled morphology (nanosheets with reactive (001) exposed facets) on the photocatalytic activity in H₂ production from biomasses and in degradation of polluting dyes. In the case of the TiO₂ semiconductors, it was paid particular attention to bi-dimensional nanocrystals to decrease the e⁻/h⁺ recombination rate and in the synergistic effect of the combination of two polymorphs (anatase/brookite). Basically the research activity carried out can be summarized as follows: synthesis of novel nanomaterials, including the preparation of metal-doped TiO₂ nanocrystal with controlled morphology; evaluation of photocatalytic acitivity under realistic conditions (bio-alcohols photo-reforming and degradation of organic compounds in self-cleaning materials) and the effect of the metal transitions in both activity and selectivity; Sub-nanometric characterization of selected photocatalysts by mean of Advanced Electron Microscopy Techniques. Throughout the duration of this experimental work, was handled many advanced characterization techniques to obtain a deeper understanding of the nature of the samples and get to explain their behavior in different photocatalytic experiments. Several techniques such as textural characterization, band-gap measures using UV-diffuse reflectance spectroscopy, XPS, ICP, XRF have been used for obtaining trial data which have

been used to obtain results. Particular attention has been devoted to the characterization of the materials by electron microscopy.



Introduction

1. Introduction

The life of human beings in today's World requires large amounts of energy, that are satisfied essentially by extensive use of non-renewable fossil fuels. The production of such relevant quantities of energy represents a global problem in relation with damages to the environment, contributing to air pollution and to the increase in carbon dioxide (CO₂) emissions. Energy-related CO₂ emissions is considered one of the main responsible of an overall increase in global temperatures, the so-called Global Warming^(1,2). Nowadays, World population is approaching 7.5 billion of human beings, with an average annual growth around 1.3%. The 95% of the increase in world population will occur in developing countries during next years. In this scenario, the energy demand of our society will increase year by year^(3,4). It is unquestionable that one of the most important scientific and technological challenges of our society is the development of new energy strategies to satisfy the increasing energy demand in a sustainable way, tackling global warming and exhaustion of fossil fuels^(3,5,6).

In this context, heterogeneous photocatalysis has attracted great attention in the scientific community for the development of efficient materials able to promote the valorisation of alternative feedstocks (such as biomass-derived compounds) into high added value compounds (i.e. fuels) by the efficient exploitation of Sunlight.

Sunlight is one of the most abundant renewable and clean energy sources in the world. For this reason, the scientific community has great interest in developing suitable ways to harvest this renewable energy and to store it, in order to deliver this energy when Sunlight is not available or during maxima in energy requirements. In the Figure 1.1 is illustrated the solar radiation spectrum over atmosphere and sea level. At the surface of the Sun the intensity of the solar radiation is about $6.33 \times 10^7 \text{ W/m}^2$. The solar constant is the average extraterrestrial insolation at the edge of the atmosphere, which value is 1367 W/m^2 and is commonly called ISC. Taken into account that the Earth presents a disc of area nR^2 to the Sun, the total amount of extraterrestrial insolation incident on the Earth is $I_{sc} \times nR^2$. This value is then divided by half the surface areas of the Earth, $4nR^2/2$, which gives 684 W/m^2 . The distribution of the solar irradiation is UV (200-400nm) 8.7%, Visible (400-700nm) 38.3% and IR (700-3500nm) 51.7%.

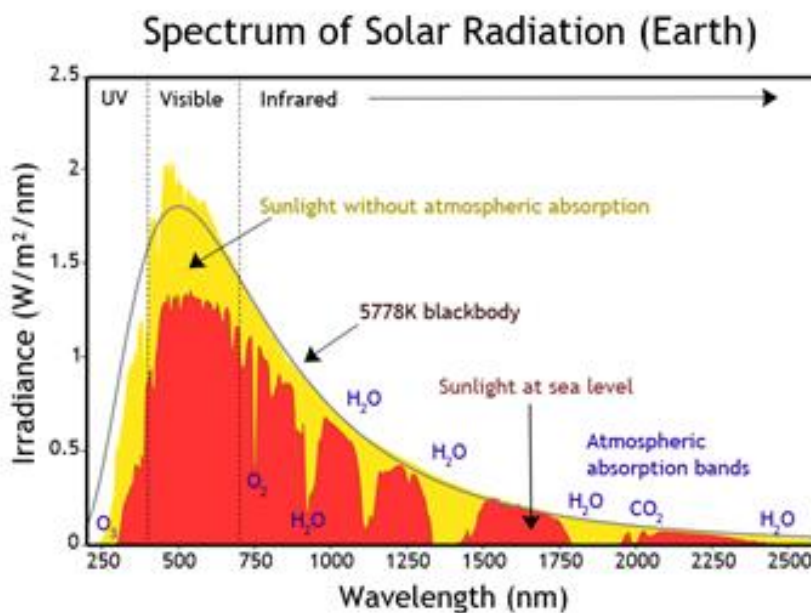


Fig.1.1 Solar radiation spectrum over atmosphere and sea level

The conversion of solar energy into chemical energy in the form of so-called "solar fuels" is one of the main strategies today to solve the energy problem we face in the near future⁽⁷⁻¹²⁾. Among them, particular attention is devoted to the sustainable production of H₂, in view of its large use in chemical industry and of the potential use as energy vector.

Likewise, if it were to desired remove accumulated contamination on the stones of the buildings or monuments, produced by hundreds of chemical compounds (that contain among others, NO_x, CO, and volatile organic compound (VOC)) that are emitted directly or indirectly into the atmosphere due to industrial and urban activities, this had to be done by application of a technique that involve high temperatures, with the cost than that would suppose. These techniques of thermal combustions of VOCs is applied in the pollution source, no directly to the monuments and try to purify the air that go directly to the atmosphere. These VOCs present in the air are the responsible of the monuments deterioration. The heterogeneous photocatalysis appears not only for the production of clean and renewable energy but also as an activator of photocatalytic reactions that would otherwise require significant energy input. In this context, heterogeneous photocatalysis has a crucial role.

1.2 Heterogeneous photocatalysis

Since the discovery of electrochemical photolysis water splitting to produce H₂ on TiO₂ by Fujishima and Honda in 1972⁽¹³⁾ (this meant a breakthrough in the field of semiconductor materials), extensive research has been carried on photocatalysis field.

Heterogeneous photocatalysis can be defined as the acceleration of a chemical reaction by action of a solid catalyst, activated by electronic excitation when energy in the form of light falls on the semiconductor, e.g. TiO₂, ZnO, etc. The main difference from conventional catalytic techniques is therefore that in the conventional catalytic techniques the activation process is thermal; it is an

enormously expensive process. That makes the photocatalysis be a less expensive and environmentally friendly technique.

1.2.1 The photocatalytic process

A semiconductor is a crystalline solid characterized by peculiar electronic properties. In the electronic band structure typical of solid materials, a distinct separation between the higher filled band (called valence band, VB) and the lower un-occupied band (called conduction band, CB). The energy difference between VB and CB edges represents the so-called band gap (E_g). When photons with an energy equal or larger than the E_g are absorbed by the semiconductor, an electron (e^-) is promoted into the CB, leaving a hole (h^+) in the VB. This charge separation induces a redox potential within the semiconductor material, with holes having oxidant capacity and electrons taking part in reduction reactions. This process is illustrated in the Figure 1.2.

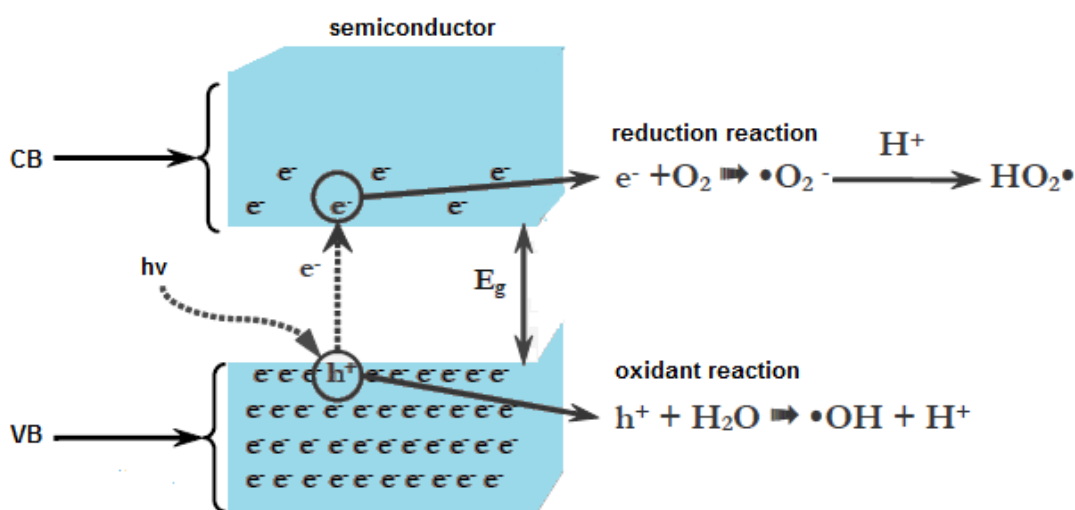


Fig.1.2 Photocatalytic process in heterogeneous photocatalysis. Exited electrons (e^-) participate in the reduction semireactions and holes (h^+) participate in the oxidant semireactions.

The most part of electron-hole pairs formed by irradiation recombine by annealing processes, in the form of heat (non-radiative recombination) or in some cases with a photoemission (radiative recombination). Considering that in

semiconductors materials the mean lifetime of the e^-/h^+ pairs is of the order of nanoseconds⁽¹⁴⁾, which means in the timescale of electron transfer during chemical reactions, the e^-/h^+ pair can react with the molecules adsorbed on the semiconductor surface, promoting non spontaneous redox processes.

The photocatalytic research in the last years have been focused in the use of new strategies to avoid the e^-/h^+ recombination with the use of traps or e^- or h^+ acceptors. The most common method is loading a photocatalyst with a co-catalyst, as will be pointed out below. In any case, independently of the greater or lesser likelihood of recombination, the reaction can take place only when the reduction potentials of the donor (donor is a dopant atom that, when added to a semiconductor, can form a n-type region) and acceptor (an acceptor is a dopant atom that when added to a semiconductor can form a p-type region) are inside of the region between the VB and CB edges.

1.2.3 Semiconductors used in heterogeneous photocatalysis

A variety of materials with suitable properties to act as photocatalyst has been already reported in the scientific literature, such as TiO_2 , ZnO , CdS , WO_3 , ZnS , iron oxides, etc. These materials have a low cost and can be excited with light of relatively large wavelengths, enabling to absorb part of the solar radiation that comes to the Earth surface ($\lambda > 310nm$) as a clean energy source, with the obvious environmental and the economic benefits.

From a practical point of view, interesting semiconductors materials must possess a band-gap within the energy interval of the solar spectrum. Some examples of adequate materials are represented in the Figure 1.3. In a photocatalytic process, photogenerated holes are able to oxidize only the redox couples having a reduction potential correspondent to an energy higher than the VB edge. At the same time, photogenerated electrons are able to reduce only the redox couples having a reduction potential correspondent to an energy lower than the CB edge.

Moreover, ideal photocatalysts have also to be chemically stable against photocorrosion, non-toxic, largely available and cheap.

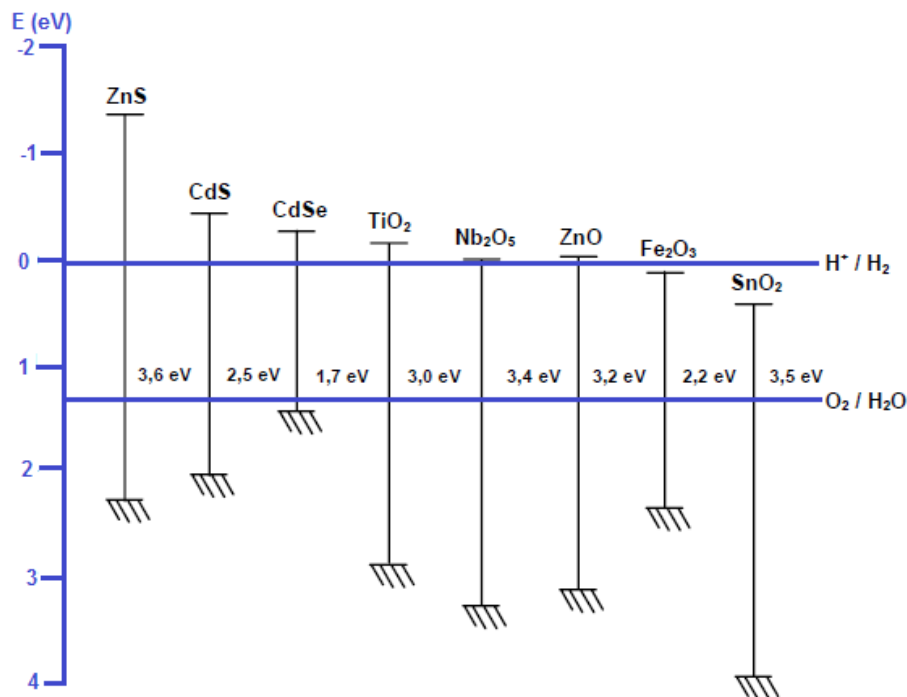
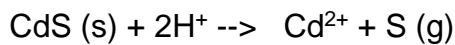


Fig.1.3. Energy of VB and CB edges and values of E_g for several common semiconductors, compared to the energies correspondent to the redox potential at pH = 0 of the couples involved in water splitting^(15–17).

From Figure 1.3, it can be appreciated that CdS has the best value of VB and CB edge energies for solar water splitting. Selenides as sulphides are usually quite vulnerable to the oxidative action of impurities or of the treatment medium. CdS, for example, gradually decomposes under irradiation because the generated charges have a high tendency to participate in the following reaction⁽¹⁸⁾:



Although band-gap energy is not optimal for an efficient harvesting of Sunlight, TiO_2 possesses high resistance to light-induced corrosion. Coupled with its low cost and low toxicity, its high chemical stability makes this semiconductor material one of the most suitable for application in heterogeneous photocatalysis.

1.3 Titanium dioxide (TiO_2) as a photocatalyst

The properties of TiO_2 have been widely explored theoretically and experimentally because of its photocatalytic properties, which make this semiconductor material, be a good candidate to be used as photocatalysis for energy conversion and self-cleaning applications. TiO_2 is a photosensitive semiconductor where its valence electrons are excited into the conduction band by high-energy radiation in the ultraviolet (UV) range (200nm-400nm), that represents less than 5% ⁽¹⁹⁾ of the total energy in the solar spectrum. In recent years, great effort has been done to increase the photosensitive response of the TiO_2 in the visible range of the spectrum ^(19–21), since this represents the major part of the solar energy incoming to the Earth's surface (approximately 45%).

TiO_2 can be present in many polymorphs. Among them, anatase, rutile and brookite are the most stable. Anatase and rutile are the phases of TiO_2 more commonly used in photocatalysis, the first one generally being the most active. This can be attributed to two reasons: its Fermi level is located approximately 0.1 eV above rutile, and the higher concentration of superficial hydroxyls, which can produce more OH^- .

The crystal structure of the different TiO_2 polymorphs are based on the octahedral coordination of Ti^{4+} ions surrounded by six oxygen ions O^{2-} , these being in turn bonded to three atoms of titanium in a trigonal configuration. Depending on how the connections between the octahedral units are established, the three crystal modifications mentioned above can be obtained. In anatase phase, whose space group is $I\ 4_1/\text{amd}$, each titanium ion in anatase

is coordinated by six oxygens, and each oxygen ion by three titanium atoms. The TiO_6 octahedra share edges with four adjacent octahedra. In rutile phase, whose space group is $\text{P}42/\text{mnm}$, crystallize in the tetragonal system and as anatase and brookite phases, have Ti^{4+} cations coordinated by six O^{2-} anions. In rutile phase, these TiO_6 octahedra are linked by edges to form chains parallel to the z-axis. Brookite, whose space group is Pcab , crystallizes in the rhombic system and is an orthorhombic unit constructed by an octahedron of oxygen ions arranged about a single titanium ion. Each octahedron shares three edges with adjoining octahedra.

The photocatalytic activity of the TiO_2 phases is different. This is justified by the difference in the crystal lattice, which cause differences in electronic states. These differences translate into differences in the band gap. For solid materials, anatase has a band gap of 3.2eV, 3.02 eV for rutile and 3.13 eV for brookite. These energy levels correspond to UV radiation 380-376nm and 400-410nm for anatase and rutile respectively.

Among the remarkable properties of TiO_2 , the following would to be particularly noteworthy:

- chemical stability: TiO_2 is degraded only in the presence of concentrated HF or H_2SO_4 . At high temperature the atoms of Ti^{4+} can be reduced to Ti^{3+} by means of reductants like CO, NH_3 or H_2 ; process that is associated to a change in the colour, from the characteristic white to grey/black;
- high resistance to the photocorrosion: only in strongly acid medium, in the presences of sulphates ions, has been detected a significant degradation of TiO_2 under irradiation⁽²²⁾ .
- The TiO_2 surface is polar and therefore is hydrophilic. That means that in contact with H_2O , this is chemisorbed and dissociated, causing the superficial hydroxylation of TiO_2 , generating OH^- groups with different grades of reactivity in function of their localization. This property is particularly interesting in photocatalytic reactions for environmental remediation and pollutant degradation.
- high dielectric constant ($\epsilon > 100$) and refractive index ($n = 2.54$ for anatase and 2.75 for rutile, at $\lambda = 550$ nm).

Because of the above described properties, TiO_2 became one of the most used active materials in heterogeneous photocatalysis, in addition to others technological fields. However, TiO_2 has some disadvantages that reduce the efficiency of the photocatalytic reactions, such as high recombination rate of the e^-/h^+ pairs and the low absorption in the visible spectrum region. To overcome these problems, several strategies aimed to achieve an increase in the photocatalytic activity of the TiO_2 have been proposed, that can be summarized as follow:

- a)** doping with anions/cations in order to introduce intra-gap energies levels;
- b)** the formation of composite materials with a second semiconductor, a carbon-based nanostructure or metal nanoparticles (both noble and non-noble metals have been used);
- c)** crystal facet engineering by developing new strategies of synthesis: obtaining well-defined structures, the less thermodynamically stable (and more reactive) crystal facets are exposed and accumulation of e^- and h^+ takes place on different facets, improving their lifetime;
- d)** with the sensitization of the TiO_2 with organic dyes in order to increase the response in the visible light.

In the present work have been used the first three strategies, that it is going to discuss in next paragraphs.

1.3.1 Effect of transition metals as dopants in TiO_2

In order to increase the visible response of TiO_2 , several works of doping TiO_2 with transition metal have been reported. The band-gap is one of the principal variables that affect the photocatalytic efficiency of TiO_2 . The introduction of ions into the TiO_2 lattice could significantly influence the photoreactivity, in the charge recombination rates and in the interfacial electron-transfer rates but at the cost of reduced thermal stability. Because the unique d configuration of transition metals is the most effective to improve the absorption edge of TiO_2 to visible light region, which either inserts a new band level into the original band gap or can modify the CB or VB, the Figure 1.4 illustrates the effect of transition metals in TiO_2 .

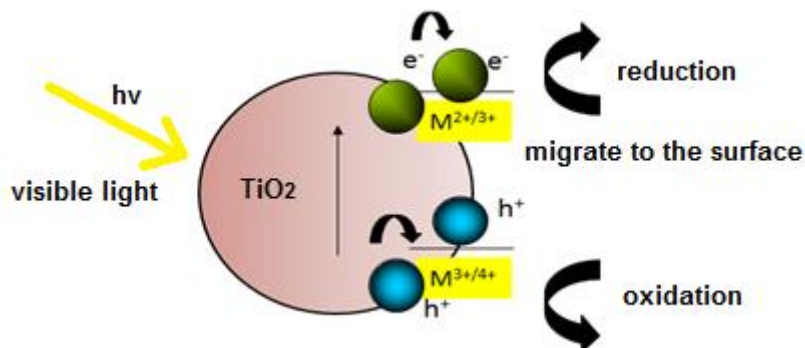


Fig.1.4 Band-Gap modification by doping with a transition metal (Fe, Mn, Co, Ni and Cu) create new energy levels in the band gap.

A key issue in this topic is to develop reliable doping procedures. It is extremely difficult to be modified once the lattice has been formed because ionic radius of Ti^{4+} is very small, therefore, TiO_2 can accommodate very small amount of doping cations independently from the polymorph considered. Another key issue is that for most of the material in which metal doping shows some type of photoresponse difference for pure TiO_2 , is not clear evidence that the metal doping is in the TiO_2 lattice. In addition, all the doping metals can undergo photocorrosion during the photocatalytic reaction, but is difficult to have photocorrosion if the dopant is within the TiO_2 lattice. The leached dopant ions reasonably come from metal oxide outside the lattice. In this sense is a key issue provide convincing characterization data to show that the doping metal is in the TiO_2 lattice. The characterization of the fresh dopant metals (Mn, Fe, Co, etc.) is not sufficient and characterization of the photocatalyst after the photocatalysis reaction is necessary to show that no changes have occurred. On the basis of the theoretical (23–25) studies and experimental results (26–29), it is unquestionable the effectiveness of TiO_2 doping with transition metals ions to improve the photoresponse of the semiconductor in the visible region of the electromagnetic spectrum. But nowadays still is a challenging to improve the absorption of the TiO_2 in the visible region and research in this field is ongoing. Theoretical work is much needed in this area to gain understanding on mechanism of the process and how it becomes influenced by metal doping.

1.4 The effect of co-catalyst on TiO₂

One of the principal problems that make that a photocatalytic system does not work well, is the fast recombination of the e/h⁺ pairs, diminishing the photocatalytic activity. A suitable co-catalyst is indispensable for achieving high efficiency in photocatalysis.

A co-catalyst can provide reduction or oxidation active sites, catalyse the surface reactions by lowering the activation energies, trap the charge carriers, and suppress the recombination of photogenerated electrons and holes. An efficient co-catalyst should be in concordance with the semiconductors in terms of energy levels and electronic structures; that is, the co-catalyst and light harvesting semiconductor should have compatible lattice and electronic structures with suitable Fermi-levels or band levels.

The trapping ability is largely determined by the work functions of the noble metals, which are greater than those of many semiconductors. In the TiO₂ a Schottky barrier can be formed at the metal/TiO₂ interface. Schottky barrier is a kind of junction which can facilitate charge separation. Noble metals with larger work function that is, lower Fermi level, should more readily trap electrons. Thus, Pt, among many noble metals the one with the largest work function (5.12-5.93 eV), is the best candidate co-catalyst for trapping electrons. The work function is not a characteristic of a bulk material, but rather a property of the surface of the material. That means that in Pt, the electrons transfer from the CB of semiconductor to metal readily happens. In this sense, Pt can trap the photogenerated electrons of the TiO₂ leading to efficient charge separation^(30,31). Additionally, Pt has the lowest activation for proton reduction^(30,32) that means that Pt not only act as electron trap, also provides effective proton reductions sites, hence dramatically facilitates proton reduction reaction.

1.4.1 Optimal amount of co-catalyst

The introduction of a co-catalyst onto a semiconductor could gradually enhance the photocatalytic (Figure 1.5). When the loading amount of a co-catalyst on a semiconductor reaches the optimal value, this co-catalyst/semiconductor system achieves the highest activity. However, further loading of the co-catalyst will drastically decrease the photocatalytic activity. This decrease is caused by the following factors⁽³³⁾:

- (i) High co-catalyst loading amount could result in over-coverage of the surface, blocking the active sites of the semiconductor;
- (ii) Excessive loading of co-catalyst on the surface of semiconductors could block the incident light;
- (iii) Co-catalyst at high loading amount could act as charge recombination centres, resulting in the decrease of the photocatalytic activity

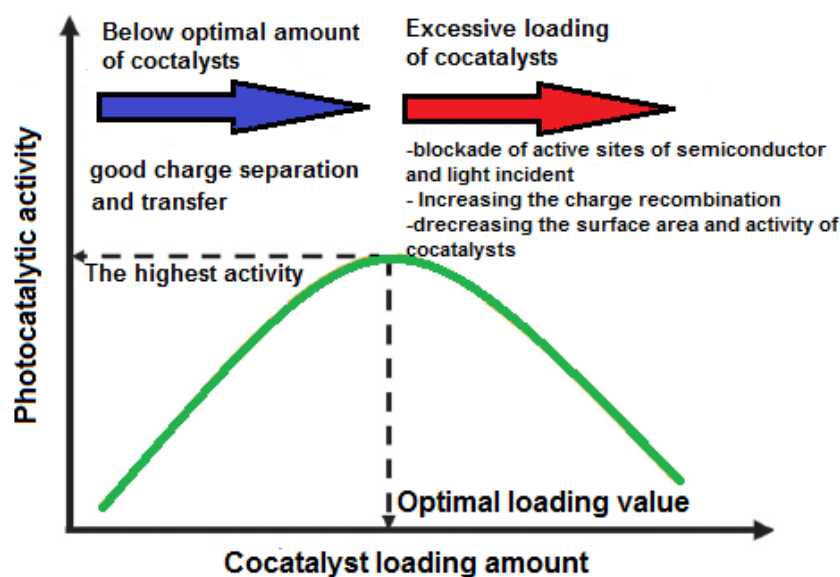


Fig.1.5 Relationship between the loading amount of a co-catalyst and the photocatalytic activity of the co-catalyst loaded semiconductor photocatalyst. Figure adapted from reference⁽³³⁾.

Another important factor influencing the catalytic activity of co-catalyst is their size. Normally, at the same loading amount, co-catalysts with smaller size

have a larger surface area and more active sites, which result in higher catalytic activity.

1.5 Hydrophilicity and hydrophobicity: effect in the photocatalytic activity

The hydrophilicity of the material has an important effect ^(34,35) in the photocatalytic activity as it will see in the experimental result of this thesis. The wetting of a solid with H₂O, where air is the surrounding medium, is dependent on the relation between the interfacial tensions (water/air, water/solid and solid/air). The ratio between these tensions determines the contact angle θ between water droplets on a given surface. A contact angle of 0° means complete wetting, and a contact angle of 180° corresponds to complete non-wetting. Hydrophobic surfaces with low wettability and contact angles of about 100° are known for a long time. The higher this angle the lower is the value of the adhesion work. Decreasing of the contact angle leads to enlarged values of the adhesion work (hydrophilic surfaces)⁽³⁴⁾. The water-repellent surfaces indicate self-cleaning properties. This effect was studied by *Barthlott et al.*⁽³⁶⁾ that investigated and proved the correlation between the microstructure, wettability and contaminants in detail using lotus leaves.

If TiO₂ of the anatase phase is exposed to UV light very low contact angles are obtained (< 1°). These materials have the unique property of “attracting” rather than repelling water (super-hydrophilicity). UV illumination of TiO₂ leads to the formation of powerful agents with the ability to oxidize and decompose many types of bacteria, organic and inorganic materials.

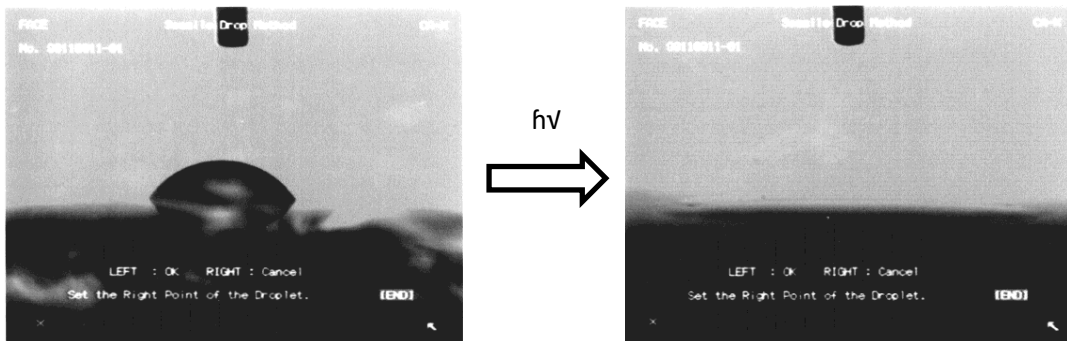


Fig. 1.6 Pictures collected during contact angle measurements, showing changes of water contact angles of TiO₂ thin film surfaces before and after UV illumination (20 mW/cm²) for 1 h under ambient conditions. UV illumination turned the water contact angles TiO₂ thin film from 54 to 0°.

In the Figure 1.6 it is possible to see the effect of the contact angle of a drop of H₂O on a thin film of TiO₂ and to examine the visible light photoinduced hydrophilicity. It is still not clear whether visible light irradiation could influence such phenomenon⁽³⁷⁾, similarly to photocatalytic properties of TiO₂.

1.6 Crystal facet engineering

The design and controlled fabrication of nanostructured materials with controlled morphologies has emerged in last years as an important strategy to maximize the photocatalytic reactivity. In the process of heterogeneous photocatalysis with a semiconductor as photocatalyst there are involve three steps: the excitation, bulk diffusion and surface transfer of photoexcited e⁻/h⁺ pair. The surface atomic structure of the photocatalyst has an undeniable influence in the reactivity since the atomic arrangement of the exposed surfaces determines the adsorption of the reactant molecules, surface transfer between photogenerated electrons and holes and reactant molecules, and desorption of product molecules. The most important reason to prepare morphologically controlled semiconductors is the accumulation of electrons and holes on different facets on the nanocrystals, improving their lifetime.

The concept of the crystal facet engineering is represented on Figure 1.7. The crystal growth process takes place by continuous accumulation of the constituents of the material on the external surface of an initial nucleus. The growth of the crystal is basically driven by the decreasing the total surface energy of crystal, finally reaching the minimum surface energy point. The density, size concentration and surface chemistry of the resulting crystalline particles are highly dependent on the growth environment ⁽³⁸⁾. Impurities and additives present in solutions that influence the ultimate shape of the crystals are called surfactants or capping agents. In a solution without capping agents, the crystal will grow exposing the most thermodynamically stable facets, which means the facets with the lower surface energy. When a capping agent is added to the growth solution, it will adsorb on specific facets of the crystal, which results in a change in the surface energy of the facets. The surface affinity of the capping agent for the crystal facets with various orientation is different. The preferential adsorption of capping agents on a specific facet hinders the accumulation of the constituents of the material on those facets. As a result, growth of the crystal is possible by deposition of material only on the facets where capping agents are not adsorbed. At the end of the crystal growth process, the final crystals will expose only the facets on which capping agents are adsorbed. Therefore, the habit of a crystal can be engineered via modulation of the solvent-capping agent in which the crystal growth takes place.

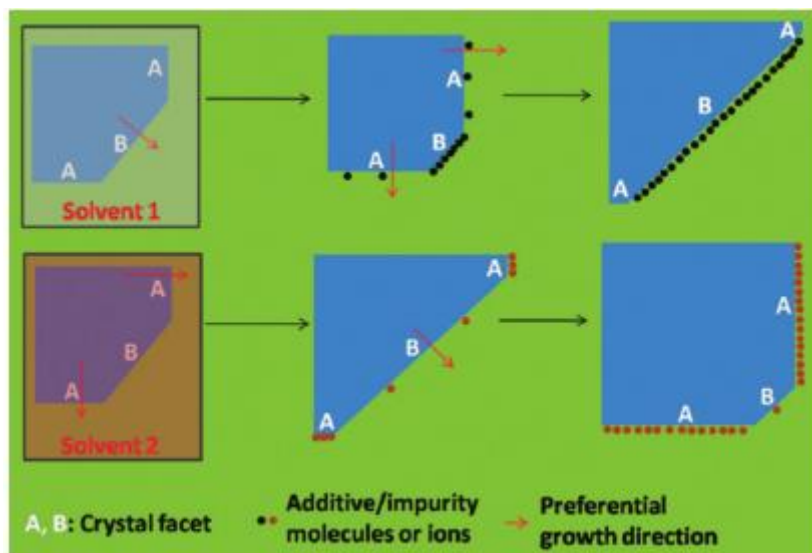


Fig.1.7. The impurity/additive effect in controlling the shape of the crystal is represented. The introduction of additive/impurity results in a different growth orientation⁽³⁸⁾.

1.6.1 Crystal facet engineering of TiO₂

Crystal facet engineering has been applied for the synthesis of well-defined TiO₂ nanoparticles^(39–42). The obtainment of TiO₂ nanocrystals with controlled morphology favours the e⁻/h⁺ pair separation due to electrons and holes are accumulated in different facets. In this sense advanced TiO₂ nanoarchitectures have been engineered as photocatalyst, such as, nanorods, nanosheets, etc.

The energy of the terminating surface of a solid is always higher than that of the bulk and this energy difference is defined as the surface energy. The Wulff construction uses the surface energy of all facets of the materials to determine the equilibrium morphology. The Wulff construction is a method to determine the equilibrium shape of a crystal of fixed volume inside a separate phase (usually its saturated solution or vapour). Energy minimization arguments are used to show that certain crystal planes are preferred over others, giving the crystal its shape. The equilibrium shapes of crystals of the most common TiO₂ polymorphs (anatase, rutile and brookite) are represented in Figure 1.8. The Wulff construction⁽⁴²⁾ predicted that the equilibrium shape of an anatase crystal is a truncated tetragonal bipyramid formed of eight (101) facets and two (001) facets. The (010) facets do not appear in the equilibrium shape of anatase. For

rutile, the predicted equilibrium shape of a macroscopic crystal was constructed with (110), (100), (001) and (011) facets. The equilibrium shape of brookite crystal exposes (111), (210), (010) and reconstructed (001) facets, with the (210) facet (one of the most stable surface of the brookite) having similar structure to the most stable facet (101) of anatase. But they show differences in electronic states which result in different chemical reactivity.

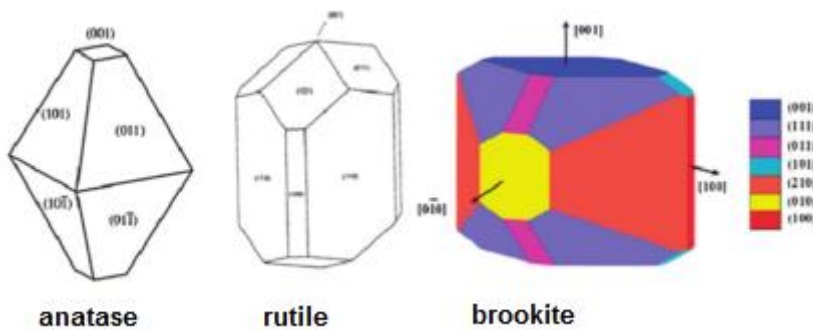


Fig.1.8 The equilibrium shape of a TiO_2 crystal according to the Wulff construction ⁽⁴²⁾.

1.6.2 Anatase TiO_2 nanosheets with a large percentage of (001) facets

It is not doubt that TiO_2 nanosheets with a large percentage of (001) facets has become very interesting synthesis since Yang *et al.* realized the first synthesis of 47% (001) in uniform crystals⁽⁴²⁾.

The study carried out by the cited article concludes that fluorine atoms are the most effective to produce a change in the surface energy of the TiO_2 during the crystal growth (Figure 1.9). The HF is used as shape controlling agent, having two roles during the hydrothermal synthesis of TiO_2 anatase nanosheets: to retard the hydrolysis of the titanium precursor and to reduce surface energy of (001) facets promoting the isotropic growth along the [010] and [100] axes⁽⁴³⁾.

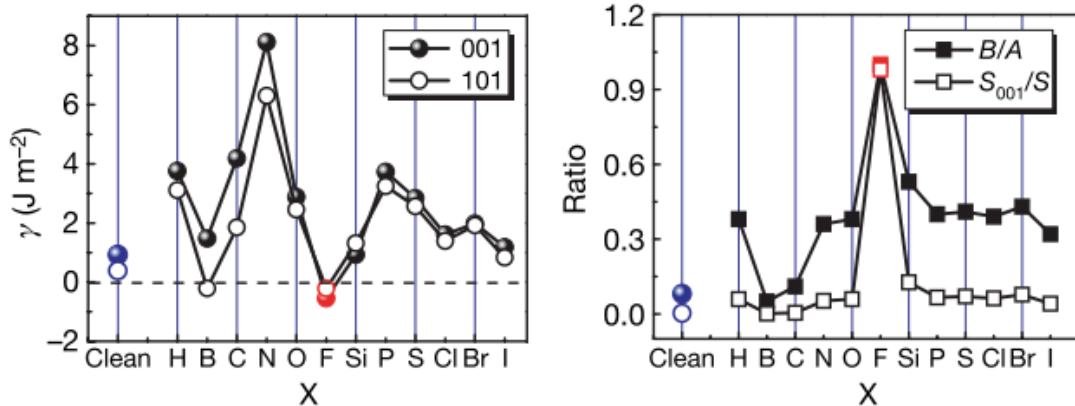


Fig.1.9 Calculated energies of the (001) and (101) surfaces surrounded by X atoms (A) and Plots of the optimized value of B/A and percentage of {001} facets for anatase single crystals with various adsorbate atoms X (B)⁽⁴²⁾. (A and B denote lengths of the side of the bipyramid and the side of the square e {001} ‘truncation’ facets, respectively)

During this synthesis, some agglomerates and/or irregular particles without defined shape appeared. To avoid this, 2-propanol (2-PrOH) is used as solvent instead of H_2O , acting as synergistic capping agent together with HF allowing the synthesis of high quality TiO_2 anatase single crystalline nanosheets. 2-PrOH tends to heterolytically dissociate forming an alkoxide group ((CH_3)₂CHO-) bound to coordinatively unsaturated Ti^{4+} cations on the (001) and (101) surfaces. The higher density of 5-fold Ti on (001) surfaces leads to selective adhesion of 2-PrOH, retarding the growth of anatase TiO_2 single crystals along [001] direction. The percentage of (001) facets can well be tuned by controlling the concentrations of precursors and fluorine species, also the synergistic effects of other capping agents^(44,45).

1.6.3 Brookite/Anatase TiO_2 nanocomposites with polyhedral morphology

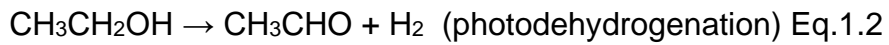
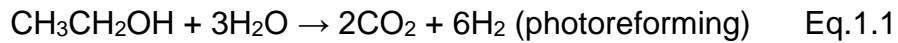
Li et al. ⁽⁴⁶⁾ used Na-Titanate nanotubes as precursor to prepare uniform tetragonal faceted nanorods with large percentage of (010) facets by a hydrothermal process in basic solution. In the present work, anatase/brookite with polyhedral morphology nanocomposites was synthesized inspired in the work of Li et al. Anatase/brookite nanocomposites were synthesized by

hydrothermal transformation of the dry Na-titanate precursor. In this sense were obtained well defined TiO_2 with nanorods morphology and with a mixture of anatase/brookite phase. The phase mixture is known to have synergistic effects and an increased photocatalytic activity is observed compared to pure phases. Several studies^(47–49) indicate that the co-presence of different phases in the TiO_2 catalysts tends to ease the charge separation. This phenomenon is associated with the electron transfer between phases, meanwhile the generated holes are confined in the respective grain wherein were generated. A well-known example is P25, which is a commercial TiO_2 powder with 75% of anatase and 25% of rutile. With illumination of ultraviolet (UV) light on P25, photoexcited electrons from the anatase phase will be transferred to the rutile phase due to lower conduction band energy of the rutile phase and thus inhibiting charge recombination. With much of the research focusing on the photocatalytic activities of anatase/rutile mixture, less attention has been paid to anatase/brookite mixture or rutile/brookite mixture due to the difficulty in synthesizing brookite TiO_2 phase⁽⁵⁰⁾.

1.7 Application of heterogeneous photocatalysis for H_2 production by means of TiO_2 as photocatalyst

The production of H_2 by means of sunlight and a semiconductor such as TiO_2 is the green alternative to solve the problem of obtain a clean energy source. The recent rejuvenation of this field has led to further exploration of new materials and new reactions to produce H_2 by means of photocatalytic reactions. One of the most intense research activities on this topic is centred in the ethanol photoreforming (eq.1.1) and ethanol photodehydrogenation (eq.1.2). The photocatalytic production of H_2 of the present work is focused in the ethanol photodehydrogenation. Because ethanol is a biomass source^(51–53) produce on a mass scale in the industry from the fermentation of plant materials such as corn, sugar cane, or grasses this method is a valid alternative to enhance process sustainability and produce H_2 using renewable energy.

In this sense the H₂ production by this technique can reduce the oil dependence and greenhouse gas emissions and help to the H₂ transition economy.



1.8 Heterogeneous photocatalysis for Self-Cleaning application on buildings materials

In the last years the deterioration of historic buildings and monuments is one of the problems with more sensitization and awareness in society nowadays. The buildings and monuments are subject to the continuous action of the atmospheric agents (mechanical action), animals and plants (biological action), and all compounds found in the surrounding atmosphere and they can interact with them (chemical action). Hundreds of chemical compounds are emitted directly or indirectly into the atmosphere due to industrial and urban activities. These air pollutants, that contain among others, NOx, CO, and volatile organic compound (VOC), are ultimately transferred to buildings, monuments and statues exhibited outdoors, act as atmospheric chemicals reservoirs. The incorporation of TiO₂ in the form of nanocoatings in the materials building can avoid the degradation of the buildings or cultural heritage by mean of a photocatalysis reaction. In photocatalysis, light energizes a mineral, triggering chemical reactions that result in the breakdown of organic matter at the molecular level, producing primarily carbon dioxide and water as by-products, as can been seen in the figure 1.10.

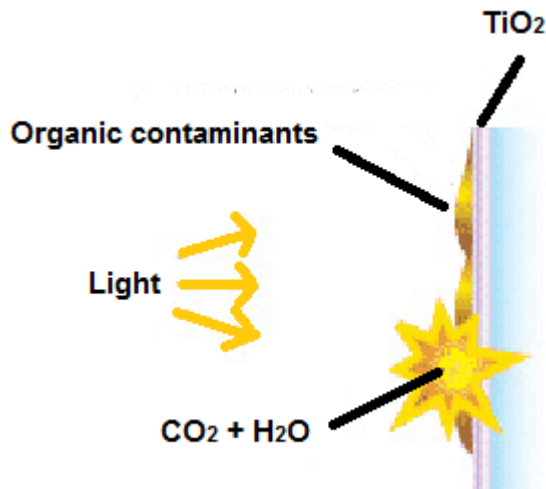


Fig.1.10. Self-Cleaning process. Photo-oxidation and decomposition of organic matter into CO_2 and H_2O .

When light and heat fall into the treated building surface, TiO_2 uses that energy to break down the dirt into molecules like O_2 , H_2O , CO_2 , NO_x , and VOCs. Gases float away, while liquids or solids are left on surface to be washed away by rain. The promising results of TiO_2 self-cleaning activity obtained on laboratories has increase the research in this field in order to develop new buildings materials in which the TiO_2 is the main component.

1.9 Aims and thesis outline

Photocatalysis has a great potential as environmental remediation and renewable energy applications. The promise of the photocatalysis is in its ability to use solar energy to produce energy in the form of chemical energy (H_2O to H_2 or CO_2 to organic compounds) or degrade pollutants of several environments such as air or water. In this sense, in last years an intensive research has been done in the field of photocatalysis in order to obtain efficient photocatalyst system. Due to that, TiO_2 is the most commonly photocatalysts used because its chemical stability, low cost and nontoxicity. The present thesis is an experimental work of the application of heterogeneous photocatalysis in energy

production and environmental remediation. It focuses on TiO_2 materials with defined morphologies, namely nanorods and nanosheets. Therefore, the present work is composed of the following chapters.

First in *Chapter 2* is described all the experimental techniques that have been used along the research work just like the entire chemical reactive employed for the synthesis of TiO_2 nanomaterials. Is this chapter is described in deep the technical aspects of the used systems and the experimental conditions in which were carried out all the experiments and measurements.

In *Chapter 3*, TiO_2 nanocomposite with anatase/brookite composition was synthesized by hydrothermal treatments. The composition of the anatase/brookite nanocomposite was tuned by changing precursor/water mass-to- volume ratio and the duration of the hydrothermal treatment. The obtained materials presented well crystallized particles with polyhedral morphology. The influence of the anatase/brookite ratio in the photocatalytic activity in H_2 production by photodehydrogenation of ethanol and its effect in the particle size of the Pt used as co-catalyst was researched. The results are related with the favoured electron/hole separation obtained with the use of multiphasic TiO_2 materials.

In *Chapter 4*, TiO_2 anatase nanosheets with high percentage of (001) exposed facets were synthesized by hydrothermal method. To obtain the desired morphology, HF was used as capping agent and in order to increase the photocatalytic response in the visible light, the synthesized material was doped with transition metals. Furthermore, to improve the photocatalytic activity, Pt was photo-deposited as co-catalyst. The synthesized photocatalyst was used to studied the photocatalytic activity in H_2 production by photodehydrogenation of ethanol and the effect of the amount the F^- ion present in the photocatalysts, the influence of the metal doping, the amount of transition metal in the photocatalyst were studied with detail, correlating with photocatalytic activity.

In Chapter 5, we employed the TiO_2 nanosheets to synthesize mesoporous $\text{TiO}_2\text{-SiO}_2$ photocatalytic coating. The coating was applied on limestone to evaluate its effectiveness in photocatalytic degradation of

atmospheric pollution in buildings materials. We have varied the loading of the TiO₂ nanoparticles in order to investigate the effect in the photocatalytic activity. Furthermore, of the loading factor, was evaluated the influences of the amount of F⁻ ion present in the TiO₂ nanosheets. To complete the study, we compare the obtained results of our photocatalyst with the commercial P25 photocatalyst, giving interesting results.

The thesis will conclude with *Chapter 6*, that correspond with the conclusions of the present work carried out and with the future perspective in the studied field.

References

1. Lashof DA, Ahuja DR. Relative contributions of greenhouse gas emissions to global warming. *Nature*. 1990 Apr 5;344(6266):529–31.
2. Meinshausen M, Meinshausen N, Hare W, Raper SCB, Frieler K, Knutti R, et al. Greenhouse-gas emission targets for limiting global warming to degrees C. *Nature*. 2009 Apr 30;458(7242):1158–62.
3. Smil V. Energy Transitions: History, Requirements, Prospects. Praeger. 2010.
4. Renewable Electricity Future. In: National Renewable Energy Laboratory. 2012.
5. A. Greening L, Greene DL, Difiglio C. Energy efficiency and consumption — the rebound effect — a survey. *Energy Policy*. Elsevier Science Ltd; 2000 Jun;28(6–7):389–401.
6. McKendry P. Energy production from biomass (part 3): gasification technologies. *Bioresour Technol*. 2002 May;83(1):55–63.
7. Choi J. Development of Visible-Light-Active Photocatalyst for Hydrogen Production and Environmental Application. 2010;2010:229.
8. Liu G, Hoivik N, Wang K, Jakobsen H. Engineering TiO₂ nanomaterials for CO₂ conversion/solar fuels. *Sol Energy Mater Sol Cells*. 2012 Oct;105:53–68.
9. Roy SC, Varghese OK, Paulose M, Grimes CA. Toward Solar Fuels : Photocatalytic Hydrocarbons. 2010;4(3):1259–78.
10. HARVEY L. Solar-hydrogen electricity generation and global CO₂ emission reduction. *Int J Hydrogen Energy*. 1996 Jul;21(7):583–95.
11. Zini G, Tartarini P. Solar Hydrogen Energy Systems. *Solar Hydrogen Energy Systems: Science and Technology for the Hydrogen Economy*. Milano: Springer Milan; 2012. 1-184 p.
12. Barreca D, Carraro G, Gombac V, Gasparotto A, MacCato C, Fornasiero P, et al. Supported metal oxide nanosystems for hydrogen photogeneration: Quo vadis? *Adv Funct Mater*. 2011;21(14):2611–23.
13. Inoue T, Fujishima A, Konishi S, Honda K. Photoelectrocatalytic reduction of carbon dioxide in aqueous suspensions of semiconductor powders. *Nature*.

14. Yamada Y, Kanemitsu Y. Determination of electron and hole lifetimes of rutile and anatase TiO_2 single crystals. *Appl Phys Lett.* 2012;101(13):133907.
15. Miseki Y, Kato H, Kudo A. Water splitting into H_2 and O_2 over niobate and titanate photocatalysts with (111) plane-type layered perovskite structure. *Energy Environ Sci.* 2009;2(3):306.
16. Kudo A. Development of photocatalyst materials for water splitting. *Int J Hydrogen Energy.* 2006;31(2):197–202.
17. Maijenburg AW, Veerbeek J, de Putter R, Veldhuis SA, Zontjes MGC, Mul G, et al. Electrochemical synthesis of coaxial TiO_2 –Ag nanowires and their application in photocatalytic water splitting. *J Mater Chem A.* 2013 Dec 5;2(8):2648–56.
18. Liu G, Hoivik N, Wang K, Jakobsen H. Engineering TiO_2 nanomaterials for CO_2 conversion/solar fuels. *Sol Energy Mater Sol Cells.* Elsevier; 2012 Oct;105:53–68.
19. Qin H, Lin W, Zhang ZC, Cheng JY, Kong Y. Synthesis of F- TiO_2 ; Nanosheets and its Photocatalytic Oxidation of Benzene to Phenol. *Adv Mater Res.* 2013;750–752:1160–3.
20. Sun L, Zhai J, Li H, Zhao Y, Yang H, Yu H. Study of Homologous Elements: Fe, Co, and Ni Dopant Effects on the Photoreactivity of TiO_2 Nanosheets. *ChemCatChem.* 2014 Jan 24;6(1):339–47.
21. Yoong LS, Chong FK, Dutta BK. Development of copper-doped TiO_2 photocatalyst for hydrogen production under visible light. *Energy.* Elsevier Ltd; 2009;34(10):1652–61.
22. Wang T, Gong J. Single-Crystal Semiconductors with Narrow Band Gaps for Solar Water Splitting. *Angew Chem Int Ed Engl.* Wiley-VCH Verlag; 2015 Sep 7;54(37):10718–32.
23. Umebayashi T, Yamaki T, Itoh H, Asai K. Analysis of electronic structures of 3d transition metal-doped TiO_2 based on band calculations. *J Phys Chem Solids.* 2002;63:1909–20.
24. Choi J, Park H, Hoffmann MR. Effects of Single Metal-Ion Doping on the Visible-Light Photoreactivity of TiO_2 . *J Phys Chem C.* 2010 Jan 21;114(2):783–92.

25. Hoffmann MR, Martin ST, Choi W, Bahnemann DW. Environmental applications of semiconductor photocatalysis. *Chem Rev.* 1995;95(1):69–96.
26. Klosek S, Raftery D. Visible light driven V-doped TiO₂ photocatalyst and its photooxidation of ethanol. *J Phys Chem B.* 2002;105(14):2815–9.
27. Anpo M, Higashimoto S. The local structures of transition metal oxides incorporated in zeolites and their unique photocatalytic properties. In: *Studies in Surface Science and Catalysis.* 2001. p. 123–32.
28. Di Paola A, García-López E, Ikeda S, Marcì G, Ohtani B, Palmisano L. Photocatalytic degradation of organic compounds in aqueous systems by transition metal doped polycrystalline TiO₂. *Catal Today.* 2002 Jul;75(1–4):87–93.
29. Čaplovičová M, Billik P, Čaplovič L', Brezová V, Turáni T, Plesch G, et al. On the true morphology of highly photoactive anatase TiO₂ nanocrystals. *Appl Catal B Environ.* 2012 May;117–118:224–35.
30. Mao J, Ye L, Li K, Zhang X, Liu J, Peng T, et al. Pt-loading reverses the photocatalytic activity order of anatase TiO₂ {001} and {010} facets for photoreduction of CO₂ to CH₄. *Appl Catal B Environ.* Elsevier B.V.; 2014;144:855–62.
31. Zou JJ, He H, Cui L, Du HY. Highly efficient Pt / TiO₂ photocatalyst for hydrogen generation prepared by a cold plasma method. *Int J Hydrogen Energy.* 2007;32(12):1762–70.
32. Lin C-H, Lee C-H, Chao J-H, Kuo C-Y, Cheng Y-C, Huang W-N, et al. Photocatalytic Generation of H₂ Gas from Neat Ethanol over Pt/TiO₂ Nanotube Catalysts. *Catal Letters.* 2004 Oct;98(1):61–6.
33. Ran J, Zhang J, Yu J, Jaroniec M, Qiao SZ. Earth-abundant cocatalysts for semiconductor-based photocatalytic water splitting. *Chem Soc Rev.* Royal Society of Chemistry; 2014;43:7787–812.
34. Benedix R, Dehn F, Quaas J, Orgass M. Application of titanium dioxide photocatalysis to create self-cleaning building materials. *Lacer.* 2000;3:157–68.
35. Janczarek M, Hupka J, Kisch H. HYDROPHILICITY OF TiO₂ EXPOSED TO UV AND VIS RADIATION. *Glass.* 2006;40:287–92.

36. Barthlott W, Neinhuis C. Purity of the sacred lotus, or escape from contamination in biological surfaces. *Planta*. 1997;202:1–8.
37. Asahi R, Morikawa T, Ohwaki T, Aoki K, Taga Y. Visible-light photocatalysis in nitrogen-doped titanium oxides. *Science*. 2001;293(5528):269–71.
38. Liu G, Yu JC, Lu GQM, Cheng H-M. Crystal facet engineering of semiconductor photocatalysts: motivations, advances and unique properties. *Chem Commun (Camb)*. 2011 Jun 28;47(24):6763–83.
39. Liu S, Yu J, Jaroniec M. Anatase TiO₂ with Dominant High-Energy {001} Facets : Synthesis , Properties , and Applications. 2011;4085–93.
40. Liu G, Yang HG, Wang X, Cheng L, Pan J, Lu GQ (Max), et al. Visible Light Responsive Nitrogen Doped Anatase TiO₂ Sheets with Dominant {001} Facets Derived from TiN. *J Am Chem Soc*. 2009 Sep 16;131(36):12868–9.
41. Khan MA, Jung H-T, Yang O-B. Synthesis and characterization of ultrahigh crystalline TiO₂ nanotubes. *J Phys Chem B*. 2006 Apr 6;110(13):6626–30.
42. Yang HG, Sun CH, Qiao SZ, Zou J, Liu G, Smith SC, et al. Anatase TiO₂ single crystals with a large percentage of reactive facets. *Nature*. 2008 May 29;453(7195):638–41.
43. Zhu S, Liang S, Gu Q, Xie L, Wang J, Ding Z, et al. Effect of Au supported TiO₂ with dominant exposed {001} facets on the visible-light photocatalytic activity. *Appl Catal B Environ*. Elsevier B.V.; 2012;119–120:146–55.
44. Wu L, Yang BX, Yang XH, Chen ZG, Li Z, Zhao HJ, et al. On the synergistic effect of hydrohalic acids in the shape-controlled synthesis of anatase TiO₂ single crystals. *CrystEngComm*. 2013;15(17):3252–5.
45. Ong W-J, Tan L-L, Chai S-P, Yong S-T, Mohamed AR. Highly reactive {001} facets of TiO₂-based composites: synthesis, formation mechanism and characterization. *Nanoscale*. 2014 Mar 21;6(4):1946–2008.
46. Sun X, Li Y. Synthesis and characterization of ion-exchangeable titanate nanotubes. *Chemistry*. 2003 May 23;9(10):2229–38.
47. Carneiro JT, Savenije TJ, Moulijn J a., Mul G. How phase composition influences optoelectronic and photocatalytic properties of TiO₂. *J Phys Chem C*. 2011;115(5):2211–7.

48. Kuo H-L, Kuo C-Y, Liu C-H, Chao J-H, Lin C-H. A highly active bi-crystalline photocatalyst consisting of TiO₂ (B) nanotube and anatase particle for producing H₂ gas from neat ethanol. *Catal Letters.* 2007 Jan 13;113(1–2):7–12.
49. Kandiel TA, Feldhoff A, Robben L, Dillert R, Bahnemann DW. Tailored Titanium Dioxide Nanomaterials: Anatase Nanoparticles and Brookite Nanorods as Highly Active Photocatalysts. *Chem Mater.* 2010 Mar 23;22(6):2050–60.
50. Tay Q, Liu X, Tang Y, Jiang Z, Sum TC, Chen Z. Enhanced Photocatalytic Hydrogen Production with Synergistic Two-Phase Anatase/Brookite TiO₂ Nanostructures. *J Phys Chem C.* 2013 Jul 25;117(29):14973–82.
51. Navarro RM, Peña MA, Fierro JLG. Hydrogen production reactions from carbon feedstocks: fossil fuels and biomass. *Chem Rev.* 2007 Oct;107(10):3952–91.
52. Cagnello M, Gasparotto A, Gombac V, Montini T, Barreca D, Fornasiero P. Photocatalytic H₂ and added-value by-products—the role of metal oxide systems in their synthesis from oxygenates. *Eur J Inorg Chem.* 2011;(28):4309–23.
53. Zinoviev S, Müller-Langer F, Das P, Bertero N, Fornasiero P, Kaltschmitt M, et al. Next-generation biofuels: Survey of emerging technologies and sustainability issues. *ChemSusChem.* 2010 Oct 25;3(10):1106–33.



Methodology

2. Methodology

The basic principles of the main experimental characterization techniques used in the present work are briefly described in this chapter. As it would be shown in the following chapters, the use of electron microscopy was crucial to determinate the morphology and chemical composition of the samples at the sub-nanometric scale. Therefore, an in-depth description of the electron microscopy and related techniques is included in section 2.7. The last two sections of the chapter include the description of the photocatalytic reactors and the experimental procedure used to evaluate the self-cleaning capacity and the activity in the ethanol photo-reforming of the materials. In order to facilitate the reading, a detailed description of the solvo-thermal synthesis of nanosheets, and TiO₂ nanorods, and TiO₂-SiO₂ nanocoatings, are included at the beginning of each corresponding chapter.

2.1 Textural analysis. Nitrogen physisorption technique

The surfaces area (S_{BET}) of the samples were analysed by nitrogen physisorption at the liquid nitrogen temperature (~ 77K).

Physisorption is a general phenomenon: it occurs whenever an absorbable gas (the adsorptive) is brought into contact with the surface of a solid (the adsorbent).

From the nitrogen adsorption isotherms on porous solids, it is possible to determine the specific surface area, the total pore volume and their distribution using different mathematical models. The specific surface determined by BET model relates to the total surface area (reactive surface) as all porous structures adsorb the small gas molecule. The volume of gas adsorbed to the surface of the particles is measured at the liquid nitrogen temperature ~ 77 K). The amount of adsorbed gas is correlated to the total surface area of the particles including pores in the surface. Traditionally nitrogen is used as adsorbate gas, the relative pressure range is $10^{-7} \leq p/p_0 \leq 1$. The Brunauer-Emmett-Teller (BET)⁽¹⁾ model assumes the following hypotheses:

- The gas molecules are adsorbed in successive layers.
- There is no interaction between each adsorption layer.
- The Langmuir theory can be applied to each layer.

The mathematical equation that describes this model is the following:

$$\frac{P}{V \cdot (P - P_0)} = \frac{1}{V_m \cdot C} + \frac{(C - 1) \cdot P}{V_m \cdot C \cdot P_0} \quad Eq. 2.1$$

where, V is the amount of gas adsorbed at a pressure P, P_0 is the saturation pressure, V_m is the volume of the monolayer of adsorbate and C is a constant related to the adsorption equilibrium and with the energy of the adsorption (stronger the interaction between adsorbate and adsorbent, higher the C value – Fig. 2.1). B.E.T. equation is typically applied in the relative pressure range $0.1 \leq p/p_0 \leq 0.35$ to determine the surface are of the investigated material.

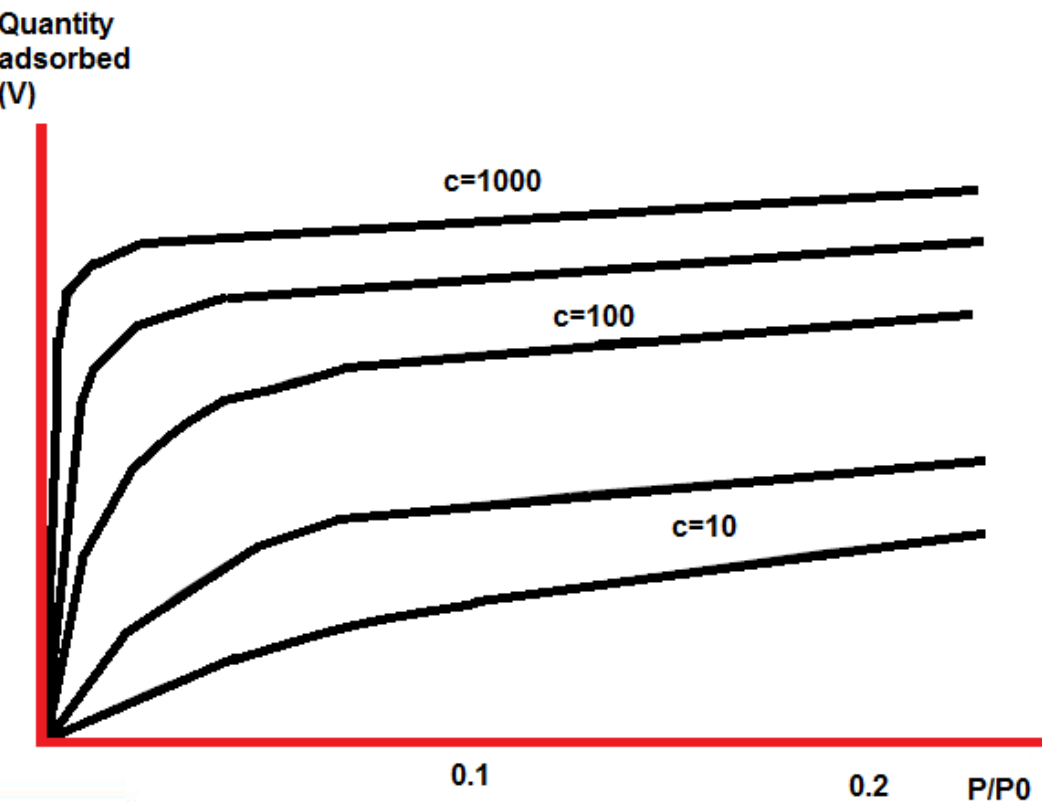


Fig.2.1 Adsorption isotherm as a function of the c-value.

Commonly, most of the catalytic materials have a high surface area and a porous structure that would determinate the reactants accessibility. It is therefore obvious the importance of a comprehensive characterization of the texture of catalytic materials. Accordingly to the IUPAC classification ⁽²⁾, pores can be classified depending on their dimension, as follow:

- micropores, with diameters less than 2 nm.
- mesopores, with diameters in the range 2 - 50 nm.
- macropores, with diameters larger than 50 nm.

The porous structure of a material can be qualitatively evaluated by the shape of the physisorption isotherm. The International Union for Pure and Applied Chemistry (IUPAC) has classified the most common isotherms into six types (Figure 2.2, left) ⁽²⁾:

Type I isotherm is typical of microporous systems, in which the external surface area is small while the internal contribute is relevant.

Type II isotherm is generally observed in non-porous or macroporous systems and represents a multi-layer adsorption. The B point (at the inflection point) is generally considered as the point of monolayer formation.

Type III and V isotherms are not common and indicate a very weak interaction between adsorbent and adsorbate. This problem can be solved using a different adsorbate in order to obtain a physisorption curve easier to analyse.

Type IV isotherm is the most common one and it is typical of mesoporous systems. The initial part of the isotherm is similar to that of type II one while, at higher relative pressures, it shows the typical hysteresis associated to capillary condensation that takes place into the mesoporous. The hysteresis shape can change to a great extent according to pores geometry. IUPAC has classified the hysteresis shapes into four main groups, denoted as H1, H2, H3 and H4 (Figure 2.2 right). Type H1 and H4 hysteresis represent two opposite and extreme situations: the first is often found in compact agglomerates of spherical particles with uniform dimensions. The latter one is obtained in the case of materials with pores formed by the aggregation of bidimensional particles. Type H2 and H3 hysteresis represents intermediate situations between those two extremes. However, hysteresis cannot be easily classified as most of the materials show heterogeneous distributions in shapes and dimensions of pores.

Type VI isotherm represents a multilayer adsorption which occurs by subsequent passages onto a non-porous surface.

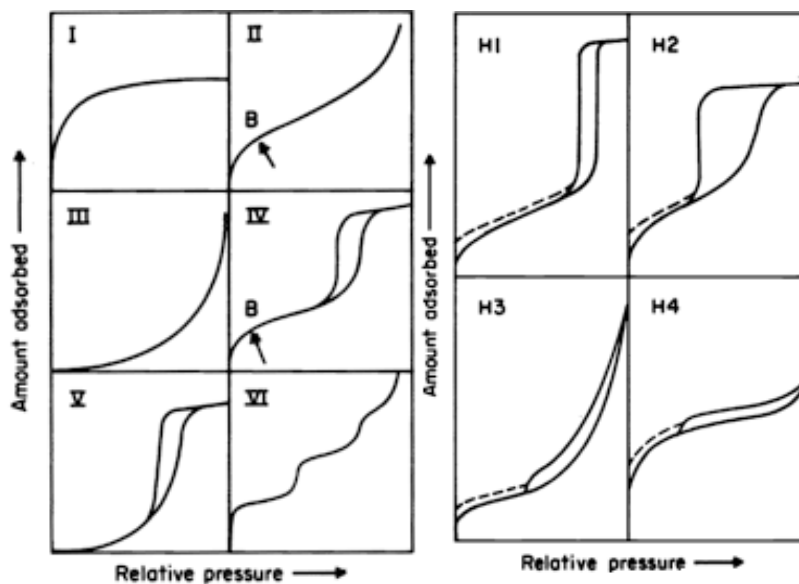


Fig. 2.2 Classification of isotherms (left) and hysteresis (right)

The calculation of the pore volume and size distribution can be determined by the method developed by Barrett, Joiner and Halenda (BJH model). This model describes the adsorption and capillary condensation process inside the mesopores, that is controlled by the Kelvin equation:

$$\ln \frac{p}{p^0} = \frac{\gamma 2V_m \cos \theta}{RT r_c} \quad Eq. 2.2$$

where: p pressure of the gas; p^0 gas saturation pressure; g surface tension of the liquid; V_m liquid molar volume; R gas constant; T absolute temperature; r_c pore radius where capillary condensation occurs. The pressure range (0.4-0.967) is generally used as initial data for BJH calculations.

In the present thesis, physisorption characterization were performed using two different equipment and experimental conditions. For the textural analysis of TiO₂ anatase/brookite and TiO₂ nanosheets (Chapters 3 and 4), a Micromeritics ASAP 2020 system was used. In this case, the samples have been degas at 120°C for twelve hours. Nitrogen adsorption-desorption isotherms were obtained by taking 40 points for adsorption curve and 25 for desorption curve. For the characterization of TiO₂ nanocoatings samples, an Autosorb IQ system from Quantachrome was used. Theses samples were evacuated for 15 hours at 150°C. 90 points were recorded for the adsorption

curve, while 40 points were obtained for the desorption curve. Both equipments are located at the IMEYMAT (Instituto Universitario de Investigación en Microscopía Electrónica y Materiales) at the University of Cadiz.

2.2 Diffuse reflectance spectroscopy in the ultraviolet-visible range (UV-Vis)

When radiation interacts with matter, a number of processes can occur, including reflection, scattering, absorbance, fluorescence/phosphorescence (absorption and reemission), and photochemical reactions. In general, when measuring UV-visible spectra, absorbance is the only desired process. This phenomenon happens when the photons have enough energy to cause transitions between the different electronic energy levels. In this case, a fraction of the light with that wavelength is absorbed and electrons are transferred from a lower energy level to a higher energy level.

In the case of semiconductors, the UV-vis absorption is related to transitions from the valence band (VB) to the conduction band (CB) and to many other electronic transitions involving intra-gap states related to the presence of dopants and/or defects of the structure. Fig 2.3 represents the possible electron transitions in the UV-visible range for a semiconductor. The effect of dopants can create additional donor or trap levels, leading to additional absorption bands. In addition, it is reported in the literature that the size and shape of the semiconductor nanoparticles can modify the optical properties ^(3,4). The quantum confinement effect is observed when the size of the particle is too small to be comparable to the wavelength of the electron. Confinement indicates the confinement of the motion of randomly moving electron to restrict its motion in specific energy levels (discreteness) and quantum reflects the atomic realm of particles. The decrease in size of a particle up to the nano-scale level makes the energy levels discrete and increases or widens up the band gap. Ultimately, the band gap energy increases.

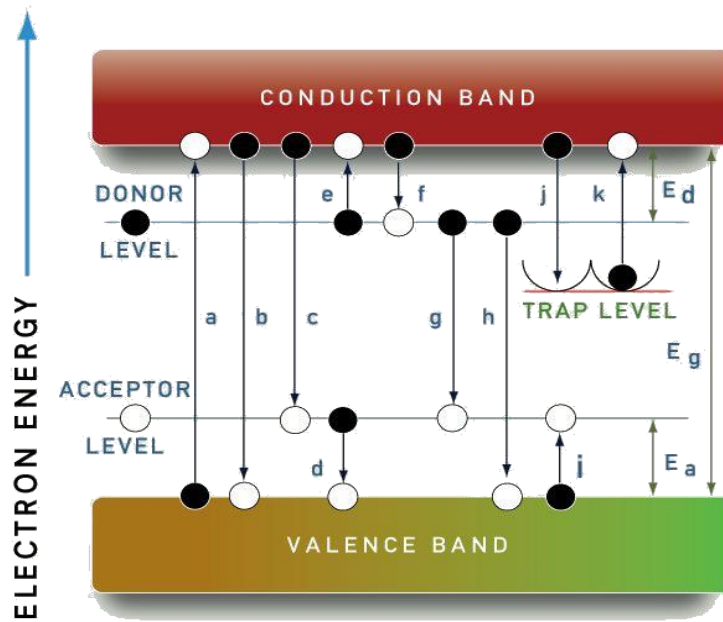


Fig. 2.3 Electronic transitions observed in a classical semiconductor with dopants (donor (a,e,i) and acceptor(b,c,d,f,g,h) levels) and defects (trap levels (j,k)).

One of the objective of the present work is to obtain doped TiO₂ nanosheets to improve the Sunlight harvesting to promote photocatalytic reactions. In this context, the characterization by UV-Vis spectroscopy is crucial to discuss the effect of the dopants in the electronic structure of TiO₂ and its absorptive properties.

The Tauc's plot is a method that is widely used for the determination of the band gap ⁽⁵⁾. This model is based on the assumption that the energy-dependent absorption coefficient (α) can be expressed as:

$$\alpha h\nu = A(h\nu - E_g)^n \quad Eq. 2.3$$

where, α is the absorption coefficient, A is a constant, $h\nu$ is photon energy, E_g is the allowed energy gap, $n = \frac{1}{2}$ for allowed direct transition and $n = 2$ for allowed indirect transition.

Figure 2.4 shows a typical representation of Tauc's plot for an allowed indirect transition. The band gap can be obtained by the fitting of the lineal part of the curve to obtain the $h\nu$ value corresponding to $(\alpha h\nu)^n$.

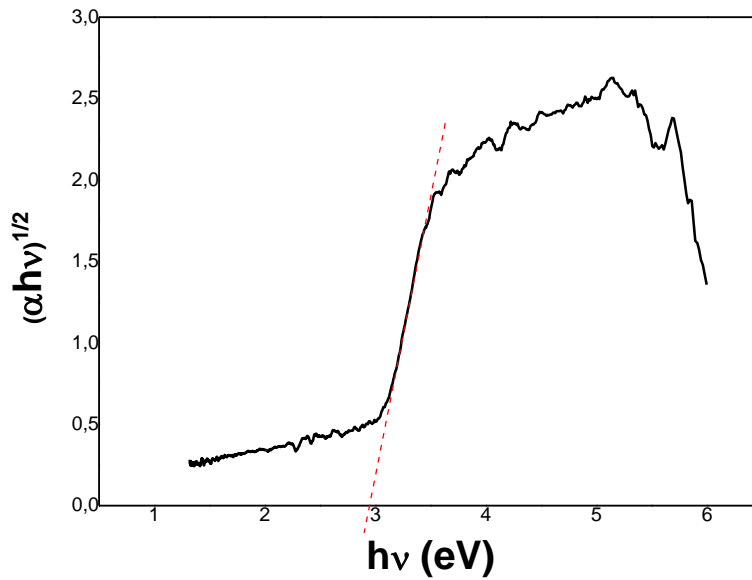


Fig. 2.4 Representation of the Tauc law for the data of TiO_2 nanosheet undoped. The cut the horizontal axis provides the energy gap that is 2.98 eV.

When solid samples are analysed, it is difficult to obtain a transmittance spectrum and therefore the reflectance technique is typically used. The raw diffuse reflectance spectra appears different from its transmission equivalent (stronger than the expected absorption). However, the Kubelka-Munk conversion can be applied to a diffuse reflectance spectrum to compensate these differences. The Kubelka-Munk equation is expressed as follows:

$$F_{KM}(R) = \frac{(1 - R)^{1/n}}{2R} \quad Eq. 2.4$$

where R is the absolute reflectance of the sample layer.

In the present thesis, the diffuse reflectance spectra in the UV-Visible region were recorded on a homemade system located at the Instituto de Ciencia de Materiales de Sevilla (ICMS). A sketch of the equipment is included in Fig. 2.5 and it is based on the following elements:

- An UV spectrometer model AvaSpec-ULS2048 that includes deep-UV detector coating for better performance in the deep-UV-range, a detector collection lens to enhance sensitivity in the 200-1100 nm range and

order-sorting filters to reduce 2nd order effects. The resolution of the equipment was 0.6 nm.

- A Deuterium-Halogen light source model AvaLight-DH-S. The spectral range of the equipment is from 200 to 2500 nm. An integrated TTL-shutter is included and it was controlled from the AvaSpec software.
- A reflection probe based on a fibre bundle was used to irradiate the sample and collect the spectra emitted by the sample.

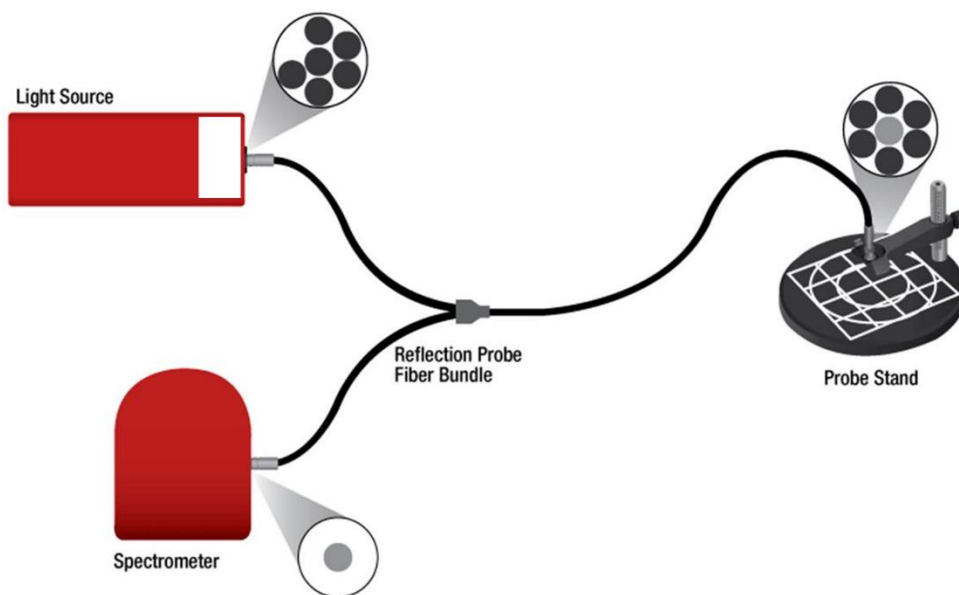


Fig. 2.5 Sketch of the experimental setup used to obtain the band gap of TiO₂ samples.

The system was previously calibrated with BaSO₄ as a reference signal. The TiO₂ powers were compacted on a small sample holder. The sample holder is placed in a box in order to carry out the measurement without light pollution from outside.

2.3 Raman Spectroscopy

Raman spectroscopy is a vibrational spectroscopy technique based on inelastic scattering of monochromatic light, usually from a laser source. Inelastic scattering means that photons in the monochromatic light change their frequency due to the interaction with a sample. This energy variation is related with a change in vibrational and rotational modes or electronic configuration of the sample. Raman spectroscopy can be used to study solid, liquid and

gaseous samples. This technique is highly selective, allowing to identify and differentiate molecules and chemical species. In the present work, Raman spectroscopy has been used to study the presence of different TiO_2 polymorphs in the samples. Figure 2.6 presents the Raman spectra of the main TiO_2 polymorphs, highlighting the differences among them.

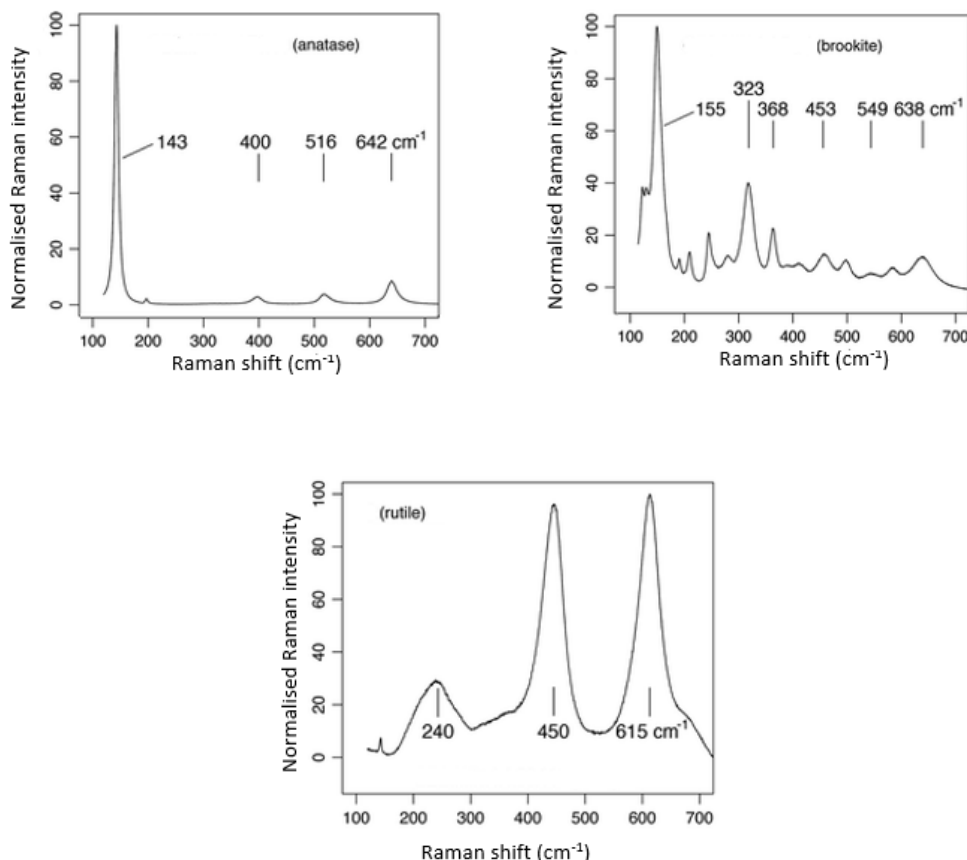


Fig. 2.6 Raman spectra of anatase, brookite, and rutile. Rutile was identified by Raman bands at 240, 450, and 615 cm^{-1} (peak positions) and anatase by bands at 143, 400, 516, and 642 cm^{-1} . Brookite produces a range of Raman bands with varying intensities, among these are bands at 128, 155, 215, 247, 250, 289, 323, 368, 453, 549, and 638 cm^{-1}

The Raman spectra of the TiO_2 samples prepared in this study were recorded using a spectrometer inVia Renishaw Raman Microscope with a laser source of 532 nm. This microRaman tool, by coupling the instrument to a Raman microscope, allows focusing the laser beam in one bright spot of small

size. It is therefore possible to collect Raman spectra in different areas of the sample. Data were collected with a power of 1 mW at a magnification of 100x and in the energy range from 100 cm^{-1} to 1500 cm^{-1} . The instrument is located at the Department of Chemical and Pharmaceutical Sciences, at the University of Trieste (Italy).

2.4 X-Ray Photoelectron Spectroscopy (XPS)

The X-ray photoelectron spectroscopy is widely used for the superficial characterization of solids. XPS spectra are obtained by irradiating a material with a high energy beam of X-ray that commonly comes from an Mg and/or Al anode. As a result of the interactions between the beam and the sample, we can observe the photoionization or photoemission of electrons from the sample. XPS is obtained by recording the amount of photo-emitted electrons as a function of their kinetic energy.

The kinetic energy of the photo-emitted electrons (E_k) can be related with the electron binding energy (E_B) and with the energy of the X-ray photons ($h\nu$):

$$E_B = (h\nu) - (E_k + \varphi_{\text{spec}}) \quad \text{Eq. 2.5}$$

where φ_{spec} is the work function of electron absorption in the detector of the spectrometer. It is a constant that rarely needs to be adjusted in practice.

The energy of the photoelectrons leaving the sample gives a spectrum with a series of photoelectron peaks (Fig. 2.7). The binding energy of the peaks is characteristic of each element and its oxidation state. In addition, the shape of the peak, as well as the binding energy, can be slightly altered by the chemical environment of the emitting atom.

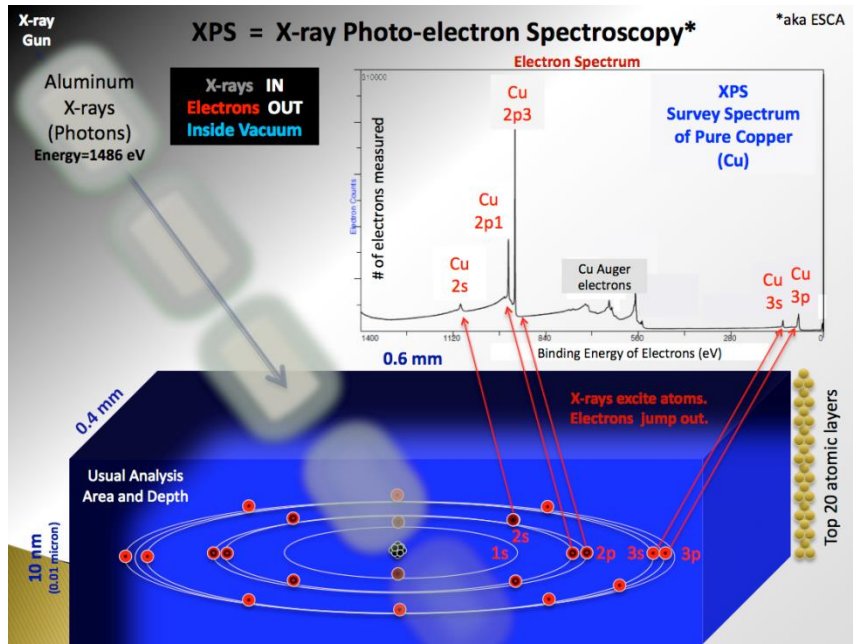


Fig. 2.7 Schematic representation of a X-Ray Photo-electron Spectroscopy system⁽⁶⁾

Experiments were carried out in an ultrahigh vacuum system with a base pressure of 1×10^{-8} Pa. The system is equipped with a dual anode laboratory X-ray source (SPECS XR50) and an electron energy analyser (SPECS Phoibos 150). XPS spectra were recorded using an excitation energy of $h\nu = 1486.6$ eV (Al K_α) with electrons emitted along the samples surface normal (the angle of incidence of the X-rays with respect to the sample normal was 68°). The instrument is located at the Department of Surface and Plasma Science of the Charles University in Prague (Czech Republic).

2.5 Inductively coupled plasma atomic emission spectroscopy atomic emission Spectroscopy (ICP-AES)

This technique was used to determine the effective content of the transition metal present in the doped-TiO₂ samples. Inductively coupled plasma atomic emission spectroscopy (ICP-AES) is a chemical analysis method which use the intensity of light emitted from a flame, plasma, arc or spark in a particular wavelength to determine the amount of an element in a sample. The wavelength of the atomic spectral line gives the identity of the element, while the intensity of the emitted light is proportional to the number of atoms of the specific element.

Samples (0.1g) were dissolved in HF by microwave-assisted acid digestion (microwave Berghof Speedwave four) and were measured twice in order to obtain reliable results. After complete dissolution, ICP-AES analysis was performed using an Iris Thermo Elemental Intrepid instrument, located at the Servicios Centrales de Ciencia y Tecnología at the University of Cadiz.

2.6 Powder X-Ray diffraction (XRD)

X-ray diffraction is one of the most commonly used techniques to determinate the structure of crystalline samples. This technique is based on the diffraction of an x-ray beam by the family of planes of a crystalline structure. A reflection is observed when a constructive interference of all the diffracted rays occurs. Under these conditions, the Bragg's law ⁽⁷⁾ is satisfied:

$$\lambda = 2d_{hkl} \sin \theta \quad \text{Eq. 2.6}$$

where d_{hkl} is the spacing among the planes of the hkl family of planes, λ and θ are the wavelength and the incident angle of the incoming X-Ray beam, respectively.

An exhaustive characterization of all the samples have been carried out by powder XRD to identify the phase composition of the samples and estimate the average crystallite size. The relative amount of different TiO₂ polymorphs

has been calculated by Rietveld refinement of the XRD patterns using the PowderCell 2.3 software for data analysis. The average crystallite size of the samples can be calculated using the Scherrer's equation:

$$d_p = \frac{k\lambda}{(B\cos\theta)} \quad Eq. 2.7$$

where d_p is the average crystallite size, λ is the wavelength of the incident X-ray radiation, θ is the diffraction angle, k is the Scherrer constant, that take an average value of 0.9 and B is the full width at half the maximum (FWHM) in radians of the X-ray diffraction peak Qualitatively, small and broad diffraction peaks are typically the evidence of low crystalline samples or the presence of small crystals. This approach allows to calculate the average crystallite dimension in the direction perpendicular to the considered reflection plane. Therefore, the morphology of the sample will affect the peak broadening in the overall XRD pattern. In this context, an anisotropic morphology of the crystals will reflect in anisotropic peak broadening.

In the present work X-ray diffraction (XRD) patterns were collected by a Philips X'Pert diffractometer using a Cu K α ($\lambda= 0.1544$ nm) X-ray source in the range $10^\circ < 2\theta < 100^\circ$. The instrument is located at the Department of Chemical Sciences and Technologies at the University of Udine (Italy).

2.7 Transmission Electron Microscopy

Transmission Electron Microscopy (TEM) has been proven as an extremely powerful characterization tool and it is nowadays indispensable in nanotechnology. In heterogeneous catalysis, TEM makes possible the in depth study of some key parameters of the active phases, such as the size of the metal particles and the morphology of the catalysts.

In this thesis, TEM was used to determine the morphology and crystal size of TiO₂ nanoparticles, as well as to obtain the particle size distribution of the Pt nanoparticles on the surface of the catalytic materials. These informations were crucial to fully understand the influence of the TiO₂

morphology, the sample structural anisotropy and co-catalyst (Pt) size on the photocatalytic activity. The nanostructural and morphological characterization of the samples were obtained by the combination of High Resolution Electron Microscopy (HREM) and High Angle Annular Dark Field (HAADF) images. On the other hand, the intensively use of spectroscopic techniques, such as Energy-Dispersive X-ray Spectroscopy (EDS) and Electron Energy Loss Spectroscopy (EELS), allowed to get information about the chemical composition of the sample at subnanometric scale.

Transmission Electron Microscopy was developed to overcome the resolution limitations of light microscopes. Accordingly, to the Wave-Particle Duality theory developed by De Broglie, accelerated electrons have an associated wavelength much smaller than the light. This wavelength can be calculated using the following equation:

$$\lambda = \frac{h}{(2m_o eV)^{1/2}} \quad Eq. 2.8$$

where m_o is the electron mass, e its charge, V is the accelerating voltage and h the Planck constant.

This equation, even though doesn't include relativistic effects, can give us an idea of the theoretical resolution limits of TEM. As example, an electron accelerated at 200 KV have an associated wavelength of 0.00025 nm, that is two orders of magnitude smaller than the diameter of an atom. This fact immediately highlights the potential of using electrons as an alternative to visible light for illuminating the sample. Electron microscopes use an electron beam to illuminate the sample and a number of electromagnetic lenses, within a high vacuum, to obtain high magnification images.

It must be pointed out that electromagnetic lenses have important practical limitations that negatively affect the resolution limit. The poor homogeneity of the magnetic fields within electromagnetic lenses introduce strong spherical and chromatic aberrations, limiting the resolution of conventional instruments. Both defects are unavoidable in the case of static rotationally symmetric electromagnetic fields (Scherzer's theorem). However,

the use of multipole correctors or electron mirrors can partially reduce these limitations. In fact, the recent addition of spherical aberration correctors to transmission electron microscopes opened the possibility to improve the spatial resolution (Figure 2.8). As an example, an electron microscope equipped a standard field emission gun has a resolution limit of 0.19 nm in HREM mode, while that an aberration corrected electron microscope can reach 80 pm. Considering this, there was, in the last decades, a great interest in combining spectroscopic and imaging techniques with atomic resolution. The improvement of the spatial resolution, combined with the capability of performing chemical analysis by spectroscopy techniques (EELS and EDS), is crucial to extend the structural and chemical knowledge on the materials to optimize its properties.

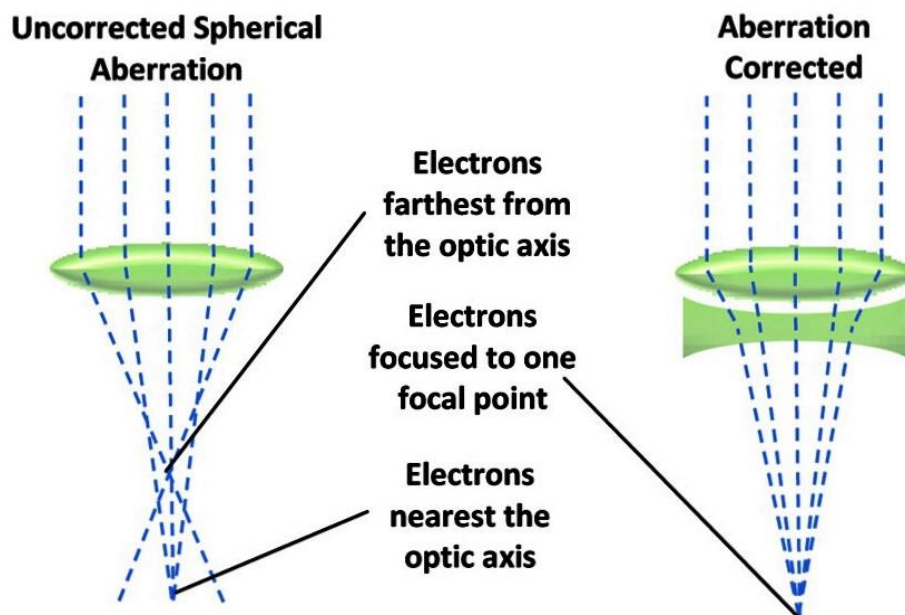


Fig. 2.8 Spherical aberration for an uncorrected lens and aberration correction using a compensating lens system ⁽⁸⁾.

A transmission electron microscope consists of a vertical column, hold in ultra-high vacuum, in which the lenses are placed to modify the trajectories of the electrons. The main parts of the TEM are the following:

- a) An electron source with the function of generating the electron beam. The most common methods to generate the electron beam are the thermionic effect and the field emission. The first one is based on heating a material (tungsten or LaB₆) enough to extract electrons. The field emission gun extracts electrons from a small tip ZrO₂ (100nm) using an electrical field of a few KV. The electron beam obtained by field emission sources is brighter and more monochromatic than those generated by thermionic processes, allowing to improve both spatial and the energy loss spectra resolution.
- b) An anode to accelerate the emitted electrons.
- c) The condenser lenses that prepare the beam before arriving on the sample. These lenses can create a parallel (image mode) or a converged beam (scanning mode).
- d) Condenser aperture to select the part of the beam that will reach the sample.
- e) Objective aperture (image mode) to select the diffracted beams that will be used for the image generation.
- f) The objective lenses that create the image by the coherence interference of the transmitted and diffracted beams (image mode).
- g) Finally, a detector, which depend on the operating mode, to record the image. The most common detectors will be described later.

As it was mentioned before, the condenser lenses can create a parallel beam or a converged beam. The first one is needed to work in image mode and obtain high resolution images, while the second is used to work in Scanning mode. The main operational differences are summarized in Figure 2.9 and their main characteristics are discussed below.

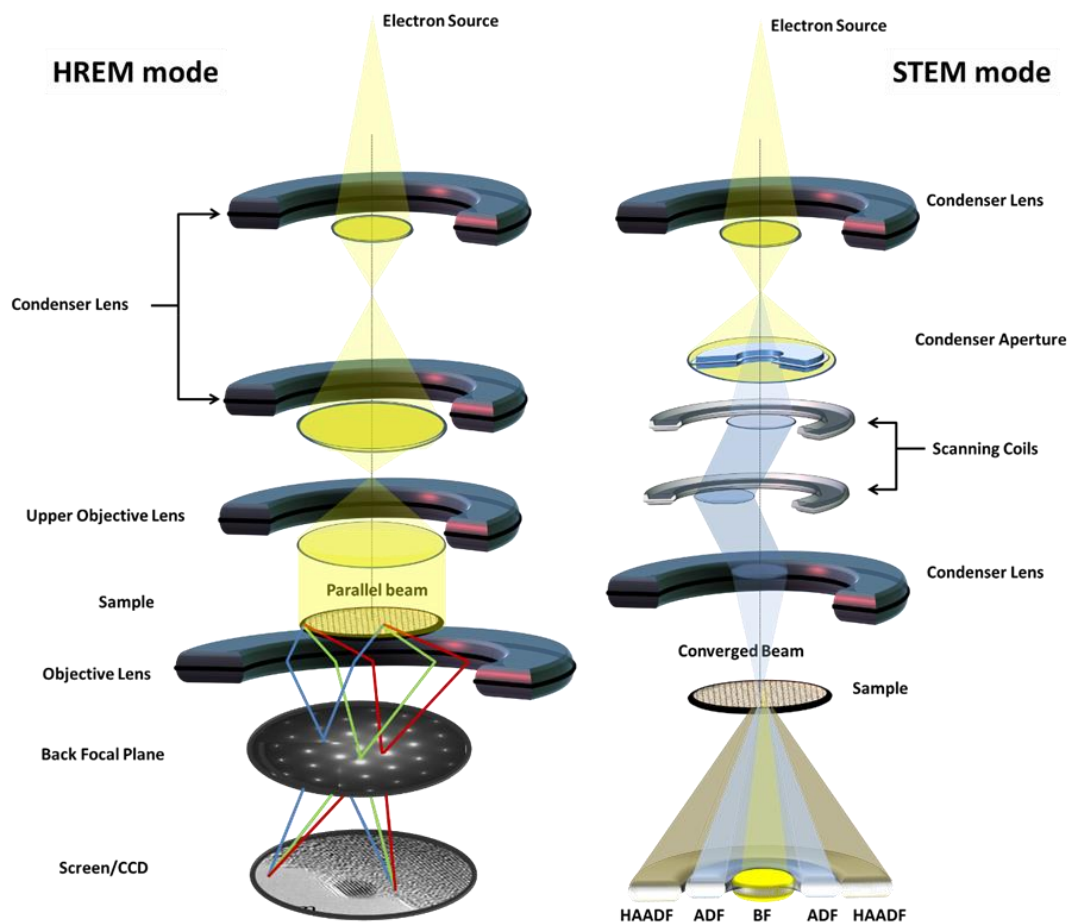


Fig. 2.9 Schematic representation of the parallel beam (HREM) and convergent beam (STEM)

High Resolution Electron Microscopy (HREM)

HRTEM allows to obtain details about of the crystal structure of the sample at the atomic scale, which can be extracted from the interpretation of so-called high-resolution images. This technique is based mainly on diffraction phenomena which occur when a parallel beam of electrons crosses the different crystals forming the sample. Figure 2.9 presents the main lenses configuration required to obtain HREM images. The condenser lenses allow to create a parallel that will interact with the sample, generating the electron diffraction pattern (EDP) in the Back Focal Plane.

EDP is a powerful tool for structural characterization and it can be easily interpreted using the diffraction theory, such as the Bragg's law (Eq. 2.6):

scattered beams at higher angles will be observed for the atomic planes with smaller spacing. In fact, the EDP is equivalent to the reciprocal space and the characteristic spacing of the planes and angles that form between them can be easily obtained. These information, in combination with the crystal structures, make possible to determinate the orientation of crystal, called zone axis [uvw], as index the planes (hkl) observed in the EDP.

Considering that each point in the EDP behaves as a source of electron waves and keeping in mind that these waves are coherent to each other, the waves emitted from these points will interfere among them giving rise, at a certain distance from the Back Focal Plane (BFP), to an interference pattern, Figure 2.10. This interference pattern is called the HREM image and it is recorded using a digital camera. This image will show the families of planes those compose the material under investigation as long as the resolution of the equipment allows it and the Bragg conditions are satisfied. Therefore, valuable structural information of the sample can be obtained by studying HREM images. This analysis can be performed by obtaining digital diffraction patterns (DDP), which mainly correspond to a logarithmic representation of the squared modulus of the fast Fourier transform (FFT) applied to one selected area of the image. The DDP can be obtained with the help of a software. In the present work, as mentioned in subsequent paragraph is used EJE Z software to obtained the DDP from the HREM images. In this way, we can easily bring to light existing periodicities in the image. From a practical point of view, a DDP is similar to an EDP and is formed for a central point surrounded by different spots. The later spots correspond with the families of planes (hkl) that obey the Bragg's law, being a representation of the reciprocal space of the sample.

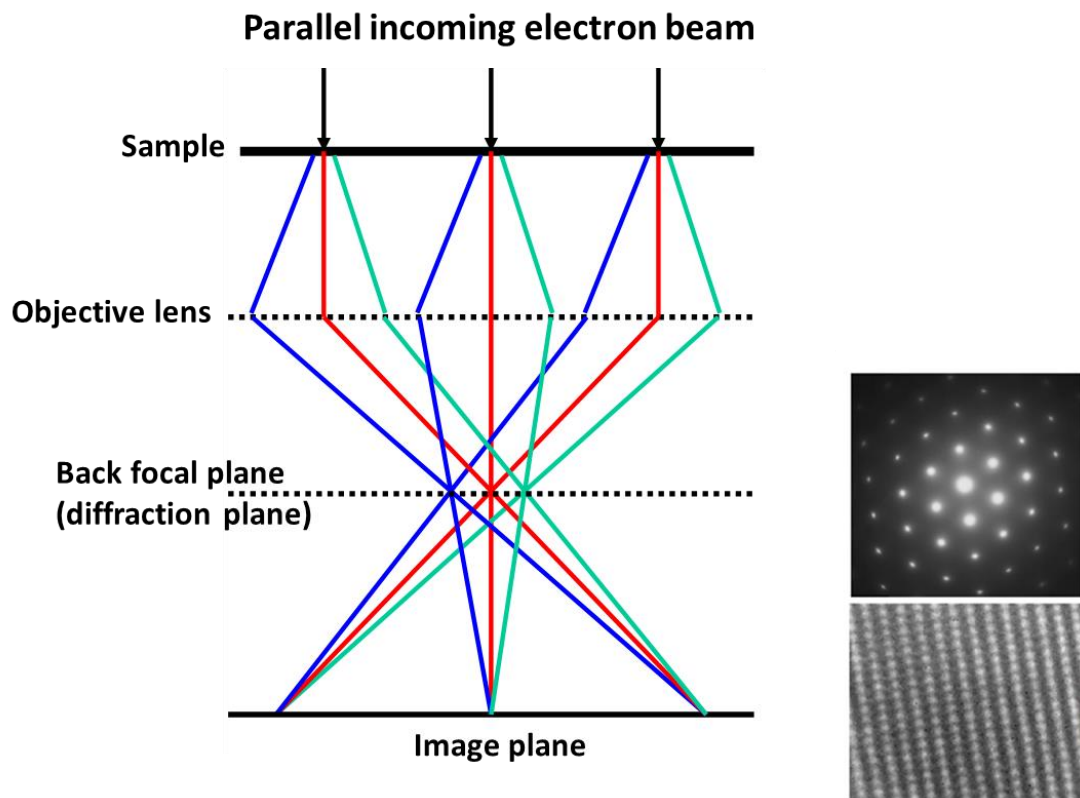


Fig. 2.10 Diagrams showing trajectories of electron beams after transmitting through a specimen in a TEM and the HREM image and diffraction pattern formation.

Scanning transmission electron microscopy (STEM)

The STEM mode⁽⁷⁾ is based on a converged beam that scan the sample. The electron beam can be scattered by Coulombic interactions with the electron cloud or the nucleus of the atoms present in the sample. The Coulombic attraction by the nucleus may cause electron to be scattered to higher angles or even backscattered (Figure 2.11). The scattered electrons can be collected, among others, by three types of detectors (Figure 2.9): Bright Field (BF), which is associated with electrons that have not modified their trajectories, the Annular Dark Field (ADF), that correspond with the electrons dispersed at low angle, and High Angle Annular Dark Field (HAADF), based in the detection of those electrons that have been dispersed elastically at high angle. We will focus on the later technique, since it was intensively used in this work.

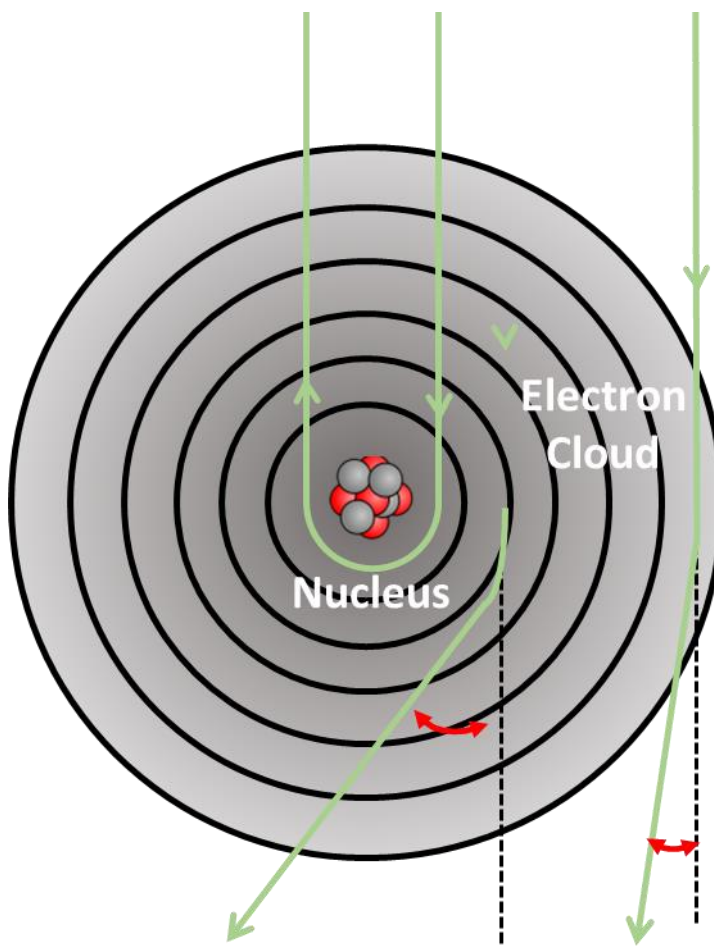


Fig. 2.11 Coulombic interaction of an isolated atom with the electron beam.

In contrast with the HREM method, the images that are obtained in HAADF-STEM are more intuitive, since the image intensity (I_{el}) is dependent of the electron beam intensity (I_0), the average atoms per area unit in the analysed volume (NT) and the cross section (σ_{el}). The chance of a particular electron undergoing any kind of interaction with an atom is determined by an interaction cross section. Each possible interaction has a different cross section which depends on the energy of the particle, in our case the beam energy.

$$I_{el} = I_0 NT \sigma_{el} \quad \text{Eq. 2.9}$$

The cross section is proportional to the effective atomic number (Z_{ef}), the speed of the light in the vacuum and also inversely proportional to the electron speed (v) and has units of area of the order of magnitude of 10^{-5} nm^2 .

$$\sigma_{el} = (1.87 \times 10^{-24} m^2) Z_{ef}^{4/3} (v/c)^{-2} \quad Eq. 2.10$$

On the other hand, the effective atomic number take in account the atomic number of the different atoms present in the sample (Z_i) and the atomic relations (f_i), that is the fraction of the total number of electrons associated with each element:

$$Z_{ef} = \frac{\sum i f_i Z_i^{1.3}}{\sum i f_i Z_i^{0.3}} \quad Eq. 2.11$$

Summarizing, the HAADF-STEM technique allows to obtain information related with the atomic number and the thickness of the sample. From a practical point of view, the contrast in HAADF-STEM images is originated by the difference of the effective atomic number of the elements those constitute the different particles, with particles containing heavy elements appearing brighter than particles containing elements with lower atom in number. It is obvious, therefore, the interest in using this technique for studying in detail the distribution of small heavy nanoparticles (such as Pt) on lighter supports (for instance TiO_2) and the morphology of the different nanoparticles.

Analytical information of the sample can be also obtained using a transmission electron microscope, considering the interaction between the beam and the sample. When the electron beam has enough energy to interact with the inner shell electrons of the atoms present in the sample, an electron might be extracted with the generation of a vacancy (Figure 2.12). This electronic configuration is an excited state of the atom, which will be relaxed when an electron will be transferred from an upper layer to the vacancy. During the atomic relaxation, a photon, with an energy in the range of X-rays, is emitted. These X-Rays are characteristic of the elements present in the sample and it is the bases of the Energy-dispersive X-ray spectroscopy (EDS). EDS spectra make possible to obtain qualitative and quantitative information on the chemical composition of the sample.

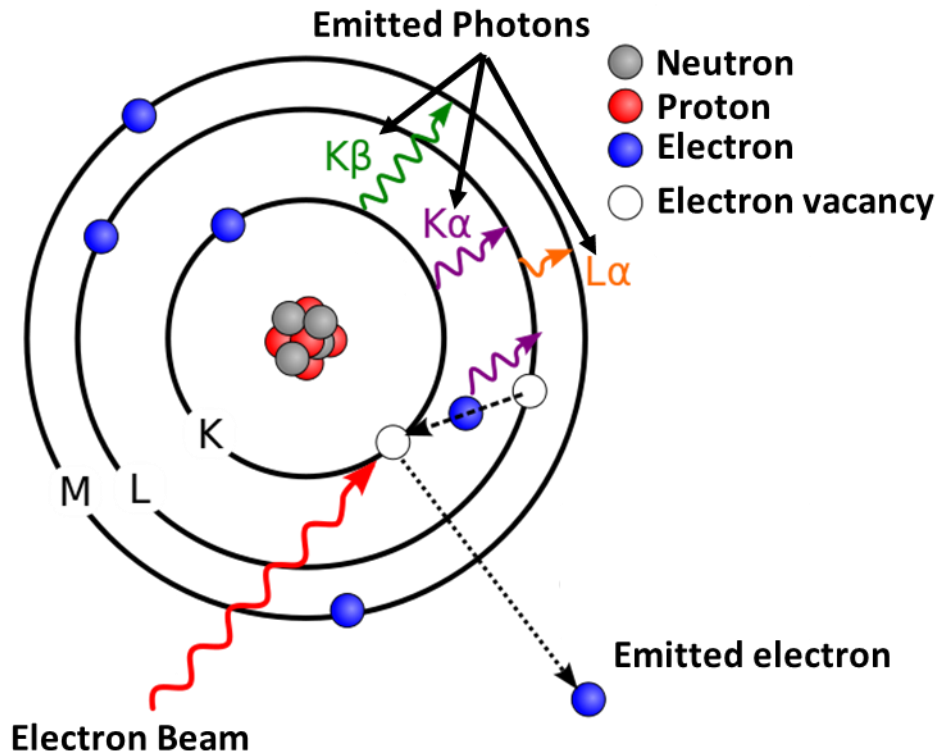


Fig. 2.12 Schematic representation of the interaction between the electron beam and the electronic structure of an isolated atom.

Finally, it would be worth to discuss the main limitations of the EM techniques employed in the thesis. The three main disadvantages of TEM are the following:

- Small volumes analysed.** The high resolution of electron microscopy makes unfeasible to analyse big volumes of the sample. Williams and Carter(9) have estimated that from the first implementation of TEM till 1996 a total volume of 0.6 mm^3 has been analysed by HRTEM. This emphasizes the need to study your sample on gradually decreasing scale and the big difficulties of studying heterogeneous samples.
- 2D dimension images.** TEM images are two-dimensional projections of 3D objects. We must be very cautious in interpreting shapes, and spatial relationships especially in the TEM. New 3D techniques, such as Electron Tomography, has been developed to take over this limitation.

However, the complex series acquisition and interpretation, make difficult to obtain a representative number of experiments.

- c. **Electron beam damage.** The high energy of the electron beam utilized in electron microscopy may causes damage by ionization⁽¹⁰⁾, radiolysis, and heating. In summary the electron beam can completely destroy the sample by amorphisation or melting and even evaporation. The electron beam can also modify the morphology of the metal nanoparticles and its interaction with the support. For this reason, electron beam dose must be adequately selected depending on the sample.

The electron microscopy studies carry out in the present thesis were performed at the University of Cadiz using an electron transmission microscope model Jeol-2010F. This microscope has field emission electron source and it can be operated with a voltage of 100 or 200 kV. The objective lens has an aberration coefficient of 0.5 mm and chromatic aberration coefficient of 1.1 mm. Furthermore, this electron microscope has a HAADF detector with a recollection inner angle of 80 and 213 mrad of exterior angle. In addition, an EDS spectrometer (Oxford Inca Energy-200) and a ELLS (Gif 2000 Gatan Imaging Filter) are attached. The HAADF images were obtained using a probe of 0.5 nm.

In the present work, a last generation aberration corrected electron microscope, FEI Titan Cubed Themis, was also used. This equipment includes a Super-X windowless EDX detector, which is able to detect elements with a concentration below 0.1%. This capability was used to localize the dopants in the TiO₂ nanosheets.

Finally, the interpretation of the DDPs, as well as the identification of crystalline phases, has been carried out using the Eje-Z® software which has been developed at Grupo de Estructura y Química de Nanomateriales, Facultad de Ciencias of University of Cádiz⁽¹¹⁾. This software allows to calculate theoretical EDP in cinematics conditions and obtain the distances and angles between different families of planes.

To prevent any alteration of the sample, a dry deposition method was used. This method consists on introducing in an Eppendorf a commercial lacey

carbon grid with a small amount of sample, and subsequently shake it for a few minutes. After that, the grid was observed in an optical microscope to determinate if the sample was properly deposited. The process was repeated until the sample partially and homogeneously cover the grid.

2.8 Catalytic activity: Ethanol photoreforming

The synthesized TiO₂ nanosheets and anatase/brookite nanorods catalyst were evaluated in the photocatalytic reforming of ethanol. The experiments were carried out in a homemade setup located at UNITS. A sketch of the equipment is included in Figure 2.13. The main parts of the equipment are the followings:

1. **Light source:** it is based on a Lot-Oriel Solar Simulator equipped with a 150 W Xe lamp and an Atmospheric Edge Filter (AM1.5) with a cut-off at 300 nm. The equipment was adequately aligned to obtain a circular collimated beam with an area of 19.63 cm². The incident irradiance was measured by a Delta Ohm HD 2302.0 Light Meter radiometer, being 25mW cm⁻² in the UV-A region and 180mW cm⁻² in the Vis–NIR range.
2. **Photoreactor:** The photocatalytic reaction take place in a Teflon reactor with a volume of 150 cm³. This part is placed inside of a stainless steel cylindrical body with a circular Kodial glass window of 50mm (19.6 cm²). The system has one inlet that was used to introduce a 15 ml/min flow of Ar to carry the reactions products to the analysis device.
3. **Magnetic stirring system:** It was fixed at 1500 rpm to guarantee a homogenous suspension of the catalyst in the reaction solution during the catalytic test.
4. **Thermostatic bath:** All the experiments were performed maintaining the reactor temperature at 25ºC using a thermostatic bath.
5. **Analytical system:** On-line detection of the products was carried out using an Agilent 7890A Gas Chromatograph (GC) equipped with two analytical lines:

- Permanent gases, including H₂, were quantified using a Carboxen 1010 PLOT column (Supelco, 30 m x 0.53 mm ID, 30 lm film) and a Thermal Conductivity Detector (TCD). Ar was used as carrier to improve the H₂ sensibility of the TCD detector.
- Volatile organic compounds were analysed by DB- 225 ms column (J&W, 60 m x 0.32 mm ID, 20 lm film) using He as carrier and followed by a mass spectrometer (MS) HP 5975C.

A 10 way-two loops injection valve was employed for introducing the samples into the GC during on-line analysis of the gaseous products.

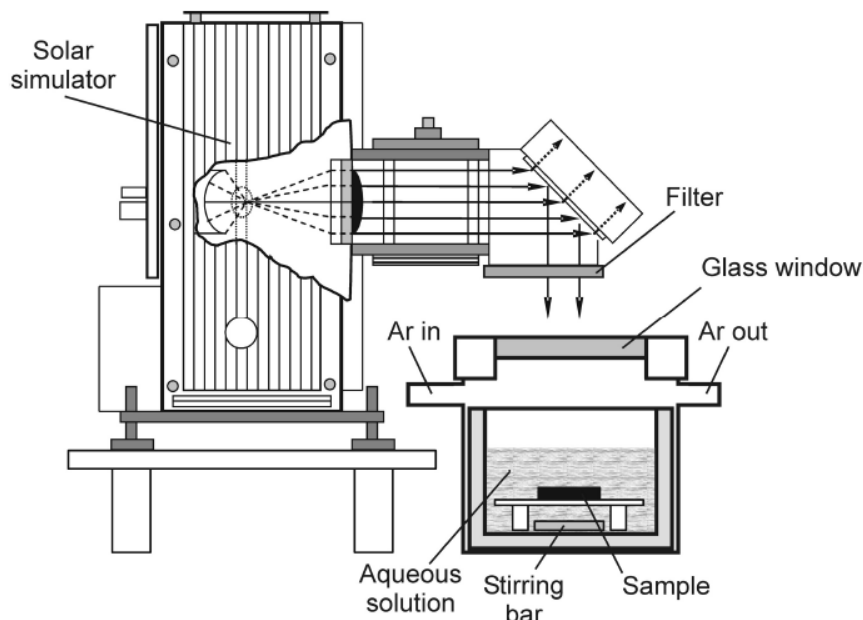


Fig.2.13 Schematic representation of the photocatalytic system used for the study of the ethanol photoreforming.

The procedure used in the catalytic tests consist on the following steps.

1. 50 mg of dried TiO₂ powder were suspended into EtOH 96% (80 mL) and 20 µl of an aqueous solution of Pt(NO₃)₂ (5 mg Pt ml⁻¹) were added in order to obtain a final metal loading of 0.2 wt.%.

2. The system was purged with Ar for 30 min to remove the air before switching-on the lamp. During the photocatalytic experiments, the reactor was continuously flushed with Ar ($15 \text{ ml}\cdot\text{min}^{-1}$) to transfer the products present in the gas phase to the analytical apparatus.
3. The liquid phase after the photocatalytic test was collected by filtration on a $0.45 \mu\text{m}$ PVDF Millipore membrane and analysed by GC/MS using 1-butanol as internal standard.

2.9 Catalytic activity: Evaluation of the self-cleaning capacity of TiO₂-SiO₂ nanocoatings

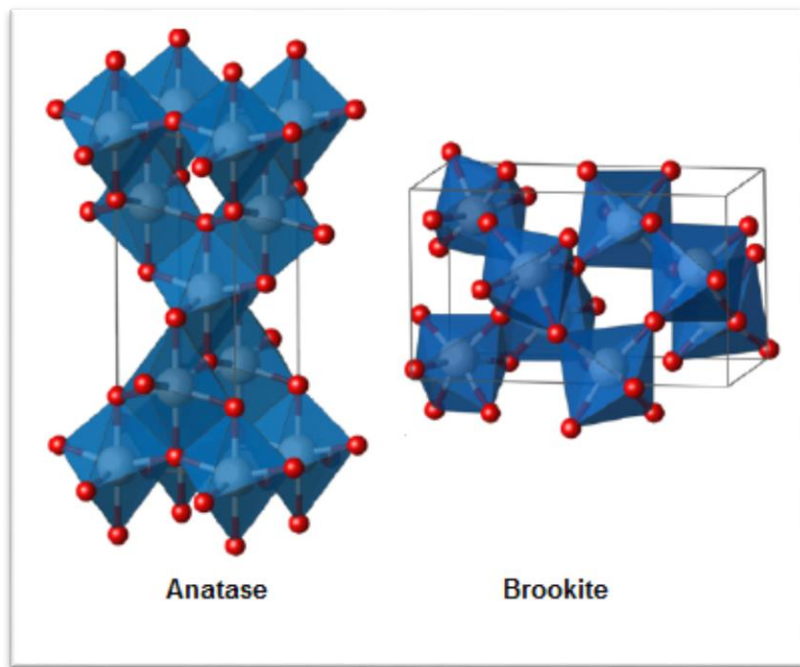
The self-cleaning capacity of TiO₂-SiO₂ nanocoatings was evaluated by depositing them onto limestone and performing a methylene blue degradation test. The TiO₂-SiO₂ nanocoatings were deposited by spraying onto the surfaces of the limestones until saturation. The stone samples were then dried under laboratory conditions until reaching constant weight.

The photo-degradation tests were carried out in the SolarBox (Vilber Lourmat CN15.CL chamber) with a Xenon lamp at 500 w/m^2 , 50°C and a relative humidity of 30 %. The stone samples were cut in the form of $5 \text{ cm} \times 5 \text{ cm} \times 2 \text{ cm}$ blocks. Then 0.25 ml of a solution of methylene blue in ethanol was deposited on treated stone specimens. Next, stone samples were irradiated with UV in the SolarBox.

Colour variations were obtained as a function of irradiation time using a solid reflection spectrophotometer Colorflex from Hunterlab. The conditions used were C illuminate mode and observer at 10° . CIE La*b* colour space was used and variations in colour were evaluated using the parameter total colour difference (ΔE^*). This catalytic test equipment is located at the Physical-Chemistry Department at the University of Cadiz.

References

1. Brunauer S, Emmett PH, Teller E. Adsorption of Gases in Multimolecular Layers. *J Am Chem Soc.* 1938;60(1):309–19.
2. Sing K. The use of nitrogen adsorption for the characterisation of porous materials. *Colloids Surfaces A Physicochem Eng Asp.* 2001;187–188:3–9.
3. Lin H, Huang CP, Li W, Ni C, Shah SI, Tseng YH. Size dependency of nanocrystalline TiO₂ on its optical property and photocatalytic reactivity exemplified by 2-chlorophenol. *Appl Catal B Environ.* 2006;68(1–2):1–11.
4. Gupta SM, Tripathi M. A review of TiO₂ nanoparticles. *Chinese Sci Bull.* 2011;56(16):1639–57.
5. Tauc J. *Phys. stat. sol.* 15, 627 (1966).pdf.
6. Wikipedia. Wikipedia X-ray photoelectron spectroscopy (XPS) [Internet]. Collaborators from wikipedia. 2014. Available from: https://en.wikipedia.org/wiki/X-ray_photoelectron_spectroscopy
7. Watt IM. The principles and practice of electron microscopy. 2nd ed. Cambridge University Press; 1997. 484 p.
8. Yang JC, Small MW, Grieshaber R V, Nuzzo RG. Recent developments and applications of electron microscopy to heterogeneous catalysis. *Chem Soc Rev.* 2012 Dec 21;41(24):8179–94.
9. Carter W and. Transmission Electron Microscopy: A Textbook for Materials Science. 2nd editio. 2009. 760 p.
10. Tian F, Li Y, Xing J, Tian H, Whitmore L, Yang H, et al. Pores on TiO₂ nanosheets with exposed high active facets. *Mater Lett.* 2014;123:254–7.
11. José A. Pérez-Omil. Eje Z. University of Cádiz; 2016.



Anatase/Brookite nanocomposites

3. Anatase/Brookite nanocomposite

The synergistic effect of multiphasic TiO₂ materials have been reported as beneficial for several photocatalytic processes, such as abatement and mineralization of pollutant compounds⁽¹⁻³⁾ or H₂ production by photoreforming^(4,5). The study of nanostructured well-defined TiO₂ photocatalysts⁽⁶⁾ is becoming a very relevant research area, even if the use of brookite with a controlled morphology⁽⁷⁾ is still rare⁽⁸⁻¹⁵⁾. In this chapter it is reported the synthesis of TiO₂ anatase/brookite nanocomposite material in order to prove its efficiency with respect to H₂ production by ethanol photo-dehydrogenation under simulated solar light irradiation. It was studied the effect of the phase composition of the photocatalytic material and the influence of the calcination protocol during the synthesis process of the nanomaterials. Pt nanoparticles were photo-deposited as co-catalyst and the average size of nanoparticles were measured in order to study the effect of their size on the photoactivity. Finally, the photocatalytic activity of the synthesized materials was compare with that of the benchmark Degussa P25 multiphasic TiO₂ material.

3.1 Synthesis of anatase/brookite nanorods

TiO₂ anatase/brookite nanocomposites were synthesized from Na-titanate adapting the procedure reported by Li et al⁽¹⁶⁾ for the preparation of anatase nanorods. Briefly, the Na-titanate precursor was synthesized by hydrothermal treatment of the commercial Degussa P25 TiO₂ (750 mg) at 120 °C for 24 h in a 45 mL Teflon-lined autoclave containing a NaOH 10 M solution (30 mL). The white precipitate was collected by centrifugation, washed several times with bidistilled water until the solution pH decreases below 11 and subsequently dried at 80 °C overnight. Anatase/brookite nanocomposites were then synthesized by hydrothermal transformation of the dry Na-titanate precursor. Specifically, a 45 mL Teflon-lined autoclave was charged with 30 mL of bidistilled water and a selected amount of Na-titanate, magnetically stirring for 1 h. The hydrothermal process was performed putting the autoclave into a pre-heated oven at 200 °C for the desired time. In the table 3.1 are shown the synthesis conditions parameters of the prepared samples. The characterization of the obtained materials allowed us to correlate the parameters employed during the synthesis with the morphological and structural characteristics and the photocatalytic performances in H₂ production evaluated by means of the ethanol photo dehydrogenation reaction.

Table 3.1 Synthesis conditions of the prepared samples. B1* and C3* are the same samples.

Sample	Na-titanate/water ratio (mg / mL)	Time (h)	Heating method
A1	27	24	Convection
A2	53	24	Convection
A3	100	24	Convection
B1	27	24	Irradiation
B2 *	53	24	Irradiation
B3	100	24	Irradiation
C1	53	12	Irradiation
C2	53	18	Irradiation
C3*	53	24	Irradiation
C4	53	30	Irradiation
C5	53	36	Irradiation
C6	53	42	Irradiation
C7	53	48	Irradiation

3.2 Characterization by XRD: phase composition and crystallite size

The precursor produced by reaction of TiO₂ P25 in NaOH has been analysed by XRD. The obtained pattern is presented in Figure 3.1. Despite the low intensity and the broad reflection obtained, this pattern can be resembling that of Na₂Ti₂O₅. *Zhao et. al* ⁽¹⁷⁾ reported the formation of Na₂Ti₂O₅ and Na₂Ti₃O₇ by the hydrolysis reaction of Ti(nBuO)₄ under hydrothermal treatment

at 180°C for 24h in NaOH with concentration of 6M and 10M, respectively. Reasonably, considering the synthesis conditions adopted in the present work (reaction between TiO₂ and NaOH 10M at a lower temperature – 120°C), a higher NaOH concentration could be required to produce Na₂Ti₂O₅ and the presence of amorphous material cannot be excluded.

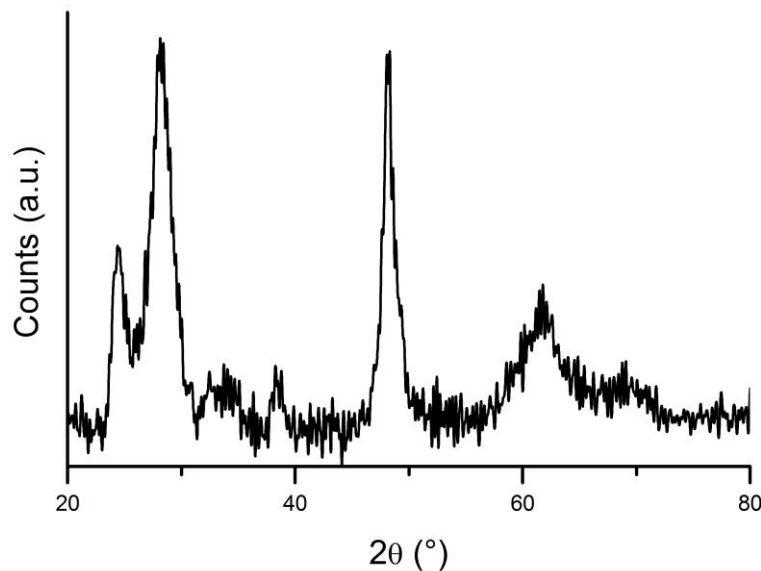
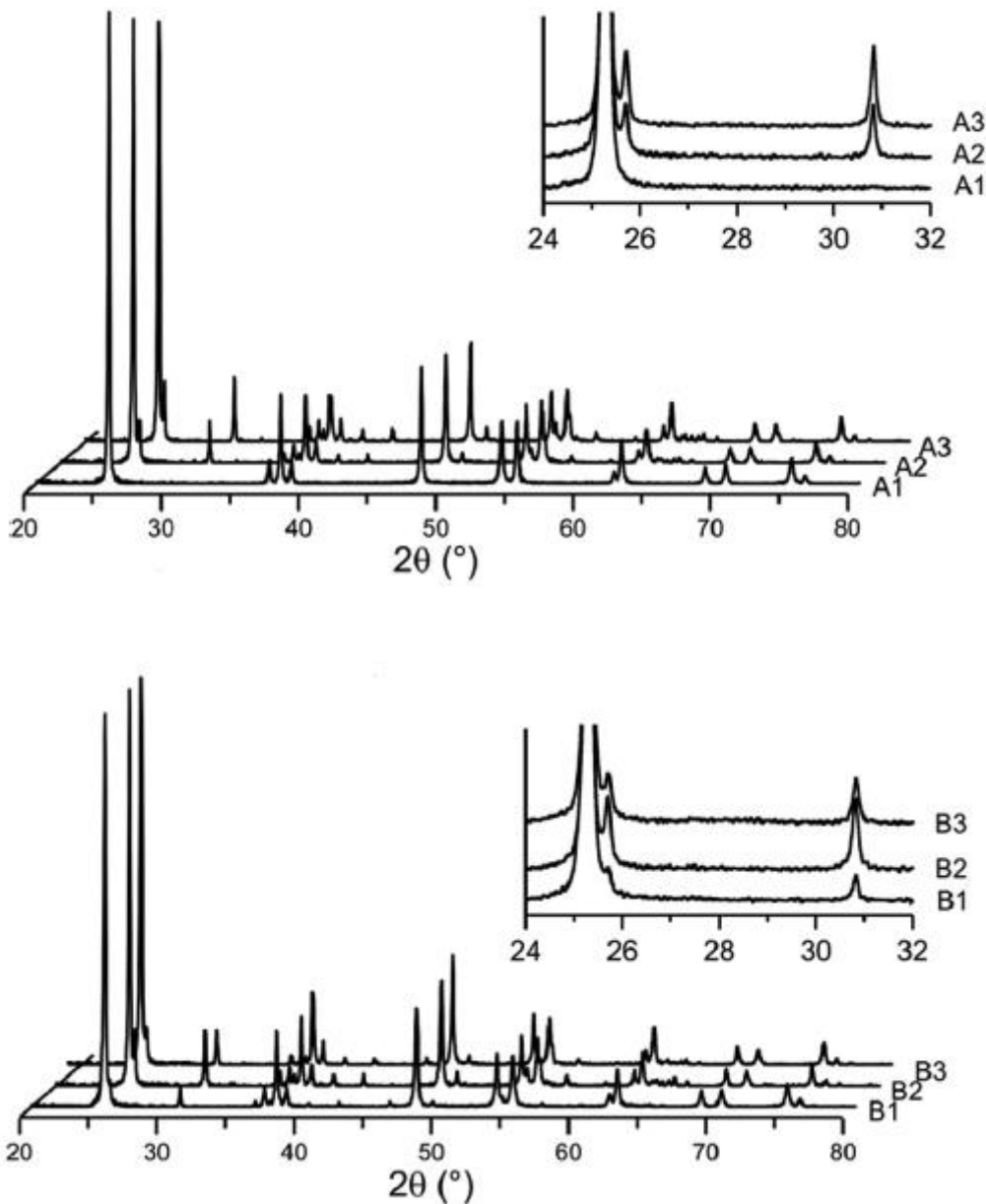


Fig. 3.1 Powder XRD pattern of precursor prepared by reaction of TiO₂ P25 into NaOH 10M at 120°C for 24h.

The XRD patterns of the samples prepared by hydrolysis of the Na₂Ti₂O₅ precursors are presented in Figure 3.2. The insets show the magnification of the 2θ region where the most intense reflections of brookite are present, in order to appreciate the evolution of the brookite content in the different sets of samples.

All the samples have well defined and resolved reflections related to anatase and brookite phases that indicated a high degree of crystallization. No detected reflections related to rutile phase and/or Na-titanate materials have been detected, although the amorphous/nanocrystalline residual precursor could be hardly detected by powder XRD.



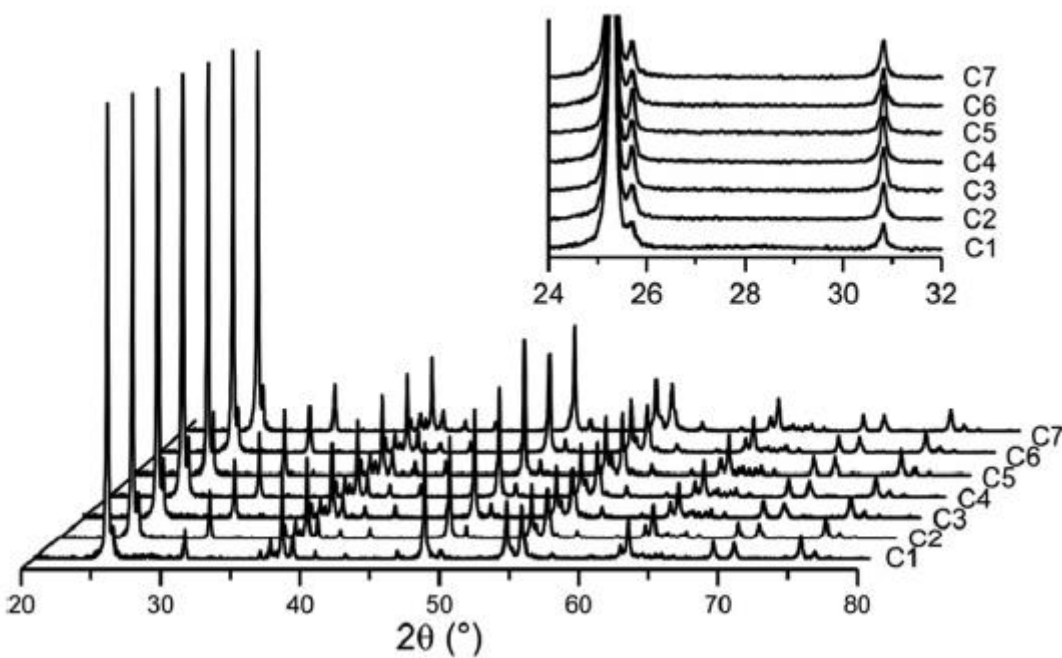


Fig. 3.2 Powder XRD pattern of all the prepared samples.

The anatase/brookite phase composition, determined by Rietveld analysis of the XRD patterns, and the mean crystallite sizes, calculated applying the Scherrer equation to the main reflections of each phase, are summarized in Table 3.2. Regardless of the heating method used in the synthesis (convection or radiation) of the samples series A- and B-, the amount of brookite phase and the average size of the crystallites increases when the Na-titanate/water ratio increases.

The C-series samples allows to study the influence of the duration of the hydrothermal process on phase composition, morphology and texture. It is possible to observe that there is an initial decrease of the content of the anatase phase and a parallel increase of the brookite phase (Tab. 3.2). This can be associated to a transformation of the residual $\text{Na}_2\text{Ti}_2\text{O}_5$ (see later). The mean crystallite size of the brookite phase decrease to a minimum of about 80 nm for 24-30 h of hydrothermal treatment. Longer hydrothermal treatments slightly decrease the content of the brookite with an increase of its mean crystallite size.

On the other hand, it can observe that the parameters of the synthesis (time for hydrothermal treatment and the heating method) appear to have little influence on the anatase phase.

Table 3.2 Results from XRD analysis and Kr physisorption.

Sample	Phase composition (%)		Average crystallite size (nm)		Surface area (m ² /g)
	Anatase	Brookite	Anatase	Brookite	
A1	100	---	61	---	7.2
A2	83	17	55	120	6.2
A3	73	27	72	117	8.5
B1	92	8	50	64	10.3
B2	69	31	64	89	5.7
B3	73	28	63	155	8.4
C1	88	12	61	253	74.4
C2	75	25	64	107	21.5
C3	69	31	64	89	5.7
C4	68	32	65	77	5.2
C5	71	29	66	85	6.1
C6	74	26	62	143	4.9
C7	77	23	63	275	5.0

3.3 Characterization by Raman spectroscopy

Raman spectroscopy allows detecting the presence of small amounts of amorphous phases. The collected spectrums are presented in Figure 3.3, confirming the trends observed by XRD measurements.

The presence of anatase is revealed by the bands at 143, 195, 395, 515 and 639 cm⁻¹ while the bands at 213, 245, 282, 320, 365, 456, 502, 545 and 584 cm⁻¹ are characteristic of brookite⁽¹⁸⁾. All the collected spectra are dominated by the very intense band of anatase at 143 cm⁻¹. This intense band has been removed from the spectra presented in Figure 3.3 to better appreciate the contribution of the less intense bands of the brookite.

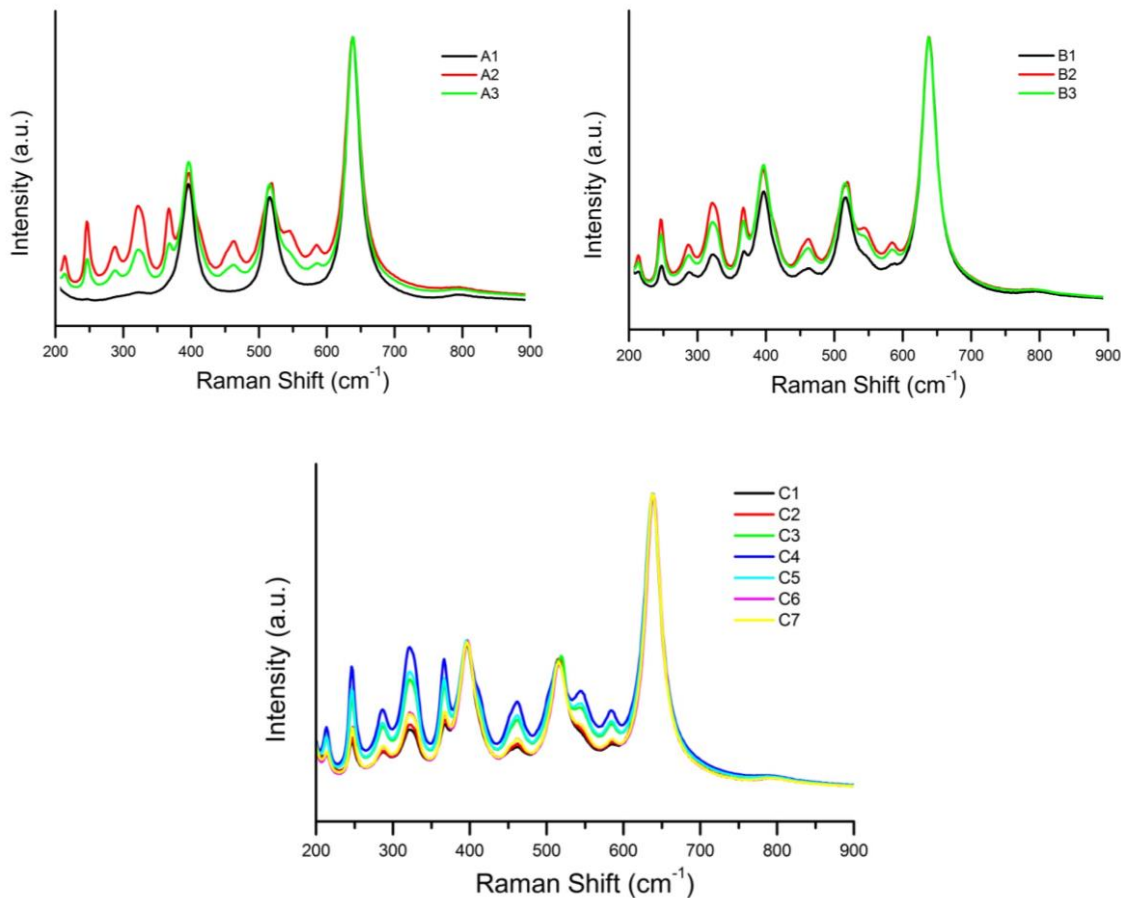


Fig. 3.3 Raman spectra of all the prepared samples. The anatase band at 143 cm^{-1} is omitted for clarity. Spectra are normalized with respect to the intensity of the anatase band at 639 cm^{-1} .

3.4 Textural analysis

Table 3.2 also includes the results of surface area measurements, performed adsorbing Kr at the liquid nitrogen temperature. Notably, the precursor $\text{Na}_2\text{Ti}_2\text{O}_5$ used for the synthesis of the anatase/brookite composites revealed a high surface area ($84 \text{ m}^2/\text{g}$).

From the data reported in Table 3.2, it is evident that the BET surface area for the samples of A and B series are very low, independently of the phase composition. For the samples of C series, in which the Na-titanate/water ratio was kept constant, the BET surface area decreases in the first 24h of hydrothermal treatment, being constant for longer hydrothermal treatments. The

high BET surface area of C1 sample can be related to the presence of unreacted Na-titanate. The decrease of surface area up to 24h of hydrothermal reaction suggests that, during this time, the principal transformations of $\text{Na}_2\text{Ti}_2\text{O}_5$ into TiO_2 anatase/brookite nanocomposite take place, finally reaching the complete conversion of the precursor.

3.5 Mechanism of formation of anatase/brookite nanocomposites

The transformation of the Na-titanate precursor into TiO_2 anatase/brookite nanocomposite can be explained taking into account the crystal structure of the involved materials. The titanate precursor $\text{Na}_2\text{Ti}_2\text{O}_5$ consists of negatively charged layers made of TiO_6 octahedrons linked through the edges and spaced by Na^+ ions. In the anatase structure, each octahedron couples to eight neighbors with four sharing an edge and four sharing a corner. The brookite structure is built up of distorted octahedral with a titanium ion at the center and oxygen ions at each of the six vertices. Each octahedron shares three edges with adjoining octahedra, forming an orthorhombic structure.

Figure 3.4 presents a possible schematic mechanism, showing the single steps involved in the transformation of $\text{Na}_2\text{Ti}_2\text{O}_5$ into anatase or brookite.

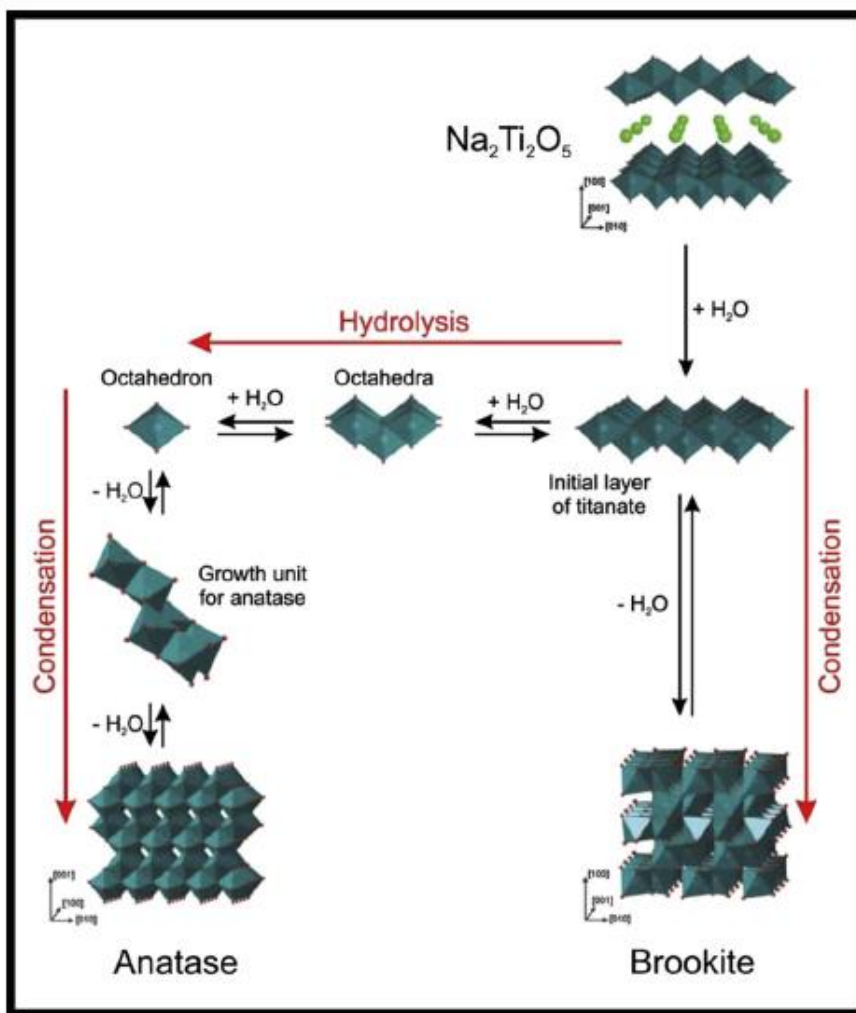


Fig.3.4 Proposed transformations taking place during the hydrothermal treatment of $\text{Na}_2\text{Ti}_2\text{O}_5$.

Conversion for $\text{Na}_2\text{Ti}_2\text{O}_5$ into TiO_2 starts by exfoliation of titanate layers of the initial material, with hydrolysis and release of NaOH , which progressively increases the pH of the solution. Brookite is formed by condensation of the exfoliated layers through the octahedron vertices, following the “Ostwald’s step rule”^(17,19). In fact, brookite is the phase having the most similar structure and, therefore, the nearest free energy compared to the precursor (the exfoliated titanate layers).

The formation of the anatase phase takes place through the complete hydrolysis of the Na-titanate precursor until the TiO_6 octahedrons are formed and their subsequent condensation through the edges. In this case the

transformation of the Na-titanate precursor follows the Ostwald's ripening, providing the most stable product.

The data on the C-series samples in Tables 3.1 and 3.2 suggest that, during the first 24h of hydrothermal treatment, the titanate precursor is initially transformed into anatase. As the reaction time increases from 12 to 30h, there is a gradual increase in the presence of brookite phase in the samples. After 12h of reaction, the pH of the solution is approximately 11, ideal conditions for the slow growth of brookite. As the hydrothermal treatment proceeds, more NaOH is released in the solution, increasing the pH and therefore favoring the formation of the brookite phase until the titanate precursor is completely consumed⁽²⁰⁾.

For hydrothermal treatments longer than 30h, the amount of anatase phase slightly increases. In this case, the brookite is slowly transformed into anatase by means of hydrolysis and re-condensation. The mean crystallite size of brookite increases for hydrothermal treatments longer than 24h. This result suggests that the smallest brookite crystals are subjected to the re-dissolution, leading to the growth of larger brookite crystals and/or to their hydrolysis and transformation into anatase phase.

Although it is known that the rutile phase is the most thermodynamically stable TiO₂ polymorph, the relative stability of the anatase and brookite is still a topic of discussion. This experimental data obtained in this study suggests that the anatase phase seems to be the most stable phase with respect to brookite phase, at least under these reactions conditions (temperature, pH, and presence of Na⁺). In fact, it is reasonable that the relative stability of the two metastable polymorphs depends on numerous factors, including the crystallite size, the exposed faces and the presence of adsorbates on the surface⁽²¹⁾.

3.6 Structural and morphological characterizations by Electron Microscopy

A wide and representative set of the prepared samples were studied by advanced electron microscopy techniques such as HREM and HAADF. The morphologies of the samples were studied to highlight the influence of the synthetic parameters on size and shape of the nanocrystals. From the analysis of the electron microscopy data, it is observed that all samples exhibit a high degree of crystallinity and large particles sizes. This is in accordance with the previously discussed XRD and surface area data (Table 3.2 and Figure 3.2).

The HAADF images for representative samples are shown in Figure 3.5. In general, two types of TiO_2 particles can be distinguished for the anatase/brookite nanocomposites: polycrystalline elongated particles and polycrystalline and polyhedral clusters. Representative HAADF-STEM images of selected samples, shown in Figure 3.5 highlight how ratio of the two types of structure depends on phase composition of the materials. Moreover, EDX analysis has been employed to reveal the possible presence of unconverted Na-titanate precursor, looking to Na signal.

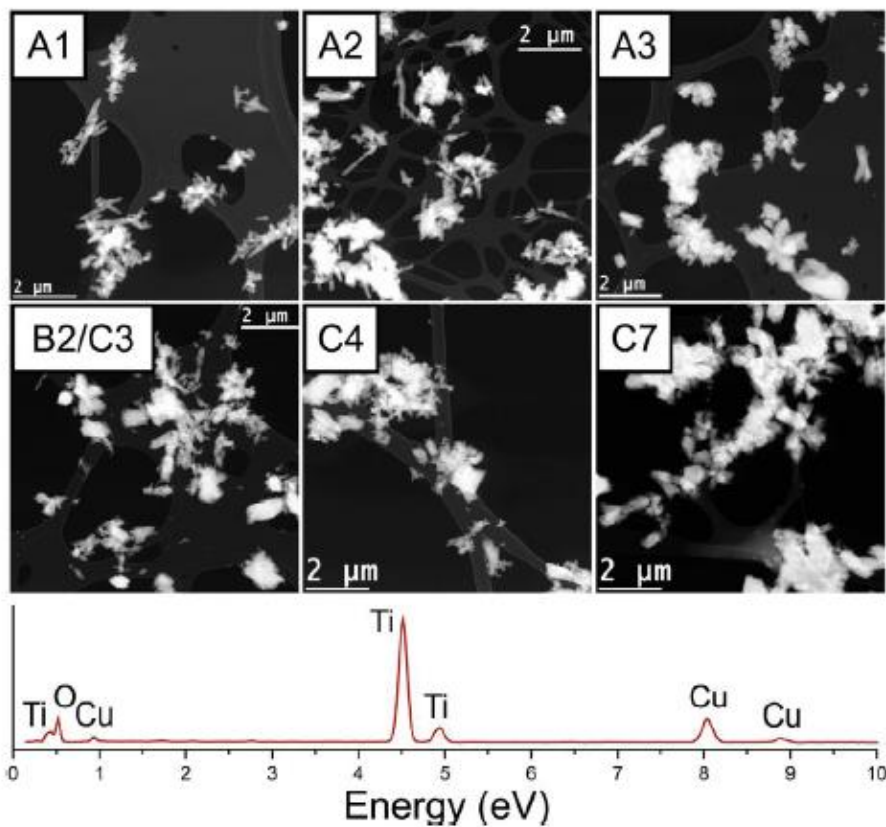


Fig. 3.5 Representative HAADF-STEM images of selected samples to highlight the evolution of the morphology of the TiO₂ nanocomposite materials. A typical EDX spectrum taken on the well-defined nanocrystals shows the absence of clear peaks related to Na.

A1 sample prepared using the lower titanate/water ratio, have uniform polycrystalline elongated particles with a mean size in agreement with the calculated in XRD. A2 samples present some polycrystalline and polyhedral cluster (100nm-1.5μm) due to the increase of the titanate/water ratio. In the sample A3, which has the higher titanate/water ratio within series-A samples, the amount polycrystalline and polyhedral cluster becomes preponderant. A similar trend is observed for the samples of series B, although some polyhedral cluster (100nm-1μm) are observed also in B1 sample, prepared with the lower titanate/water ratio. EDX analysis performed on the samples of series A and B did not detect any appreciable amounts of Na (see Figure 3.5), indicating that the Na₂Ti₂O₅ precursor has been fully converted into TiO₂.

In the C-series (Figure 3.6) in which the time of the hydrothermal treatment was changed and the ratio Na-titanate/water was maintained constant, it was observed morphological change in the anatase/brookite composite. In samples C1 and C2 (12-18h hydrothermal treatment) appears the particles with nanotube morphology and the EDX analysis of this nanotubes reveals high content of Na in comparison with the previously studied samples A and B. The samples C1 and C2 have the higher surface area of all the samples. In the rest of this series was not observed nanotubes morphologies, only the presence of polycrystalline and polyhedral clusters (100nm-2μm) similar to those seem in samples A2, A3 and B series. From the EDS analysis of the samples C3-C7, lower amounts of Na or its absence were detected. In view of the results, it can conclude that the Na-titanate needs more than 24h to be completely converted in TiO_2 .

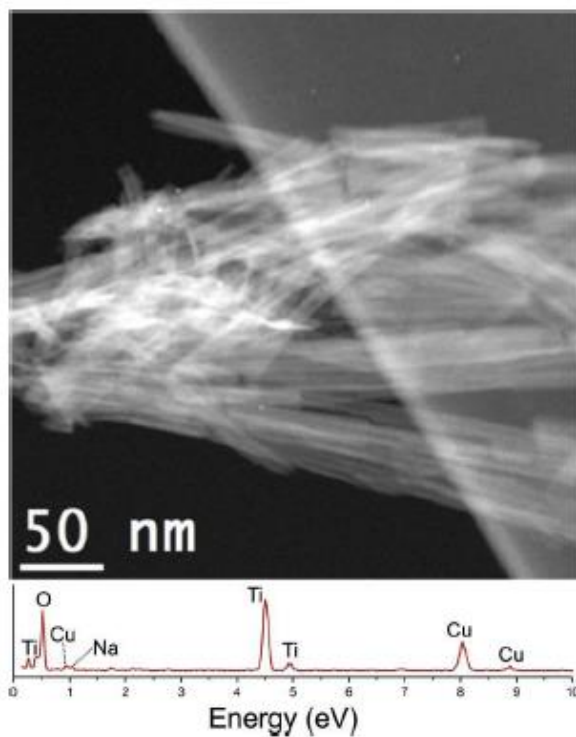


Fig. 3.6 Image of a selected portion of the sample C1, evidencing the presence of nanotube morphology. The EDX spectrum taken in this area shows an amount of Na significantly higher than in the rest on the material (see fig.3.5)

The identification of the crystallographic phase of several individual particles has been attempted in order to find a correlation between the nature of the polymorph and the morphology of the TiO₂ particles. For this reason, the digital diffraction patterns (DDP) obtained from TEM images were compared with the theoretical ones, simulated by different orientations of TiO₂ crystal structures. Unfortunately, only in a few number of cases the identification was univocally achieved, because of the overlapping of the crystallites in the nanocomposite materials and the similar spacing present in both phases.

Figure 3.7 shows two representative example of the studied samples, in which are not possible to distinguish between anatase and brookite phase because of the coincidence between some DDP of the two phases. In fact, the experimental DDP obtained from a HR-TEM image of a particle oriented in the right direction (Figure 3.7, insets in left parts) well agrees with the theoretical DDP calculated with Eje-Z® software (Figure 3.7, right parts). In the first case, the particle can be recognized as anatase oriented along the (001) direction or brookite oriented along the (111) direction. In the second case, the particle can be recognized as anatase oriented along the (131) direction or brookite oriented along the (112) direction. Figure 3.8 shows two examples of the studied samples in which were possible to identify unambiguously the anatase phase and brookite phase in the same sample. In the first case the particle was recognized as anatase oriented along the (111) direction. In the second case the particle was identified as brookite oriented along the (121) directions. In both cases only the phase identified was possible without any other possible phase identification.

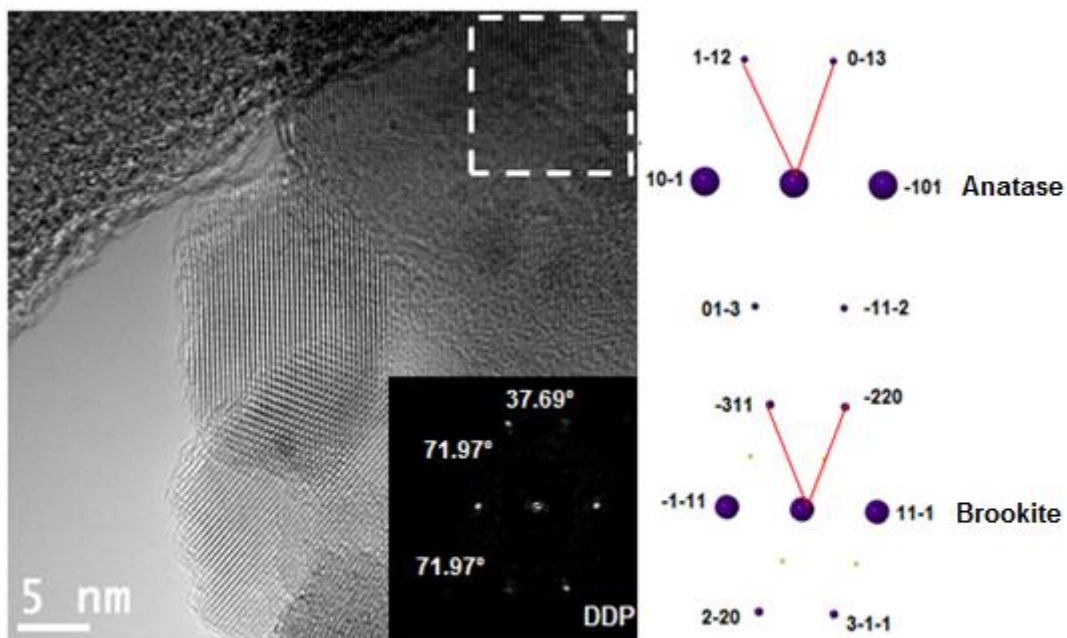
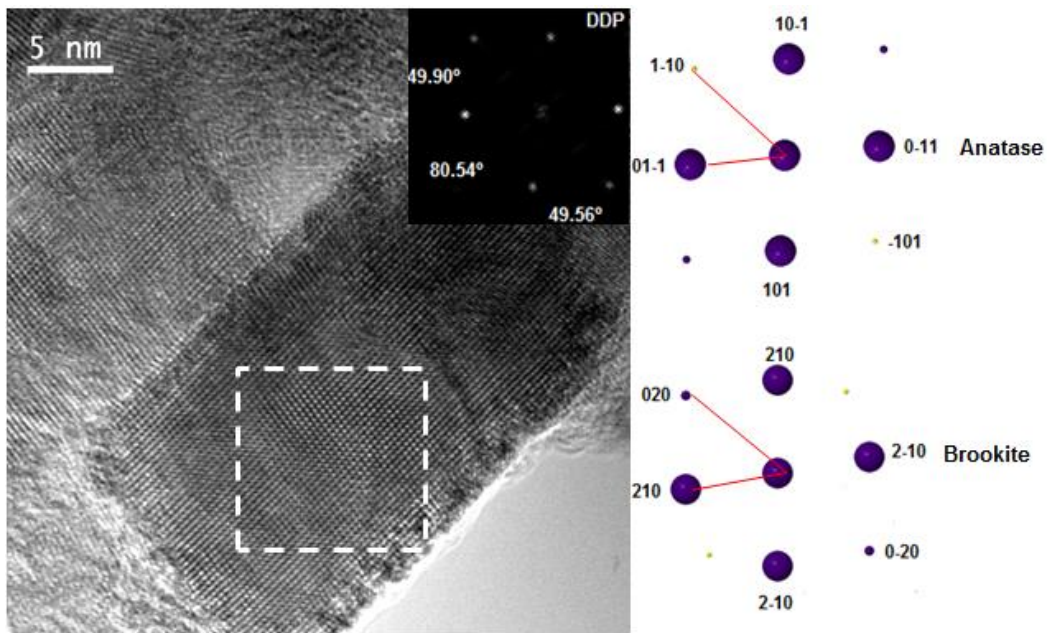
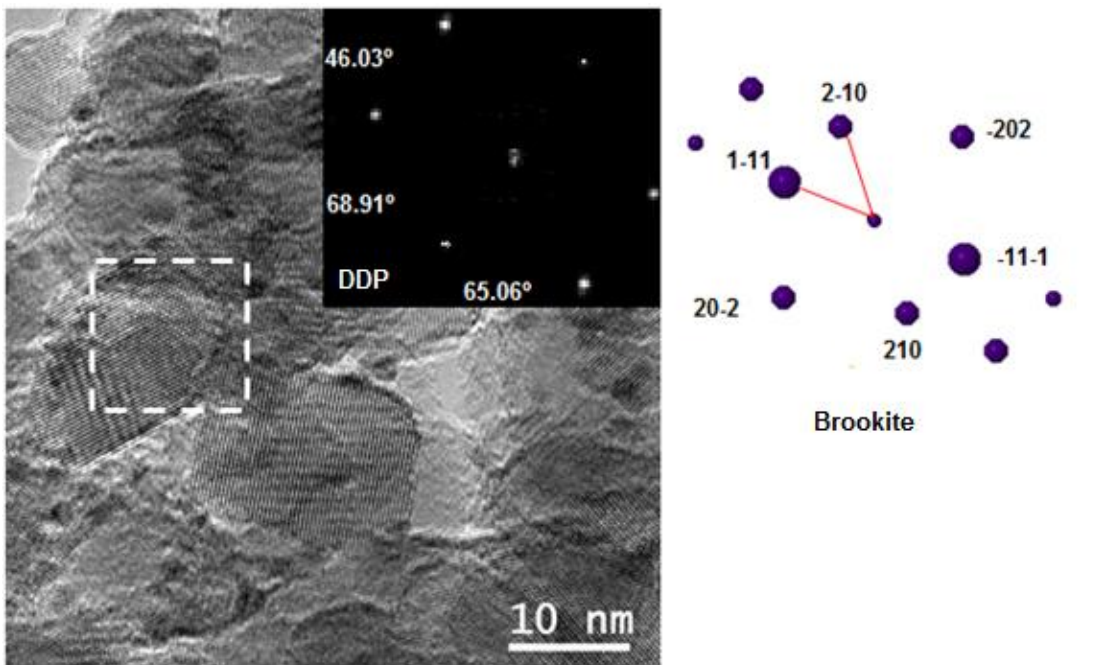
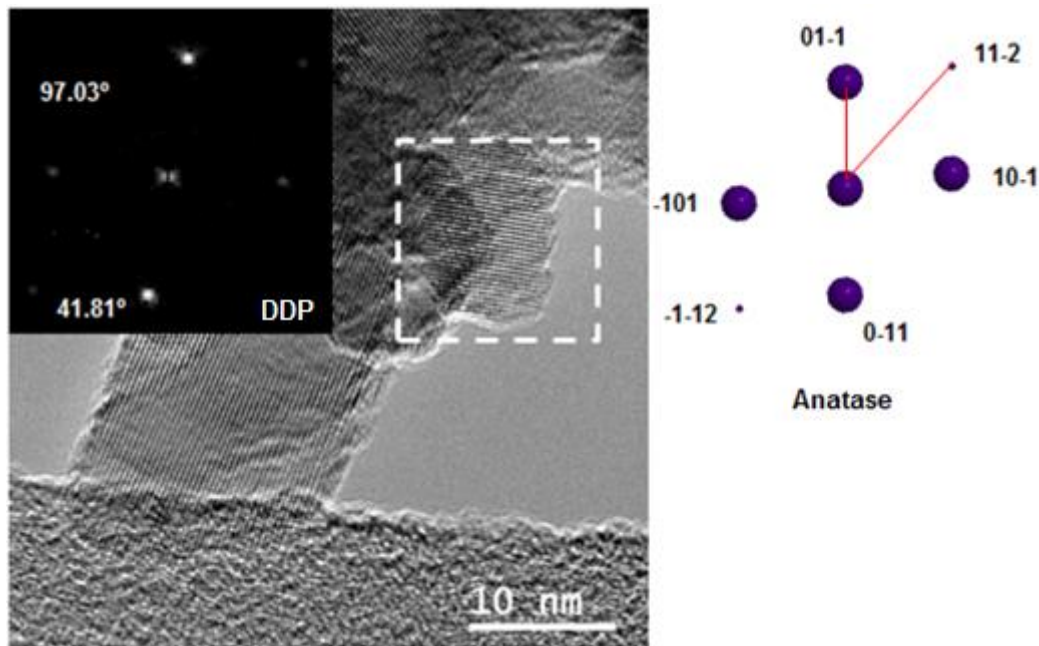


Fig.3.7 HREM images in which are not possible to distinguish between anatase and brookite phase. The inset white dashed square is the selected area for the digital diffraction pattern (DDP).



Phase	Zone axis [uvw]	distance $hkl_1 \wedge hkl_2$ (\AA)
Brookite	1.2.1.	3.51 \wedge 3.46 \rightarrow 45.75



Phase	Zone axis [uvw]	distance $hkl_1 \wedge hkl_2$ (\AA)
Anatase	1.1.1.	3.32 \wedge 2.25 \rightarrow 41.08

Fig.3.8 HREM images in which are possible to distinguish between anatase and brookite phase. The inset white dashed square is the selected area for the digital diffraction pattern (DDP).

Nowadays, the combination of transmission electron microscopy with electron energy-loss spectroscopy (EELS) is a convenient means of phase analysis. EELS analysis is particularly well adapted for local studies of small areas, a few nanometers in size, in heterogeneous samples. The phase identification by EELS was not possible because the spectral resolution did not allow us to distinguish between the anatase phase and brookite phase.

3.7 Analysis of Pt nanoparticle size distribution

The analysis by HREM of the samples (Figure 3.9) show the presence of a large amount of Pt nanoparticles deposited on the TiO₂ matrix. The Pt nanoparticles are single crystals, as revealed by the presence of lattice fringes in the HREM pictures.

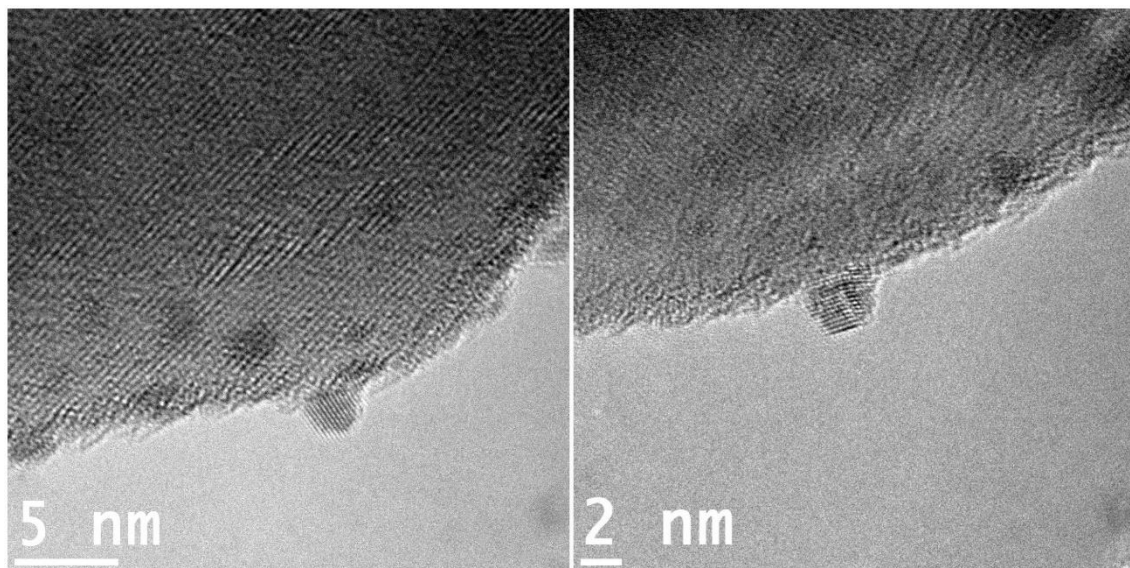


Fig. 3.9 Representative HRTEM images showing the crystalline nature of the Pt nanoparticles.

Figure 3.10 show representative HAADF-STEM images of various samples, in order to appreciate the dispersion of the Pt nanoparticles (bright spot) on the surface of the TiO₂ support. There are TiO₂ particles on which Pt nanoparticles are almost absent (i.e., A1, A3, and C4) and particles of TiO₂ homogenously covered by Pt. In some samples (B2/C3 and C1) the position of Pt nanoparticles on the titania are concentrated in particular regions of the TiO₂ support (boundaries or corners). This phenomenon can be explained by the localization of the electrons in specify areas of the TiO₂^(17,19,22–29). It is known

that electrons needed to reduce the Pt ions on the titania support forming the Pt nanoparticles migrate preferentially on specific facets, while holes are accumulated in other ones^(22,30). Therefore, the dispersion of Pt nanoparticles on the surface of a polycrystalline TiO₂ material can be not homogeneous, with higher concentration on particular crystal facets and/or at the interphase between different crystallites, where electron/hole separation is favoured.

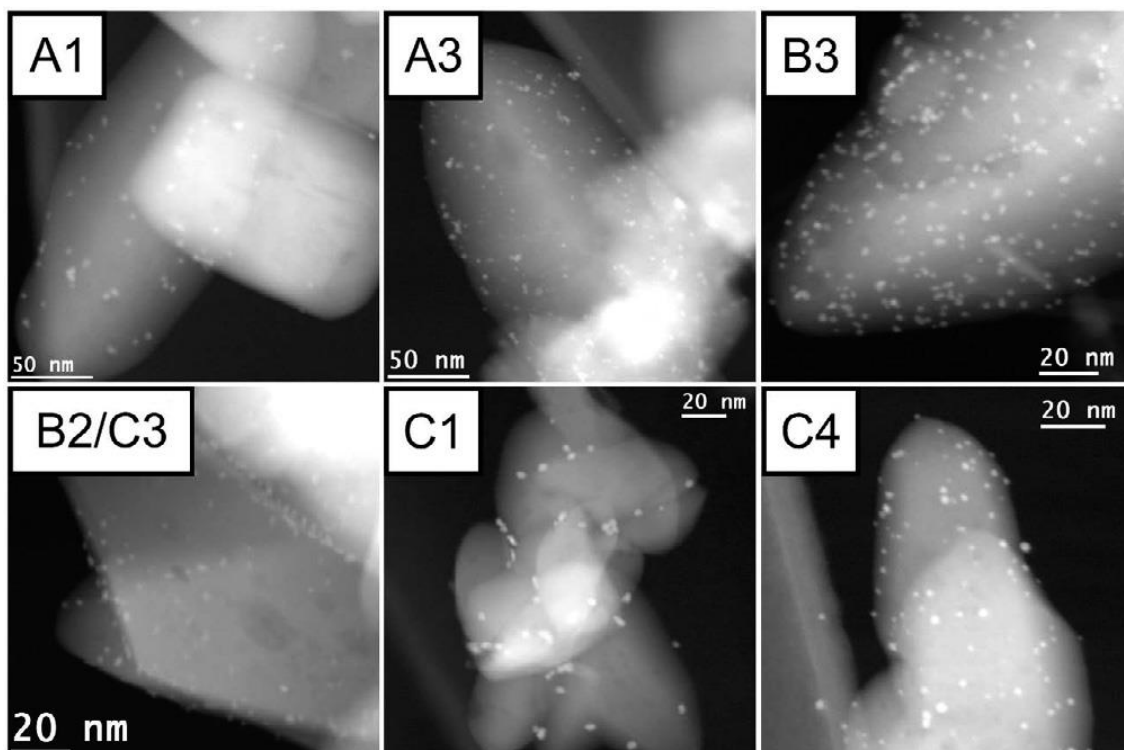


Fig.3.10 Representative HAADF-STEM images collected on selected samples, showing the Pt nanoparticles after photodeposition on the TiO₂ supports.

Size distributions of the Pt nanoparticles are summarized in Figure 3.11. The mean size of Pt nanoparticles is 2.0-2.5 nm for the samples prepared using a TiO₂ anatase/brookite support. On the other hand, the mean size of the Pt nanoparticles is 4-6 nm for the samples A1 and A2, which present low or zero brookite content, and for the samples C1 and C2, which present residual Na-titanate.

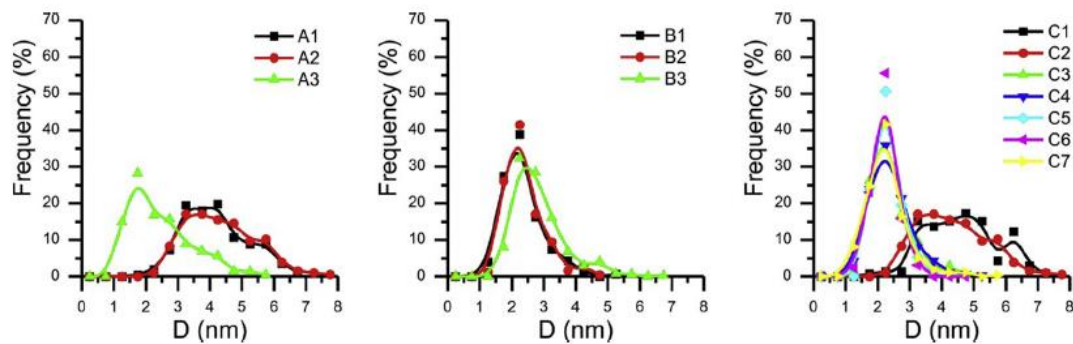


Fig.3.11 Size distribution of the Pt nanoparticles for the synthesised samples

The difference in the mean size of Pt nanoparticles in the samples can be associated with the formation of junctions between crystallites of different TiO_2 phase. This situation favours the electron-hole separation under irradiation conditions, increasing the number of nucleation sites on which Pt ions can be reduced and Pt nanoparticles can growth^(31–33).

3.8 Evaluation of the photoactivity of anatase/brookite nanorods: H_2 production by ethanol photodehydrogenation

The photocatalytic activity of the synthesized anatase/brookite nanocomposites were evaluated with respect to H_2 production by ethanol photodehydrogenation under solar light irradiation. More details of the experimental methodology can be found in the Chapter 2.

Commercial azeotropic ethanol/water solutions (containing ~96% by volume of ethanol) were used as feedstock to avoid changing in the composition during photocatalytic experiments due to selective evaporation in the inert gas flow. Preliminary experiments performed with the sample A1 revealed that the H_2 production using EtOH 96% is comparable with that observed using EtOH/ H_2O 50/50 mixture^(33–35), while it is significantly higher than the H_2 obtained using pure EtOH. This result indicates that only a little amount of water is necessary to promote the photocatalytic hydrogen production using EtOH as sacrificial agent. This is in agreement with results reported in the

literature about the relation of H₂ productivity with the EtOH/H₂O solutions⁽³⁶⁾. Blank experiments where performed without irradiation and not H₂ evolution was observed.

The on-line analysis of the volatile products revealed that H₂ is the major product in the gas stream, together with minor amounts of acetaldehyde and 1,1-diethoxyethane. Any other by products, such as CH₄, CO₂, CO or ethylene, was observed. The analysis of the liquid phases, collected at the end of the photocatalytic experiments, evidenced the presence of acetaldehyde and 1,1-diethoxyethane, accordingly to the results of the on-line analysis. Heaviest products, such as 2,3-butandiol, were not detected, in agreement with the fact that these products are formed when highly energetic UV photons are used for the irradiation⁽³⁷⁾.

The photocatalytic activity of the samples from the A- and B- series is represented in the Figure 3.12. Observing the H₂ evolution and taken in account the nature of the sample, the heating method for the hydrothermal conversion of Na-titanate precursor into TiO₂ titanate have an important role to drive the final photocatalytic performances. During the first 4-5h of the photocatalytic experiment, the H₂ production progressively increases; this is the time in which the Pt nanoparticles are photodeposited over the TiO₂ substrate.

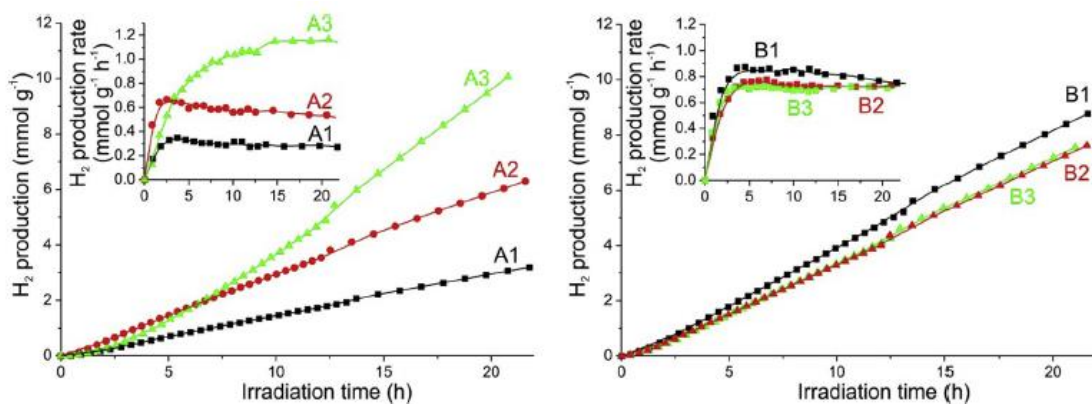


Fig.3.12 H₂ evolution during ethanol photodehydrogenation under simulated sunlight irradiation of the catalysts of the A- and B-series. The insets show the H₂ production rates.

After this activation process, the H₂ production rates remain constant without significant deactivation. The obtained results indicate that H₂ production rates increase for sample in the A-series as the Na-titanate/water ratio increases whereas it is only marginally influenced by the irradiation heating method (B-series).

The photocatalytic H₂ production of the C-series samples is reported in the Figure 3.13. As in the cases of A-series and B-series, during the photodeposition of the Pt nanoparticles (first 4-5h), the H₂ production rate increases. The photocatalytic H₂ production increases with the time of hydrothermal treatment up to 24h while for longer hydrothermal treatment time (more than 30h) not significant changes in the photoactivity were observed.

These results indicate that the complete transformation of the Na-titanate precursor into TiO₂ nanocomposite is fundamental to obtain high photocatalytic activity in the photodehydrogenation of the ethanol. Notably, a photocatalytic experiment with the bare Na-titanate precursor showed an H₂ production rates ~ 10 times lower than that obtained using the anatase/brookite composite (samples C4-C7).

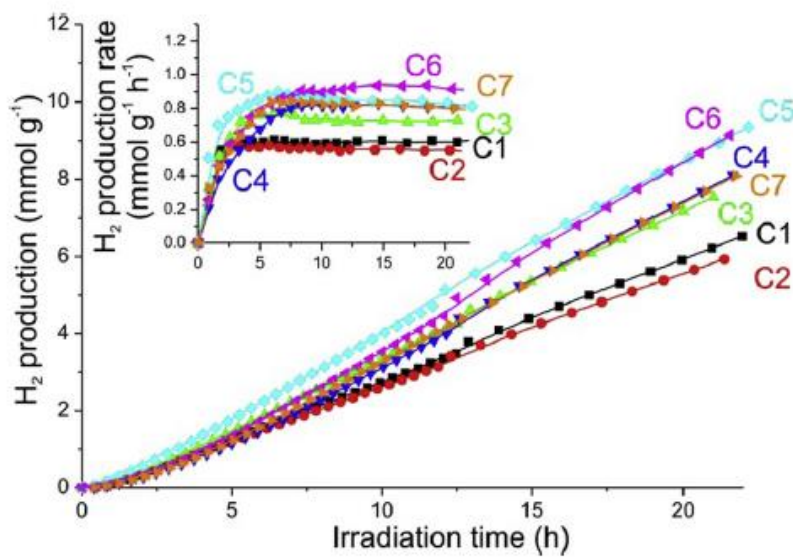
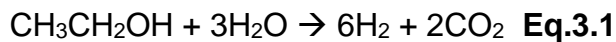


Fig.3.13 H₂ evolution during ethanol photodehydrogenation under simulated sunlight using the catalysts of the C-series. The inset shows the H₂ production rates.

To better understand these results, it is necessary to focus on the mechanism of the ethanol photoreforming (Figure 3.14). In a mixture of ethanol and water, the stoichiometric reaction for EtOH photoreforming is:



During our photocatalytic experiments, CO_2 evolution was not observed, indicating that the main process is the photocatalytic dehydrogenation of ethanol leading to acetaldehyde and H_2 . The oxidation of the acetaldehyde is highly unfavourable due to the low adsorption capability and the higher concentration of ethanol⁽³⁸⁾. The oxidation reaction of ethanol takes place on the surface of the TiO_2 . First OH^- groups and ethoxide are formed due to the dissociative adsorption on the TiO_2 of the ethanol. This process competes with H_2O adsorption. The photooxidation process involves the direct electron transfer from the ethoxide to photogenerated holes of TiO_2 meanwhile hydrogen of OH groups is reduced by photogenerated electrons trapped in the Pt nanoparticles. The produced acetaldehyde could be further oxidized to acetic acid if adsorbed on the surface or in solution by free OH^- radical. Otherwise acetaldehyde is accumulated in solution providing a less volatile compound. The high concentration of 1,1-diethoxyethane found in the liquid phase confirms that acetaldehyde react with ethanol⁽³⁸⁾.

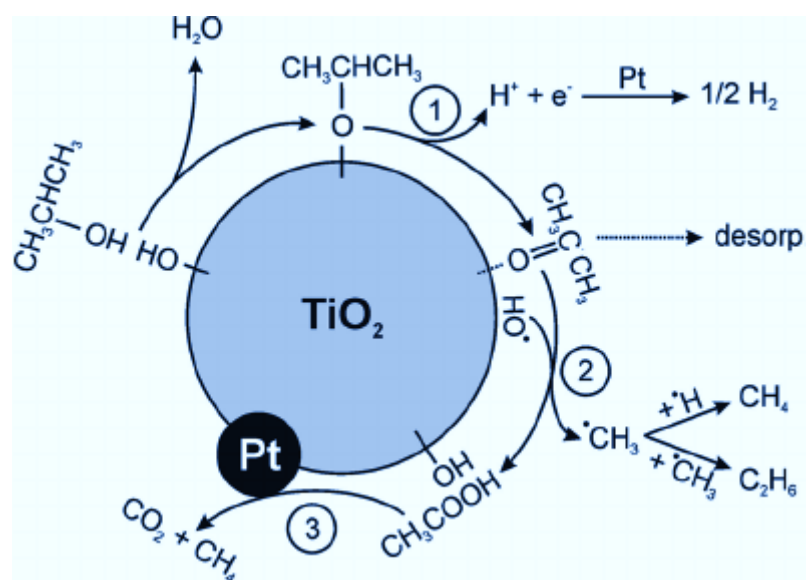


Fig.3.14 Schematic representation of the principal reaction of the ethanol photoreforming over the TiO_2 -Pt catalyst.

It well know that nanocomposites of different phases of TiO_2 are more active than the single phases both oxidation^(39,40) and in reduction^(18,35,41–43) process. This is due to a better electron-hole separation that avoids the recombination because the formation of heterojunctions between the crystallites of the different phases. Kandiel et al.⁽⁴⁴⁾ reported that flat band potential and quasi-Fermi level of brookite nanorods and of anatase/brookite nanocomposites are shifted to a more negative potential with respect to pure anatase. This reflects in a higher driving force for proton reduction in brookite containing materials, favouring interfacial electron transfer while the resulting energy barrier would suppress back electron transfer⁽⁴⁴⁾. Figure 3.15 clearly show that the samples made by anatase/brookite nanocomposites are more active than the sample containing only anatase. The results from characterization clearly evidenced that the heating method mainly influence the amount of brookite and, accordingly, the activity of the materials. In contrast, there is a not relation between the amount of brookite and the activity of the samples prepared via irradiation.

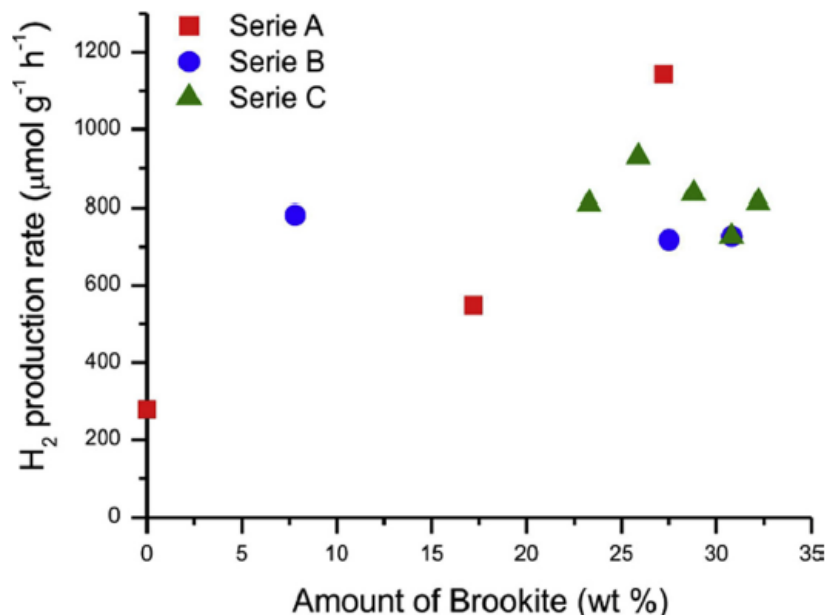


Fig.3.15 Stationary H_2 production rates as a function of brookite content in the studied materials. Samples C1 and C2 are omitted since the brookite content are warped by the amount of unconverted Na-titanate precursor, hardly detected by XRD.

The photocatalytic activity of the samples cannot be explained only considering the structural properties of the prepared materials but presents a complex dependence on morphological characteristics (surface area and exposed facets). The most important differences observed between the A- and B-series could be ascribed to potential different interaction/contact between the anatase and brookite crystallites, as a result of the different heating method adopted during the synthesis.

In order to understand better the influences of the morphological parameters of the present anatase/brookite nanocomposites, their photocatalytic activities were compared with that of a well-known TiO_2 material. For this purpose, multiphasic TiO_2 was synthesized by sol-gel method (hydrolysis of $\text{Ti}(i\text{-PrO})_4$ in a $\text{H}_2\text{O}/\text{EtOH}$ solution using HNO_3 as catalyst⁽³⁵⁾). After calcination at 420°C, the TiO_2 -SG material was composed of 64% anatase, 28% brookite and 8% rutile and possesses a surface area of 68 m²/g. After photodeposition of 0.2 wt. % Pt, Pt nanoparticles of about 2.5 nm were obtained as confirmed by means HAADF-STEM.

Normalizing the photocatalytic activity with respect to the mass of the catalyst, the performance of the TiO_2 -SG material is significantly higher than those observed for the anatase/brookite nanocomposites prepared in this study. Nevertheless, normalizing the performances on the basis of the surface area, the prepared material shows interesting/superior performances, as presented in Figure 3.16. This result suggests that the hydrothermal treatments used for the preparation of the samples allow the crystals to grow exposing crystallographic facets that are more actives than the facets exposed by the TiO_2 prepared via sol-gel. Since this material is synthesized in the absence of template agents and is subsequently calcined, it is reasonable to assume that it exposes the more thermodynamically stable facets instead of the more actives.

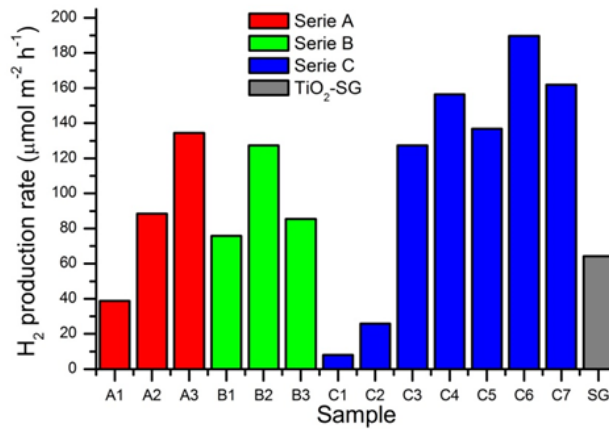


Fig.3.16 H_2 production during EtOH photodehydrogenation of a suspension of the prepared samples and the TiO_2 prepared via sol–gel (TiO_2 -SG) normalized per surface area.

3.9 Conclusions

In the present study, highly crystalline anatase/brookite nanocomposites were successfully synthesized by hydrothermal treatment of Na-titanate precursor. The phase composition can be tuned varying the Na-titanate/water ratio and the time for hydrothermal treatment, as confirmed with XRD and Raman analysis. The sizes of the photodeposited Pt nanoparticles, employed as co-catalyst, are influenced by the anatase/brookite ratio of the support. Photocatalytic activities of the as-synthesized anatase/brookite nanocomposites were evaluated in the H₂ production via photodehydrogenation of ethanol under simulated solar irradiation. High H₂ production was observed for the samples with multiphasic anatase/brookite support and small Pt nanoparticles. This is likely due to the efficient electrons transfer from the conduction band of the brookite to the conduction band of the anatase resulting in effective-hole separation. Furthermore, the photoactivity of these materials showed a higher H₂ production than reference samples prepared by conventional sol-gel method when normalized with respect to the surface area of the samples. This indicates that the present anatase/brookite nanocomposites expose the more reactive facets.

References

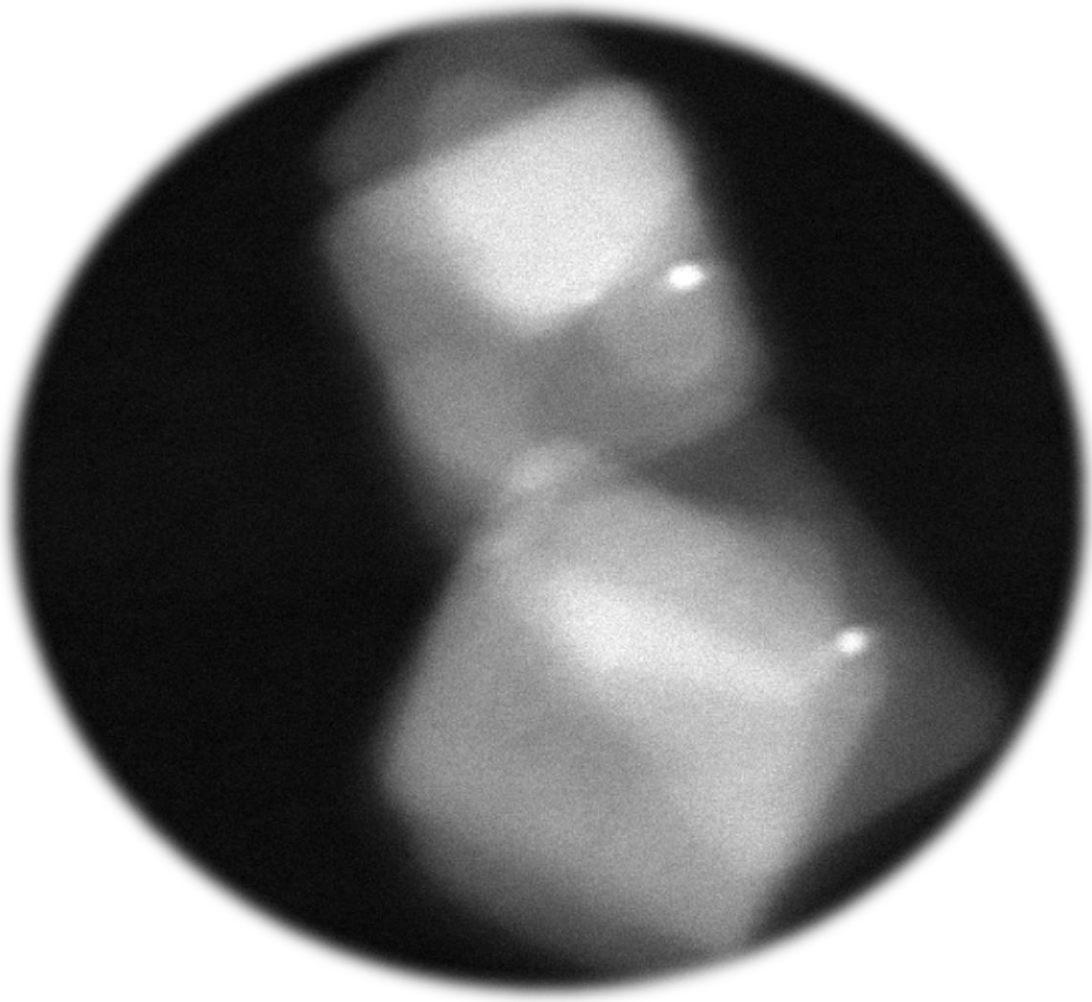
1. Chen P, Gu L, Xue X, Li M, Cao X. Engineering the growth of TiO₂ nanotube arrays on flexible carbon fibre sheets. *Chem Commun (Camb)*. 2010 Aug 28;46(32):5906–8.
2. Naldoni A, Bianchi CL, Pirola C, Suslick KS. Porous TiO₂ microspheres with tunable properties for photocatalytic air purification. *Ultrason Sonochem*. 2013 Jan;20(1):445–51.
3. Ozawa T, Iwasaki M, Tada H, Akita T, Tanaka K, Ito S. Low-temperature synthesis of anatase-brookite composite nanocrystals: the junction effect on photocatalytic activity. *J Colloid Interface Sci*. 2005 Jan 15;281(2):510–3.
4. Etacheri V, Michlits G, Seery MK, Hinder SJ, Pillai SC. A highly efficient TiO_{(2-x)C(x)} nano-heterojunction photocatalyst for visible light induced antibacterial applications. *ACS Appl Mater Interfaces*. 2013 Mar 13;5(5):1663–72.
5. Xu H, Zhang L. Controllable One-Pot Synthesis and Enhanced Photocatalytic Activity of Mixed-Phase TiO₂ Nanocrystals with Tunable Brookite/Rutile Ratios. *J Phys Chem C*. 2009 Feb 5;113(5):1785–90.
6. Gordon TR, Cagnello M, Paik T, Mangolini F, Weber RT, Fornasiero P, et al. Nonaqueous synthesis of TiO₂ nanocrystals using TiF₄ to engineer morphology, oxygen vacancy concentration, and photocatalytic activity. *J Am Chem Soc*. 2012;134(15):6751–61.
7. Cagnello M, Montini T, Smolin SY, Priebe JB, Delgado JJ. Engineering titania nanostructure to tune and improve its photocatalytic activity. 2016;
8. Testino A, Bellobono IR, Buscaglia V, Canevali C, D'Arienzo M, Polizzi S, et al. Optimizing the photocatalytic properties of hydrothermal TiO₂ by the control of phase composition and particle morphology. a systematic approach. *J Am Chem Soc*. 2007 Mar 28;129(12):3564–75.

9. Philip Colombo D, Roussel KA, Saeh J, Skinner DE, Cavalieri JJ, Bowman RM. Femtosecond study of the intensity dependence of electron-hole dynamics in TiO₂ nanoclusters. *Chem Phys Lett.* 1995 Jan;232(3):207–14.
10. Kikuchi H, Kitano M, Takeuchi M, Matsuoka M, Anpo M, Kamat P V. Extending the photoresponse of TiO₂ to the visible light region: photoelectrochemical behavior of TiO₂ thin films prepared by the radio frequency magnetron sputtering deposition method. *J Phys Chem B.* American Chemical Society; 2006 Mar 23;110(11):5537–41.
11. Yamada Y, Kanemitsu Y. Determination of electron and hole lifetimes of rutile and anatase TiO₂ single crystals. *Appl Phys Lett.* 2012;101(13):133907.
12. Kawahara T, Konishi Y, Tada H, Tohge N, Nishii J, Ito S. A patterned TiO₍₂₎(anatase)/TiO₍₂₎(rutile) bilayer-type photocatalyst: effect of the anatase/rutile junction on the photocatalytic activity. *Angew Chem Int Ed Engl.* 2002 Aug 2;41(15):2811–3.
13. Masumoto Y, Takagi H, Umino H, Suzumura E. Fast electron transfer from PbSe quantum dots to TiO₂. *Appl Phys Lett.* 2012;100(25):252106.
14. Manga KK, Zhou Y, Yan Y, Loh KP. Multilayer Hybrid Films Consisting of Alternating Graphene and Titania Nanosheets with Ultrafast Electron Transfer and Photoconversion Properties. *Adv Funct Mater.* 2009 Nov 23;19(22):3638–43.
15. Long R, English NJ, Prezhdo O V. Photo-induced charge separation across the graphene-TiO₂ interface is faster than energy losses: a time-domain ab initio analysis. *J Am Chem Soc.* 2012 Aug 29;134(34):14238–48.
16. Li J, Xu D. Tetragonal faceted-nanorods of anatase TiO₂ single crystals with a large percentage of active {100} facets. *Chem Commun (Camb).* 2010 Apr 7;46(13):2301–3.
17. Zhao B, Lin L, He D. Phase and morphological transitions of titania/titanate nanostructures from an acid to an alkali hydrothermal environment. *J Mater Chem A.* 2013;1(5):1659–68.

18. Liu Y, Wang Z, Wang W, Huang W. Engineering highly active TiO₂ photocatalysts via the surface-phase junction strategy employing a titanate nanotube precursor. *J Catal.* 2014 Feb;310:16–23.
19. Van Santen RA. The Ostwald step rule. *J Phys Chem.* 1984;88(24):5768–9.
20. Zhao X, Jin W, Cai J, Ye J, Li Z, Ma Y, et al. Shape- and size-controlled synthesis of uniform anatase TiO₂ nanocuboids enclosed by active {100} and {001} facets. *Adv Funct Mater.* 2011;21(18):3554–63.
21. Gordon TR, Cagnello M, Paik T, Mangolini F, Weber RT, Fornasiero P, et al. Nonaqueous synthesis of TiO₂ nanocrystals using TiF₄ to engineer morphology, oxygen vacancy concentration, and photocatalytic activity. *J Am Chem Soc.* 2012 Apr 18;134(15):6751–61.
22. Ohno T, Sarukawa K, Matsumura M. Crystal faces of rutile and anatase TiO₂ particles and their roles in photocatalytic reactions. *New J Chem.* 2002 Aug 22;26(9):1167–70.
23. Zhao H, Liu L, Andino JM, Li Y. Bicrystalline TiO₂ with controllable anatase–brookite phase content for enhanced CO₂ photoreduction to fuels. *J Mater Chem A.* 2013;1(28):8209.
24. Liu B, Aydil ES. Growth of oriented single-crystalline rutile TiO₍₂₎ nanorods on transparent conducting substrates for dye-sensitized solar cells. *J Am Chem Soc.* 2009 Mar 25;131(11):3985–90.
25. Xiong C, Deng X, Li J. Preparation and photodegradation activity of high aspect ratio rutile TiO₂ single crystal nanorods. *Appl Catal B Environ.* 2010 Feb;94(3–4):234–40.
26. Ma X, Dai Y, Guo M, Huang B. Relative Photooxidation and Photoreduction Activities of the {100}, {101}, and {001} Surfaces of Anatase TiO₂. *Langmuir.* 2013 Nov 5;29(44):13647–54.
27. Mao Y, Wong SS. Size- and shape-dependent transformation of nanosized titanate into analogous anatase titania nanostructures. *J Am Chem Soc.* 2006 Jun 28;128(25):8217–26.

28. Sun X, Li Y. Synthesis and characterization of ion-exchangeable titanate nanotubes. *Chemistry*. 2003 May 23;9(10):2229–38.
29. Bavykin DV, Friedrich JM, Walsh FC. Protonated Titanates and TiO₂ Nanostructured Materials: Synthesis, Properties, and Applications. *Adv Mater*. 2006 Nov 3;18(21):2807–24.
30. Ohno T, Higo T, Murakami N, Saito H, Zhang Q, Yang Y, et al. Photocatalytic reduction of CO₂ over exposed-crystal-face-controlled TiO₂ nanorod having a brookite phase with co-catalyst loading. *Appl Catal B Environ*. 2014 Jun;152–153(1):309–16.
31. Sun B, Vorontsov A V., Smirniotis PG. Role of platinum deposited on TiO₂ in phenol photocatalytic oxidation. 2003 Apr 15;19(8):3151–6.
32. Hidalgo MC, Maicu M, Navío JA, Colón G. Photocatalytic properties of surface modified platinised TiO₂: Effects of particle size and structural composition. *Catal Today*. 2007;129(1):43–9.
33. Gombac V, Sordelli L, Montini T, Delgado JJ, Adamski A, Adami G, et al. CuO x -TiO₂ Photocatalysts for H₂ Production from Ethanol and Glycerol Solutions †. 2010;3916–25.
34. Gallo A, Montini T, Marelli M, Minguzzi A, Gombac V, Psaro R, et al. H₂ Production by Renewables Photoreforming on Pt-Au/TiO₂ Catalysts Activated by Reduction. *ChemSusChem*. 2012 Sep 13;5(9):1800–11.
35. Montini T, Gombac V, Sordelli L, Delgado JJ, Chen X, Adami G, et al. Nanostructured Cu/TiO₂ Photocatalysts for H₂ Production from Ethanol and Glycerol Aqueous Solutions. *ChemCatChem*. 2011 Mar 7;3(3):574–7.
36. Stratakis N, Bekiaris V, Kondarides DI, Lianos P. Hydrogen production by photocatalytic alcohol reforming employing highly efficient nanocrystalline titania films. *Appl Catal B Environ*. 2007 Nov;77(1–2):184–9.
37. Gasparotto A, Barreca D, Bekermann D, Devi A, Fischer RA, Fornasiero P, et al. F-Doped Co₃O₄ Photocatalysts for Sustainable H₂ Generation from Water/Ethanol. *J Am Chem Soc*. 2011 Dec 7;133(48):19362–5.

38. Ampelli C, Passalacqua R, Genovese C, Perathoner S, Centi G, Montini T, et al. Solar energy and biowaste conversion into H₂ on CuO x/TiO₂ nanocomposites. In Italian Association of Chemical Engineering - AIDIC; 2013. p. 583–8.
39. Emilio CA, Litter MI, Kunst M, Bouchard M, Colbeau-Justin C. Phenol Photodegradation on Platinized-TiO₂ Photocatalysts Related to Charge-Carrier Dynamics. *Langmuir*. 2006 Apr;22(8):3606–13.
40. Carneiro JT, Savenije TJ, Moulijn J a., Mul G. How phase composition influences optoelectronic and photocatalytic properties of TiO₂. *J Phys Chem C*. 2011;115(5):2211–7.
41. Lin C-H, Lee C-H, Chao J-H, Kuo C-Y, Cheng Y-C, Huang W-N, et al. Photocatalytic Generation of H₂ Gas from Neat Ethanol over Pt/TiO₂ Nanotube Catalysts. *Catal Letters*. 2004 Oct;98(1):61–6.
42. Kuo H-L, Kuo C-Y, Liu C-H, Chao J-H, Lin C-H. A highly active bicrystalline photocatalyst consisting of TiO₂ (B) nanotube and anatase particle for producing H₂ gas from neat ethanol. *Catal Letters*. 2007 Jan 13;113(1–2):7–12.
43. Lin C-H, Chao J-H, Liu C-H, Chang J-C, Wang F-C. Effect of Calcination Temperature on the Structure of a Pt/TiO₂ (B) Nanofiber and Its Photocatalytic Activity in Generating H₂. *Langmuir*. 2008 Sep 2;24(17):9907–15.
44. Ismail A a., Kandiel T a., Bahnemann DW. Novel (and better?) titania-based photocatalysts: Brookite nanorods and mesoporous structures. *J Photochem Photobiol A Chem*. Elsevier B.V.; 2010 Dec;216(2–3):183–93.



**TiO₂ Nanosheets for
photocatalytic H₂
production**

4. - TiO₂ nanosheets for photocatalytic production of H₂

This chapter concerns on the photocatalytic activity of the TiO₂ nanosheets in the H₂ production by ethanol dehydrogenation under simulated solar light. The effect of different parameters, such as metal doping and presence of fluorine, have been evaluated with respect to structural, optical, morphological and functional properties of the prepared materials.

TiO₂ nanosheets samples were doped with first series transition metals in order to discover how they influenced the optical properties and the photocatalytic activity. Special attention was paid to the presence of fluorine ions on the surface of the photocatalysis and their influence on H₂ production during the photocatalytic experiments. TiO₂ nanosheets were characterized a plethora of experimental techniques to correlate the observed photocatalytic activities with their bulk and surface composition, morphology, structure, textural properties and optical properties.

4.1 Synthesis of TiO₂ nanosheets

Metal-doped TiO₂ anatase single crystal nanosheets were synthesized by adapting the procedure reported by Zhang et al^(1,2). First, 60 mL of 2-propanol (2-PrOH) and 18 mL of tetrabutyl titanate Ti(C₄H₉O)₄ were mixed into a 150 mL Teflon-lined autoclave. Then, the dopant metal was introduced by adding an adequate amount of the correspondent metal nitrate. Finally, 2.16 mL of HF (48 wt%) as a capping agent were added dropwise under stirring using a micropipette. The nominal molar ratio of HF to Ti(C₄H₉O)₄ was kept constant (2:1). After mixing the solution for 30min, the Teflon-lined autoclave was placed in the oven for a solvothermal treatment at 180°C for 24h. After the solvothermal reaction, the products were carefully collected and washed three times with a mixture of H₂O miliQ and ethanol (EtOH) (50:50) in a centrifuge at 4500 rpm and then dried overnight in an oven at 70°C.

Two series of samples were prepared changing the metal (M):Ti molar ratio in the solution subjected to solvothermal treatment changing the amount of the metal nitrate introduced in the synthesis procedure, with the aim to introduce different amount of the dopant metals into the anatase crystal structure. In particular, molar M:Ti ratios were adjusted in order to obtain a nominal metal loading of 0.75 wt% and 1.5 wt%, calculated as:

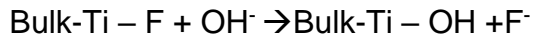
$$M \text{ wt\%} = \frac{m_M}{m_M + m_{TiO_2}} \times 100 \quad \text{Eq.4.1}$$

where M wt% in the metal content expressed as weight percent, m_M in the mass of the metal M and m_{TiO₂} is the mass of TiO₂ matrix.

The two series of samples are denoted as **0.75M-TiO₂** and **1.5M-TiO₂**, indicating respectively the samples with the desired metal content of 0.75 wt% and 1.5 wt%. As comparison material, an un-doped TiO₂ sample has been prepared using only the Ti precursor in the solvothermal reaction.

In order to investigate the effect of surface fluorination on photoactivity, the TiO₂ nanosheets were treated with diluted 0.01M NaOH solution to desorb fluoride ions form the surface⁽³⁾. The TiO₂ powder (0.5g) was placed in a plastic beaker, NaOH solution was added (50mL for 0.5g TiO₂) and magnetically

stirred in the dark for 12 hours. Then, the samples were washed with a dilute HCl solution (25mL; twice) by filtering in a vacuum to eliminate Na⁺ ions and with miliQ water until no Cl⁻ ions were detected in the mother liquor (test with AgNO₃). The treatment has been repeated 4 times, in order to ensure complete removal of fluoride ions adsorbed on the surface of the materials. Finally, the samples were dried at 60°C overnight. The F⁻ ions adsorbed onto the surface of the TiO₂ samples were removed via the following ligand exchange reaction:



The samples prepared by removing surface fluoride by the NaOH treatment will be labelled as **0.75M-TiO₂-NaOH** and **1.5M-TiO₂-NaOH**.

4.2 Morphological characterization: transmission electron microscopy

The morphology and crystal structure of the resulting TiO₂ products were investigated using electron microscopy (Figure 4.1). The synthesized TiO₂ materials comprise of well-defined sheet-shaped particles with a rectangular outline. From the HAADF observations (Figure 4.2), it can be seen that the synthesized TiO₂ nanosheets have a side length of approximately 35 nm and an approximate thickness of 5 nm.

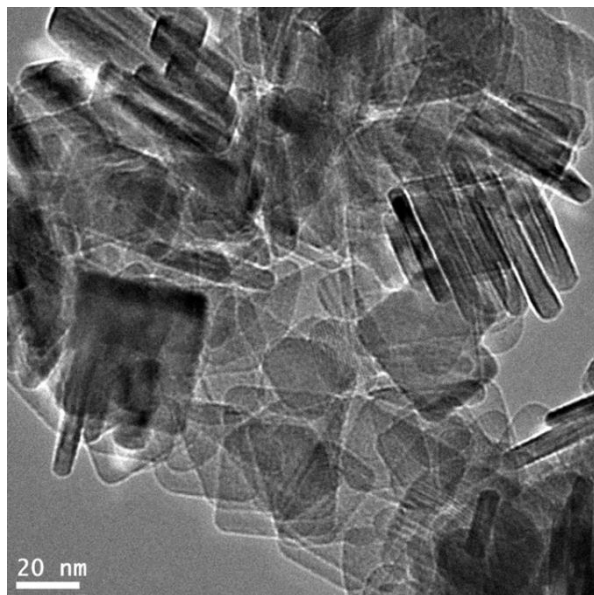


Fig. 4.1 TEM image of the TiO₂ nanosheets. The product consists of well-defined sheet-shaped structures with rectangular outlines.

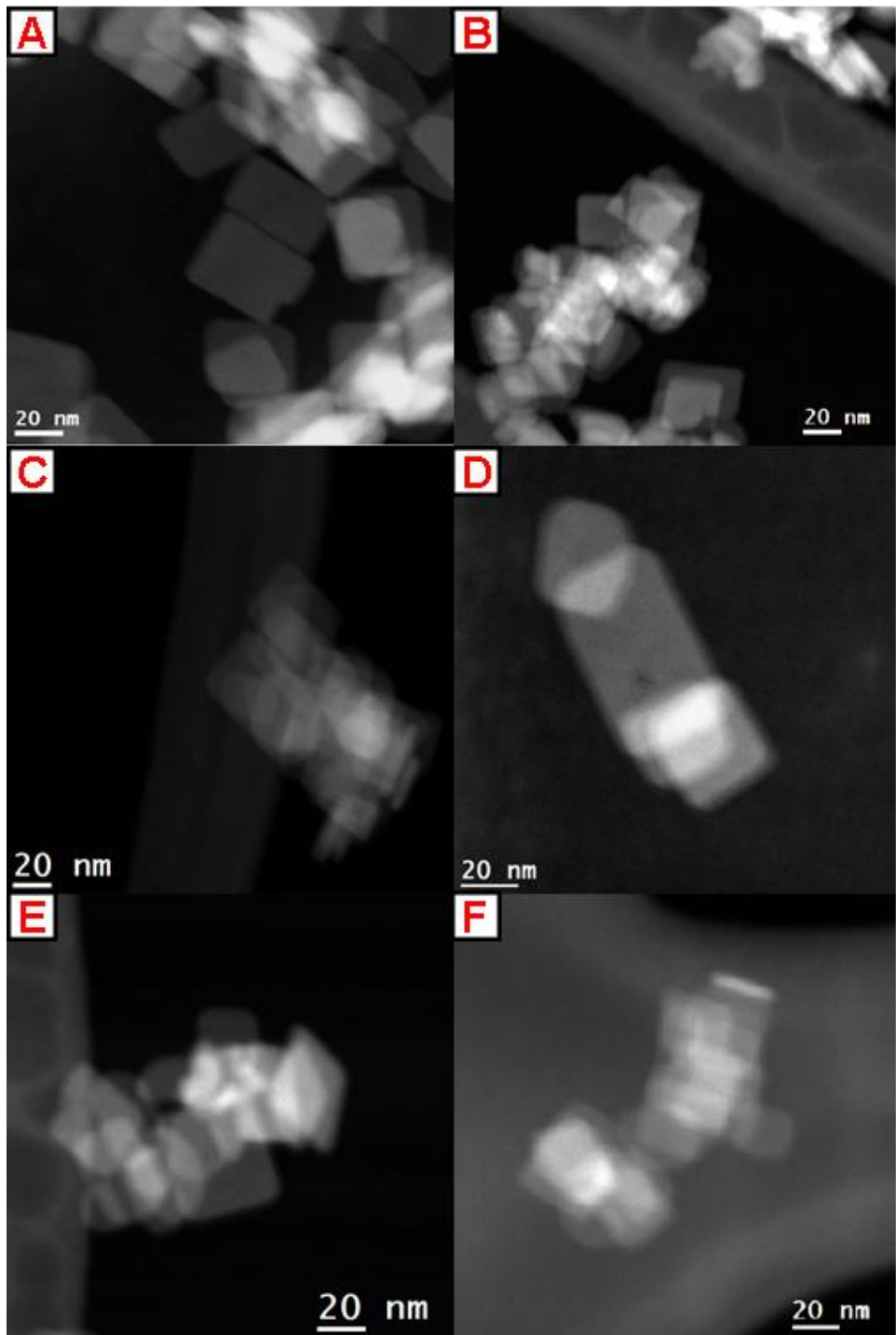


Fig. 4.2. Representative HAADF-STEM images for the M-TiO₂ samples: A) 0.75Mn-TiO₂ B) 1.5Mn-TiO₂ C) 0.75Ni-TiO₂ D) 1.5Ni-TiO₂ E) 0.75Co-TiO₂ F) 1.5Co-TiO₂

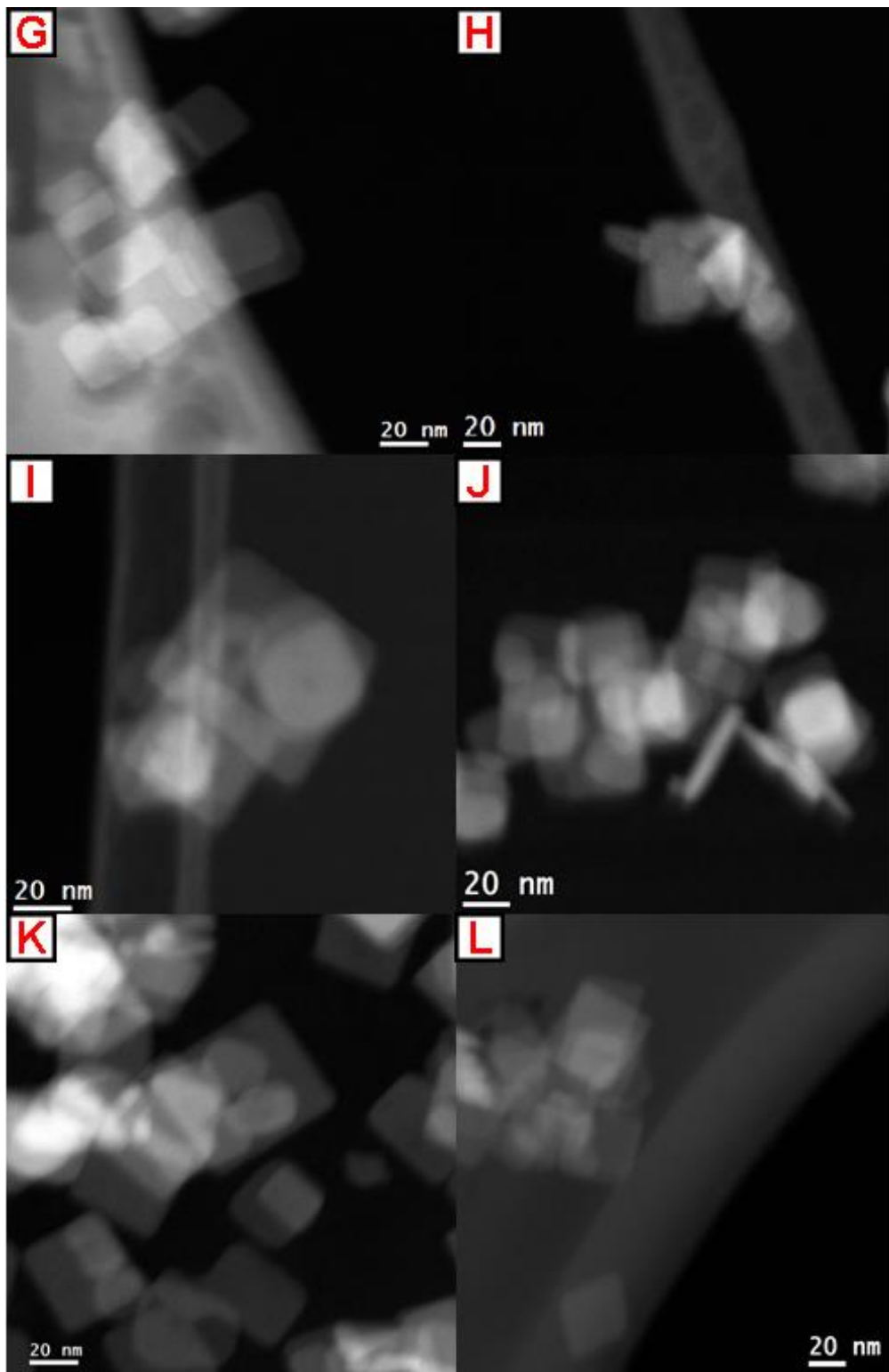


Fig. 4.2. (Continuation) Representative HAADF-STEM images for the M-TiO₂ samples: G) 0.75Cu-TiO₂ H) 1.5Cu-TiO₂ I) 0.75Fe-TiO₂ J) 1.5Fe-TiO₂ K) undoped TiO₂ L) undoped TiO₂

The identification of the crystallographic phase of the TiO₂ nanosheets particles was attempted comparing the digital diffraction pattern (DDP) obtained from the HR-TEM images with the theoretical ones simulated for various different orientations of TiO₂ crystal structures. Figure 4.3 shows a representative example of the studied sample. The upper-right corner contains a zoom of the picture, where the distance between the planes of the TiO₂ nanosheets was measured: the spacing of 0.19 nm corresponds to the (200) planes of anatase TiO₂. The lower left-hand corner shows the DDP (digital diffraction pattern) oriented along direction (111). The experimental DDP obtained from the HR-TEM image agrees well with the theoretical DDP calculated using the Eje-Z® software (Figure 4.3, right).

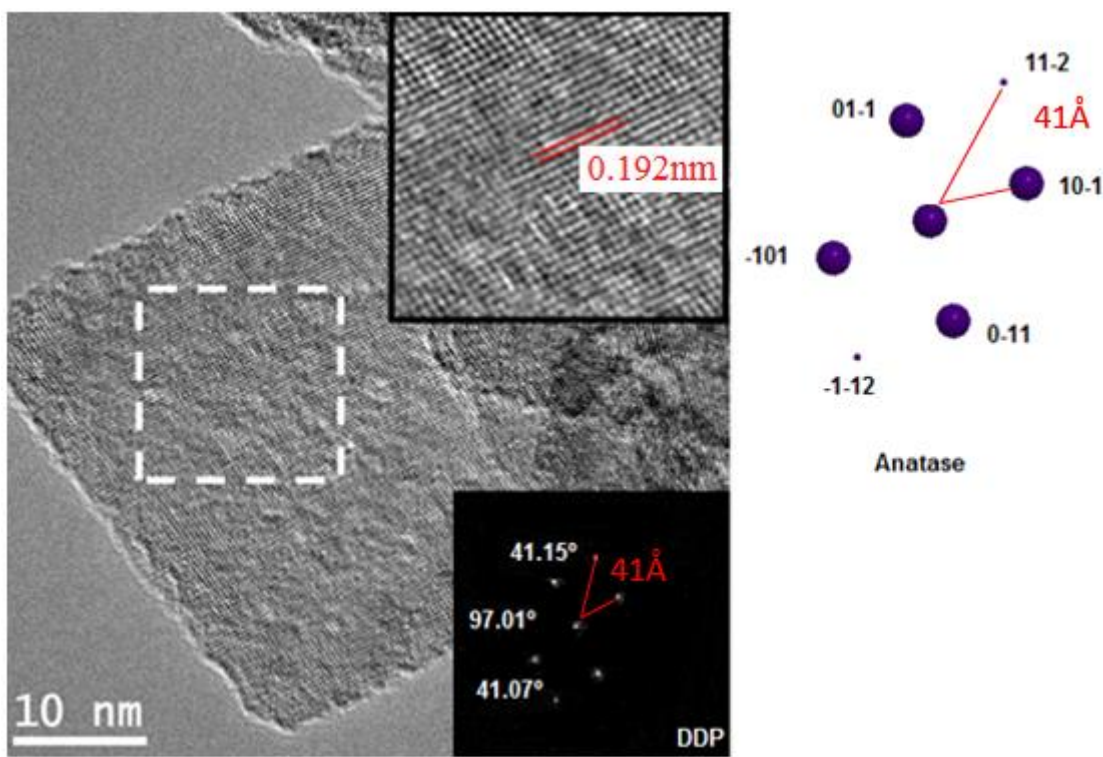


Fig. 4.3. Representative HR-TEM image of the undoped TiO₂ nanosheets, together with the correspondent Digital Diffraction Patten (DDP) and the theoretical DDP calculated along the <111> orientation of TiO₂ phase.

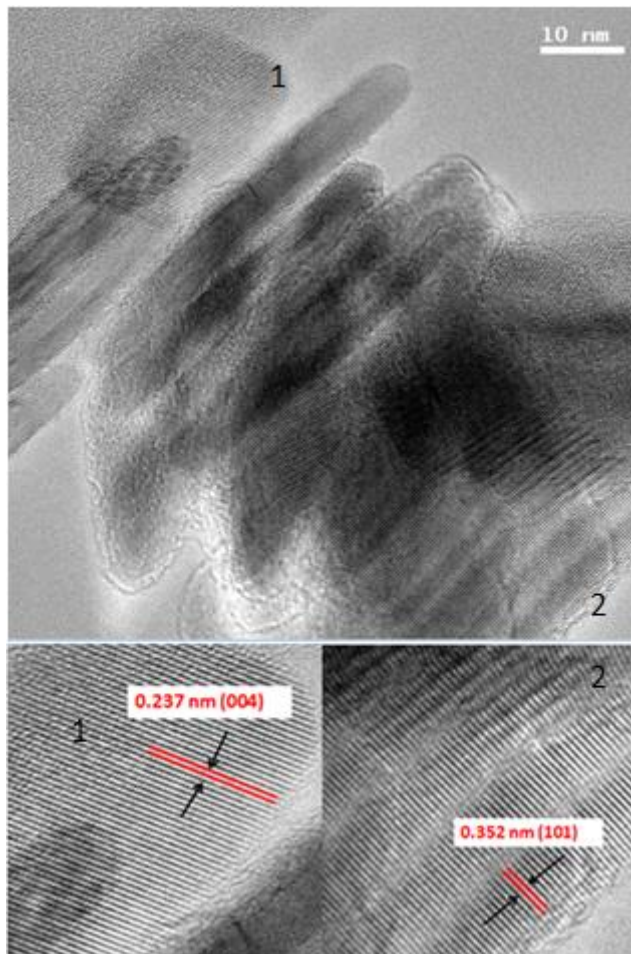


Fig. 4.4 HRTEM image in which is shown two labelled areas: **1**) interplanar distance of 0.237 nm that correspond to (200) plane of anatase TiO₂ and **2**) interplanar distance of (0.352 nm) that correspond to (004) plane of anatase TiO₂.

The orientation of the anatase TiO₂ nanocrystals was identified considering the interplanar spacing measured from HR-TEM images (Figures 4.3 and Figure 4.4). The interplanar spacing of 0.192 nm (Figure 4.3) corresponds to (002) family of planes while the interplanar spacing of 0.237 nm (Figure 4.4) corresponds to (004) family of planes of anatase TiO₂. This indicates that the large flat surface exposed by the anatase TiO₂ single crystal corresponds to the {001} facet. The lattice fringes with spacing of 0.352 nm are well in agreement with the (101) family of planes of anatase TiO₂ single crystal. As a consequence, the facets exposed on the lateral surfaces of the TiO₂ nanocrystal are the {101} surfaces ⁽⁴⁾

It is well known that a high percentage of exposed {001} facets contributes to excellent TiO₂ activity, as it has been reported that the {001} surface of the anatase TiO₂ is more reactive than other stable surfaces⁽⁵⁻⁷⁾, such as {101}.

The percentage of exposed {001} facets depends on several factors, including the pH of the solution, the concentration of F⁻ ions during the synthesis, the amount of dopant and the degree of truncation of the TiO₂ nanosheets⁽⁸⁾. The typical crystal shape found in nature for anatase crystal is a truncated octahedral bipyramid (TOB), exposing large {101} facets and a small fraction of {001} facets⁽⁹⁾.

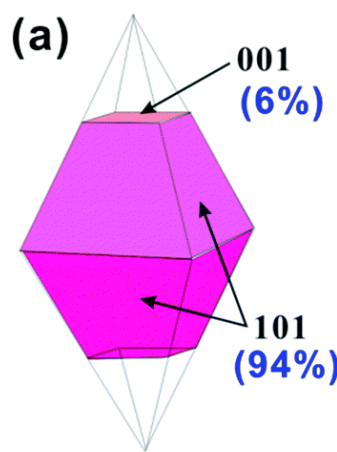


Fig.4.5. Wulff construction of anatase crystals, resulting in the formation of a truncated octahedral bipyramid (TOB).

Under solvothermal synthesis conditions, the growth process can be controlled modulating the percentage of {001} exposed facets by selecting the Ti precursors, the reaction solvents, the capping agents and the reaction conditions (temperature, time and pressure). In particular, nanocrystals exposing a large fraction of {001} facets can be produced by addition of F ions into the reaction medium. This is because adsorption of F on the surface of TiO₂ anatase strongly affects the surface energy, reversing their relative stability order and changing their expected shape^(1,2,10).

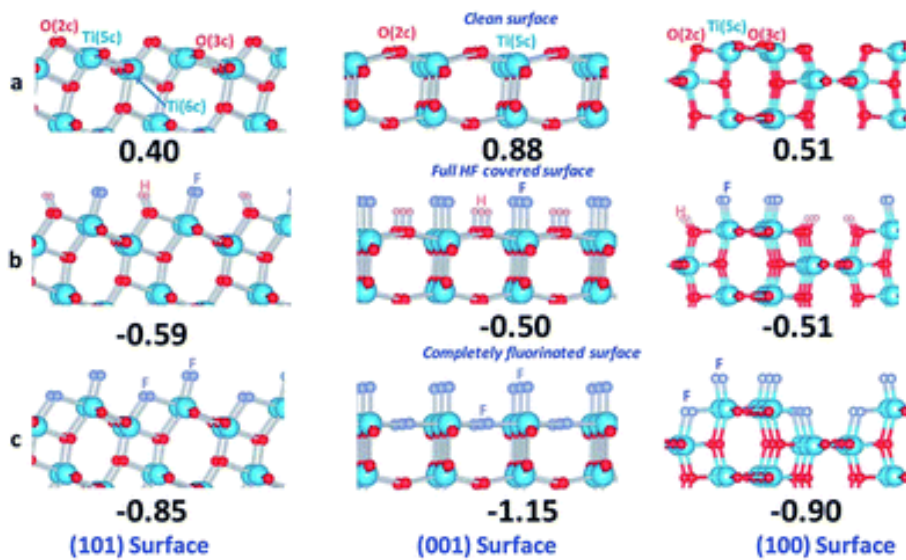


Fig. 4.6: DFT calculated surface energies (the unit is J m⁻²) and structures for different stages of HF interaction with single crystal anatase TiO₂ (101) (left) (001) (middle) and (100) (right) surfaces. (a) Clean surfaces; (b) full HF-covered surfaces; (c) complete fluorinated surfaces. All structures are optimized structures⁽¹¹⁾.

DFT calculations showed that {101} facets possess the lower surface energy in the absence of any adsorbed species, justifying the large fraction of this facet observed in equilibrium habit of anatase (Figure 4.6). On the other hand, the addition of HF or fluoride ions resulted in the adsorption of F on the surface, with a strong stabilization of {001} surface⁽¹¹⁾. By controlling of the amount of HF in the reaction medium during the synthesis, it is possible to modulate the percentage of surface made by exposed {001} facets in the TiO₂ nanocrystals. Fluoride ions adsorbed on {001} facets do not allow the nanocrystal to grow by deposition of Ti precursor on it. Consequently, crystal growth takes place only by deposition of Ti precursors on the {101} facets, growing the nanocrystal along the [100] and [010] directions. The product of this process is a flat nanocrystal with extended {001} facets and a small thickness along the [001] direction, presenting the shape of a nanosheet. With respect to the Wulff construction of the anatase crystals (Figure 4.5), the obtained nanosheets correspond to the central part of the truncated octahedral bipyramid.

The HAADF-STEM images were used to measure the side length and thickness of the synthesized TiO₂ nanosheets. The length and thickness distributions for the different samples are presented in Figure 4.7. Table 4.1 summarizes the averages sizes of the TiO₂ nanosheets measured from HAADF-STEM images (Figure 4.2).

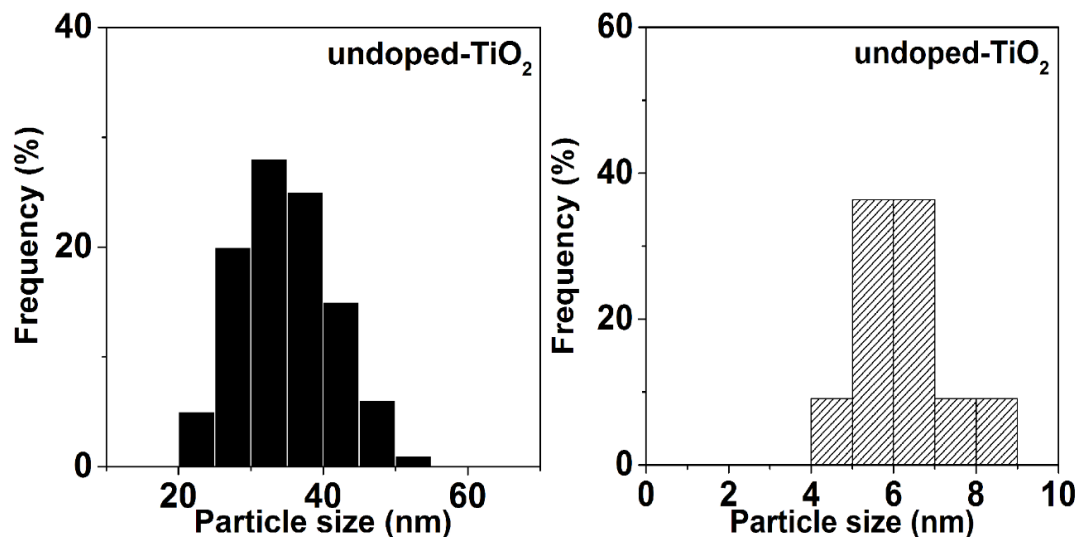


Fig. 4.7: Length (solid infill) and thickness (dashed infill) distribution for all the samples studied in the present work.

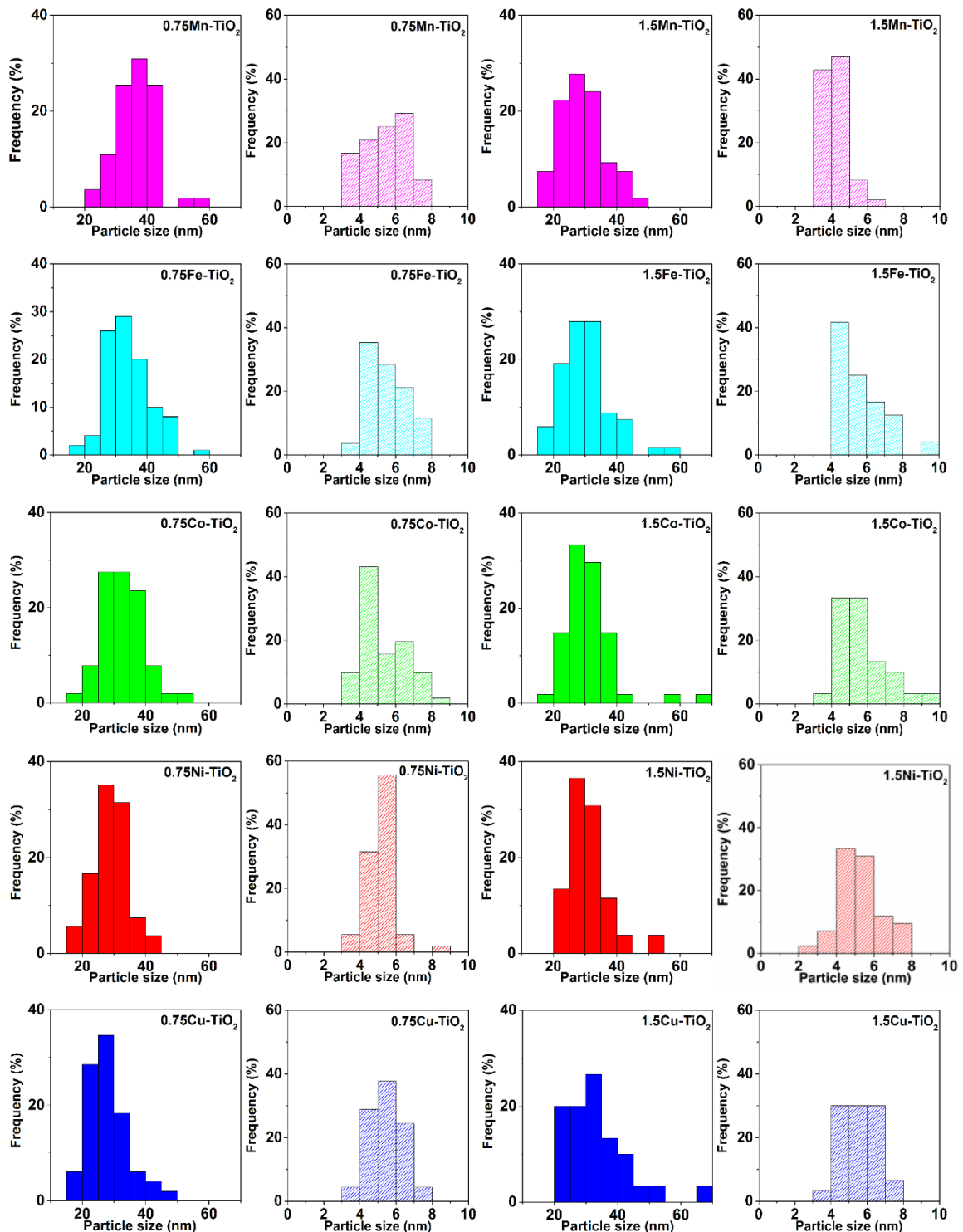


Fig. 4.7(continuation): Length (solid infill) and thickness (dashed infill) distribution for all the samples studied in the present work.

The percentage of surface represented by the (001) facets was calculated following Equation 4.1. According to the HR-TEM image, the top and bottom facets of the (001)-TiO₂ nanosheets are their (001) planes.

$$\%(\text{001}) = \frac{\text{length}^2}{2*\text{length}^2 + 4*\text{length}*\text{thickness}} \quad \text{Eq. 4.2}$$

Table 4.1. Calculation of the percentage of active facets on the TiO₂ nanosheets.

Sample	Average length (nm)	Average thickness(nm)	%(\text{001})	nº of particles counted
undoped	35	6	73%	150
0.75Mn-TiO₂	37	5	77%	100
1.5Mn-TiO₂	29	4	78%	100
0.75Co-TiO₂	33	5	83%	100
1.5Co-TiO₂	31	6	73%	100
0.75Ni-TiO₂	29	5	73%	100
1.5Ni-TiO₂	31	5	74%	100
0.75Cu-TiO₂	28	5	72%	100
1.5Cu-TiO₂	33	6	74%	100
0.75Fe-TiO₂	33	5	75%	100
1.5Fe-TiO₂	30	6	72%	100

The obtained results show that the average size of the nanosheets are marginally affected by the nature and the concentration of the dopant metals, resulting in comparable values of %(\text{001}). This result indicates that the size and shape of M-doped TiO₂ nanosheets is essentially controlled by HF added as capping agent, with a marginal influence of the addition of Mⁿ⁺ and nitrates ions.

TEM investigations were extended also on the samples subjected to NaOH treatment to remove surface adsorbed F⁻ ions (**M-TiO₂-NaOH** samples). After NaOH washing, no significant differences have been observed with respect to the pristine materials. This result confirms that the treatment at high

pH value, required to desorb F⁻ from the surface of TiO₂, does not affect the morphology and the size on anatase nanosheets investigated.

4.3 Phase composition and crystallite size: powder XRD

Powder XRD was used to identify the phase composition of the synthesized samples. Figure 4.8 shows the XRD patterns of the different pristine M-doped materials while Figure 4.9 presents the data acquired for the samples after removal of surface F⁻ ions.

All the patterns present well-developed reflections, indicating the formation of well crystallized materials. For all the samples analysed, the reflections match well with the typical XRD pattern of the anatase phase. The reflections of possible impurities, such as dopant metal oxides, other TiO₂ polymorphs (rutile and brookite) or metal titanates, were not observed. This result, although it could be related with the even low amount of the dopant metal introduced in the synthesis procedure, is in agreement with the incorporation of M ions into the TiO₂ lattice.

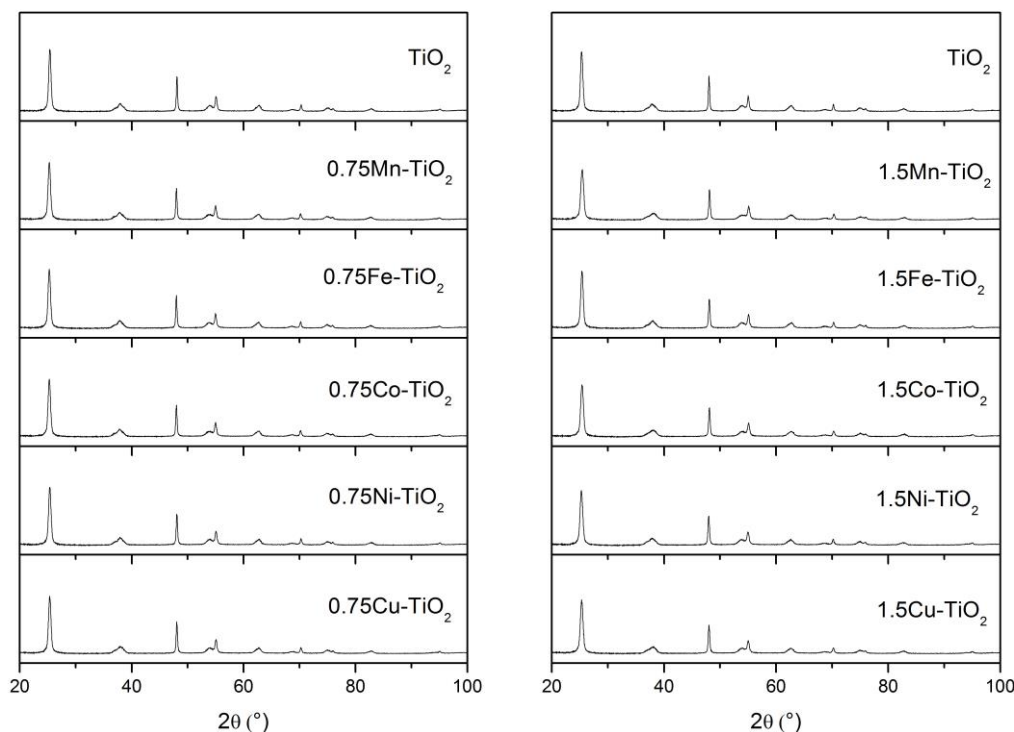


Fig.4.8. Powder XRD patterns of the investigated samples.

No differences were observed among the different samples, irrespectively from the nature and amount of the dopant metal **M** added into the reaction medium. At the same time, the XRD patterns are not significantly affected by the NaOH treatments.

The experimental XRD patterns were fitted following the Rietveld procedure to estimate cell parameters, adopting the crystal structure of pure anatase (Space Group I4₁/amd , n° 141) as initial bias. The fitting procedure did not give excellent results. A representative example of the best results obtained by Rietveld analysis of the undoped TiO₂ is presented in Figure 4.9. From the results of the Rietveld analysis, it is possible to observe some important details:

- the position of the reflections can be reasonably fitted, indicating that the values of the cell parameters obtained by the Rietveld analysis are reliable. The obtained resulted are reported in Table 4.2;
- some reflections are significantly broader and less intense than expected. This is particularly evident for (103), (004), (112) and (105) reflections;
- some reflections are very sharp and more intense than expected (i.e. (200) and (220) reflections).

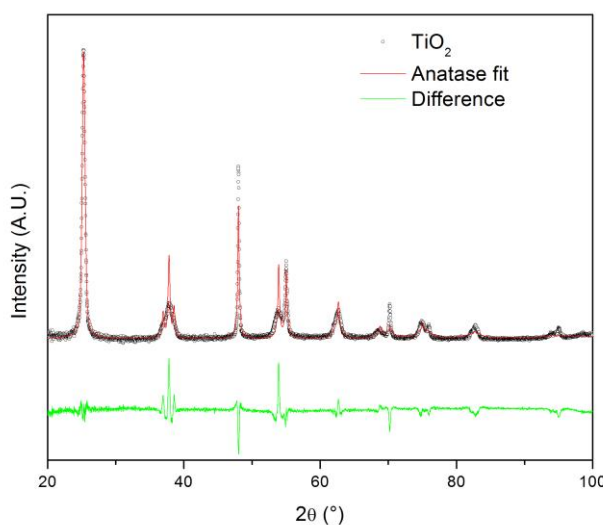


Fig. 4.9. Example of the quality of Rietveld analysis obtained for representative samples: TiO₂, 0.75Fe-TiO₂ and 1.5Mn-TiO₂.

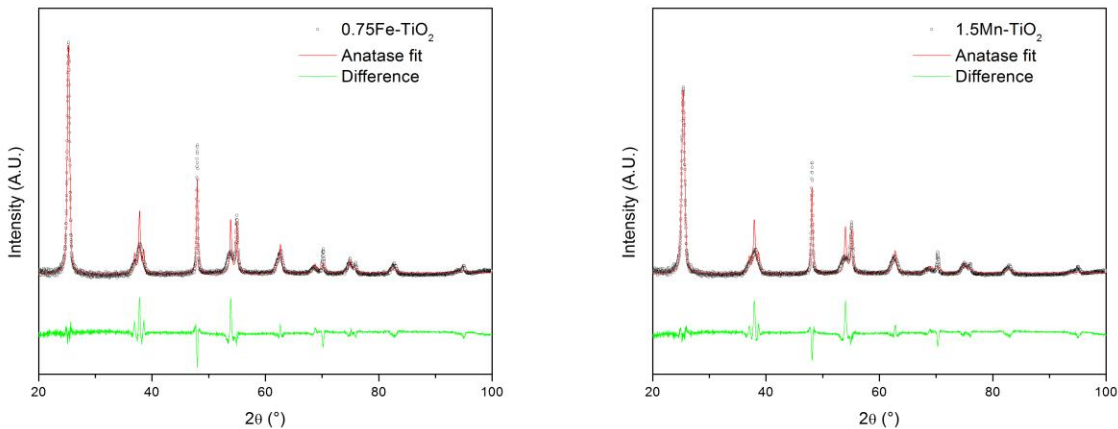


Fig. 4.9 (continuation): Example of the quality of Rietveld analysis obtained for representative samples: TiO₂, 0.75Fe-TiO₂ and 1.5Mn-TiO₂.

Table 4.2. Cell parameters and space groups for the TiO₂ anatase phase.

Sample	a = b (nm)	c (nm)	Sample	a = b (nm)	c (nm)
Theoretical	0.3785	0.9514			
TiO ₂	0.3786	0.9505	TiO ₂		
0.75Mn-TiO ₂	0.3786	0.9501	1.5Mn-TiO ₂	0.3787	0.9505
0.75Fe-TiO ₂	0.3787	0.9505	1.5Fe-TiO ₂	0.3788	0.9512
0.75Co-TiO ₂	0.3786	0.9501	1.5Co-TiO ₂	0.3787	0.9509
0.75Ni-TiO ₂	0.3787	0.9505	1.5Ni-TiO ₂	0.3786	0.9506
0.75Cu-TiO ₂	0.3787	0.9503	1.5Cu-TiO ₂	0.3787	0.9496

Doping of TiO₂ with a transition metal can be considered as dissolution of the metal oxide into the TiO₂ structure. The dopant metal ions can be included into the TiO₂ crystal lattice essentially in two ways: substitutional to Ti⁴⁺ ions or interstitial positions. In both the cases, charge compensation takes place by the formation of oxygen vacancies. The predominance of the substitutional mechanism with respect to the formation of interstitial defects depends on the ionic radii of the dopant metal. Table 4.3 summarizes the ionic radii of the most relevant dopant ions in a 6-fold O coordination, as in the case of insertion of the dopant metal in a substitutional position⁽¹²⁾

Table 4.3 Selected ionic radii(Å) for the dopant metal investigated position⁽¹²⁾.

M	CN = 6	
	HS	LS
Ti ⁴⁺	0.605	
Fe ³⁺	0.645	0.55
Fe ²⁺	0.78	0.61
Mn ⁺²	0.83	0.67
Mn ⁺³	0.645	0.58
Mn ⁺⁴	0.53	
Ni ⁺²	0.69	
Co ⁺²	0.745	0.65
Co ⁺³	0.64	0.545
Cu ⁺¹	0.77	
Cu ⁺²	0.73	

The data summarized in Table 4.3 highlight that the considered metal dopants have an ionic radius comparable or higher than the Ti⁴⁺. Also considering that this fact induces a poor solubility of the various dopant metal oxides in the anatase TiO₂ lattice, the marginal modifications of the cell parameters observed can be related with the very low amount of the dopant metal introduced into the reaction medium during the synthesis of **M-TiO₂** nanosheets.

The unusual width and intensities of some reflections observed in the XRD patterns are in good agreement with the strong anisotropy observed in the nanocrystal shape by TEM investigation (Section 4.2). For this reason, the Rietveld procedure has been modified trying to include a model accounting for the growth of crystallites along a preferred orientation. Various tests have been performed using the Rietveld-Toraya model for plate crystals. Nevertheless, a good refinement of the experimental XRD patterns have never been obtained.

A different approach was followed to account for the anisotropy of the anatase nanosheets. Considering that, for each reflection, the Full Width at Half Maximum (FWHM) is related to the mean crystallite size in the direction

orthogonal to the family of planes responsible for that reflection, the mean crystallite sizes along different directions have been calculated for the most intense reflections following the Scherrer's equation (see Section 2.6). The obtained values are listed in Table 4.4.

Table 4.4 Crystal sizes calculated for different reflections for the investigated samples.

Reflection	Sample					
	TiO ₂	0.75Mn-TiO ₂	0.75Ni-TiO ₂	0.75Co-TiO ₂	0.75Cu-TiO ₂	0.75Fe-TiO ₂
101	21.3	18.6	18.7	18.7	18.5	19.0
103	8.8	8.5	8.4	8.7	8.6	8.4
004	14.5	11.5	11.9	12.6	11.1	12.2
112	11.6	10.3	10.6	11.3	10.1	10.8
200	106.9	103.5	102.2	116.9	105.0	109.8
105	8.0	7.3	7.3	6.7	7.4	7.4
211	44.5	37.2	37.9	38.1	37.0	43.7
204	12.7	12.6	12.8	13.1	13.0	13.5
116	9.5	8.3	8.4	8.1	8.5	8.7
220	187.6	163.9	197.2	168.1	196.0	200.5
215	20.3	11.6	11.8	10.7	9.3	10.7

Reflection	Sample					
	1.5Mn-TiO ₂	1.5Ni-TiO ₂	1.5Co-TiO ₂	1.5Cu-TiO ₂	1.5Fe-TiO ₂	
101	14.8	16.4	16.0	16.4	18.7	
103	7.5	9.2	7.9	8.0	9.1	
004	9.0	10.7	9.2	9.2	11.1	
112	8.1	10.1	8.7	8.9	10.9	
200	135.1	77.0	80.8	70.1	99.3	
105	5.9	7.0	6.5	6.7	7.4	
211	30.5	28.4	33.0	30.5	45.1	
204	14.9	11.7	10.9	11.4	15.4	
116	6.7	6.8	6.6	6.7	7.8	
220	73.7	67.2	48.4	62.4	70.4	
215	6.1	11.3	9.7	9.2	11.1	

These data highlights two important features:

- the crystallite size is very large for the reflections with $l = 0$: (200) and (220). These reflections are originated by families of planes orthogonal to the c axis and parallel to the {001} facets exposed by the nanosheets.
- all the other reflections show smaller crystallite sizes because they correspond to groups of planes that are not orthogonal to the c axis. Notably, crystallite size decreases as the value of l (in hkl) increases.

All these features are consistent with the planar morphology observed by TEM, with the nanosheets having the thicker dimension along the c axis of the anatase structure.

4.4 Dopant metal content in M-TiO₂: ICP-AES analysis

The aim of doping TiO₂ with transition metals is to shift the absorption spectrum to longer wavelengths and, therefore, to more efficiently harvest light in the visible range. The real amount of dopant incorporated in the samples was determined by ICP-AES after complete dissolution of the samples by treatment. Briefly, the samples accurately weighed by duplicated (0.01 and 0.02 g), are dissolved by acid digestion in a mixture of hydrochloric acid (HCl) and hydrofluoric acid (HF). The samples are put on an Erlenmeyer flask with the acid solution and heating in a hot plate without stirring. Then the solution is taken away to a known volume and the amount of transition metal is measured by the ICP instrument. The results are reported in Table 4.5, expressing the transition metal content as weight %.

Table 4.5 Real metal content as resulting from ICP-AES analysis (± 0.01 wt%)

Sample	M content (%p/p)
TiO ₂	-----
0.75Fe-TiO ₂ / 1.5Fe-TiO ₂	0.04 / 0.80
0.75Mn-TiO ₂ / 1.5Mn-TiO ₂	0.19 / 0.31
0.75Co-TiO ₂ / 1.5Co-TiO ₂	0.26 / 0.29
0.75Cu-TiO ₂ / 1.5Cu-TiO ₂	0.18 / 0.35
0.75Ni-TiO ₂ / 1.5Ni-TiO ₂	0.18 / 0.11

The results of ICP-AES analysis clearly indicate that the effective content of the dopant metal introduced into the TiO₂ nanosheets significantly differs from the nominal amounts (0.75wt% and 1.5wt%, respectively). As a general rule, the dopant metal introduced into the reaction mixture is only partially incorporated into the final product. Although in a different extent depending on the nature of the dopant metal, the increase of the concentration of the transition metal into the initial reaction solution reflected in the increase of the dopant metal content in the final product.

The amount of dopant metal detected by ICP-AES analysis are very low, justifying the negligible modifications observed in cell parameters for the different samples (Table 4.2). The incorporation of transitional metal ions into the anatase TiO₂ crystalline structure depends essentially by the charge compensation mechanism taking place, by the ionic radius of the dopant metal and by the presence of other point defects present in the host matrix. Regarding this last point, HR-TEM and XRD characterisation (sections 4.2 and 4.3) clearly evidenced the high crystallinity in the TiO₂ nanosheets produced with a very low defect concentration, in agreement with the low content on dopant metals.

The discrepancy between nominal and effective amount of dopant materials present in the TiO₂ nanosheets can be related with the high F⁻ concentration realised in the reaction medium during the hydrothermal

synthesis. In fact, the coordination of F⁻ to the metal ions could hinder the insertion of the dopant during the growth of the TiO₂ nanocrystals.

4.8 Determination of F content

The synthesized samples have been treated with NaOH in order to remove fluoride ions from the surface of the materials. This treatment at low temperature was selected instead of thermal treatment at 500°C to avoid modifications of morphology and phase composition of the nanosheets. The amount of F⁻ removed during NaOH treatments was determined by ionic chromatography. The obtained results are presented in Table 4.6 and pictorially in Figure 4.10.

Table 4.6: Concentration of F⁻ (expressed in mg L⁻¹) detected in the washing solution during consecutive NaOH treatments.

Sample	Washing treatment			
	1°	2°	3°	4°
Undoped	341.6	85.7	5.5	1.2
0.75Mn-TiO₂-NaOH	152.0	82.8	18.6	2.1
0.75 Fe--TiO₂-NaOH	183.7	81.9	7.2	1.4
0.75 Ni-TiO₂-NaOH	152.4	105.7	13.4	1.7
0.75 Cu-TiO₂-NaOH	160.2	74.9	8.6	1.6
0.75 Co-TiO₂-NaOH	290.1	98.0	13.4	1.9
1.5 Mn-TiO₂-NaOH	146.5	118.7	13.5	3.2
1.5 Fe-TiO₂-NaOH	144.5	104.2	4.9	1.2
1.5 Ni-TiO₂-NaOH	138.5	97.4	12.9	1.4
1.5 Cu-TiO₂-NaOH	150.9	120.0	8.1	1.7
1.5 Co-TiO₂-NaOH	148.2	88.9	17.4	2.9

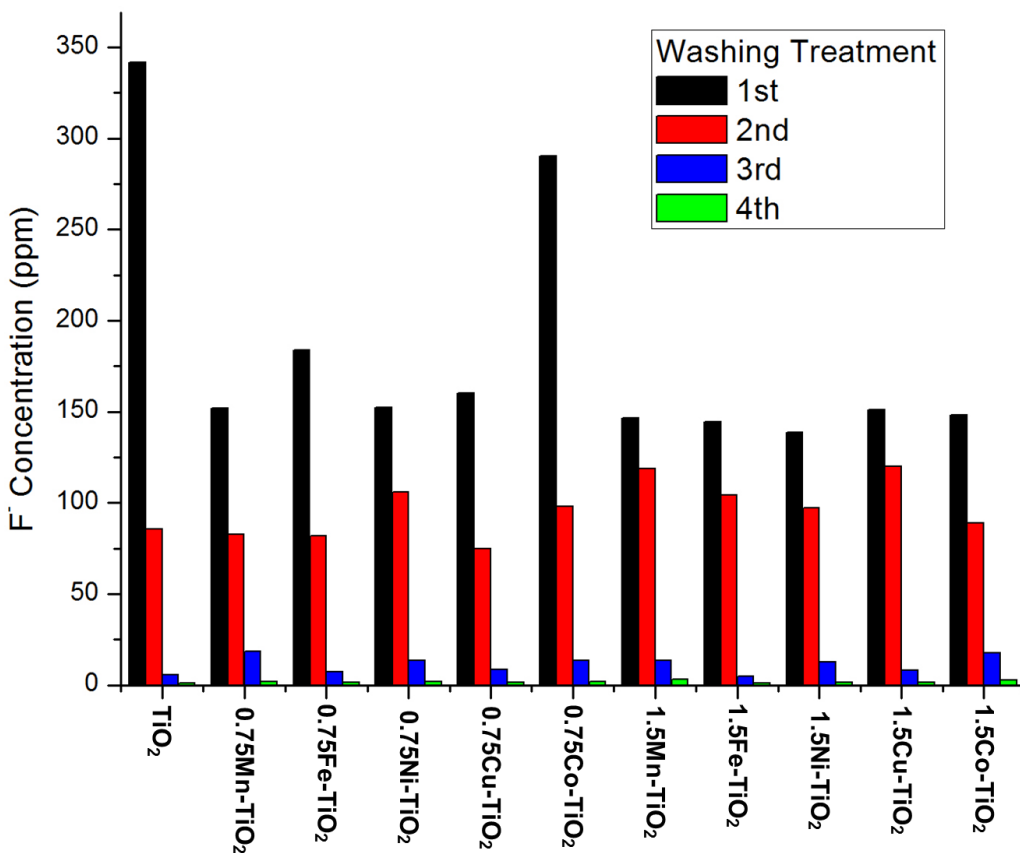


Fig. 4.10. Pictorial representation of the concentration of F⁻ (expressed in mg L⁻¹) detected in the washing solution during consecutive NaOH treatments.

These data show that the amount of F⁻ desorbed during consecutive NaOH treatments progressively decreased. After the forth treatment, the amount of fluoride desorbed is very low, indicating that a further treatment will lead to negligible modifications of the concentration of superficial F in the samples. Notably, no significant differences are observed among the samples.

Energy Dispersive X-ray Spectroscopy, or EDS, can provide rapid qualitative, or with adequate standards, quantitative analysis of elemental composition of the bulk of the materials. In the present work, this technique was used to determine the overall amount of the F with respect to TiO₂ both before and after the NaOH washing process. Table 4.7 summarizes the obtained results and Figure 4.11 shows the F/Ti molar ratios calculated from the EDS analysis.

Table 4.7. X-EDS quantitative analysis performed to determine the quantity of F⁻ ions in the different TiO₂ nanosheets samples before and after washing with NaOH.

Sample	F wt%	Ti wt%	Sample	F wt%	Ti wt%
TiO ₂	3.04	53.8	TiO ₂ -NaOH	1.99	56.81
0.75Mn-TiO ₂	3.04	55.92	0.75Mn-TiO ₂ -NaOH	1.84	56.25
0.75Ni-TiO ₂	2.81	53.78	0.75Ni-TiO ₂ -NaOH	2.29	53.71
0.75Co-TiO ₂	2.87	54.71	0.75Co-TiO ₂ -NaOH	2.05	56.02
0.75Cu-TiO ₂	3.06	54.25	0.75Cu-TiO ₂ -NaOH	2.21	54.49
0.75Fe-TiO ₂	3.33	52.51	0.75Fe-TiO ₂ -NaOH	2.11	56.74
1.5Mn-TiO ₂	2.88	54.11	1.5Mn-TiO ₂ -NaOH	1.78	57.93
1.5Ni-TiO ₂	2.73	56.31	1.5Ni-TiO ₂ -NaOH	2.14	54.85
1.5Co-TiO ₂	2.91	55.88	1.5Co-TiO ₂ -NaOH	2.28	53.13
1.5Cu-TiO ₂	3.00	55.15	1.5Cu-TiO ₂ -NaOH	2.01	56.14
1.5Fe-TiO ₂	3.25	53.11	1.5Fe-TiO ₂ -NaOH	1.98	57.48

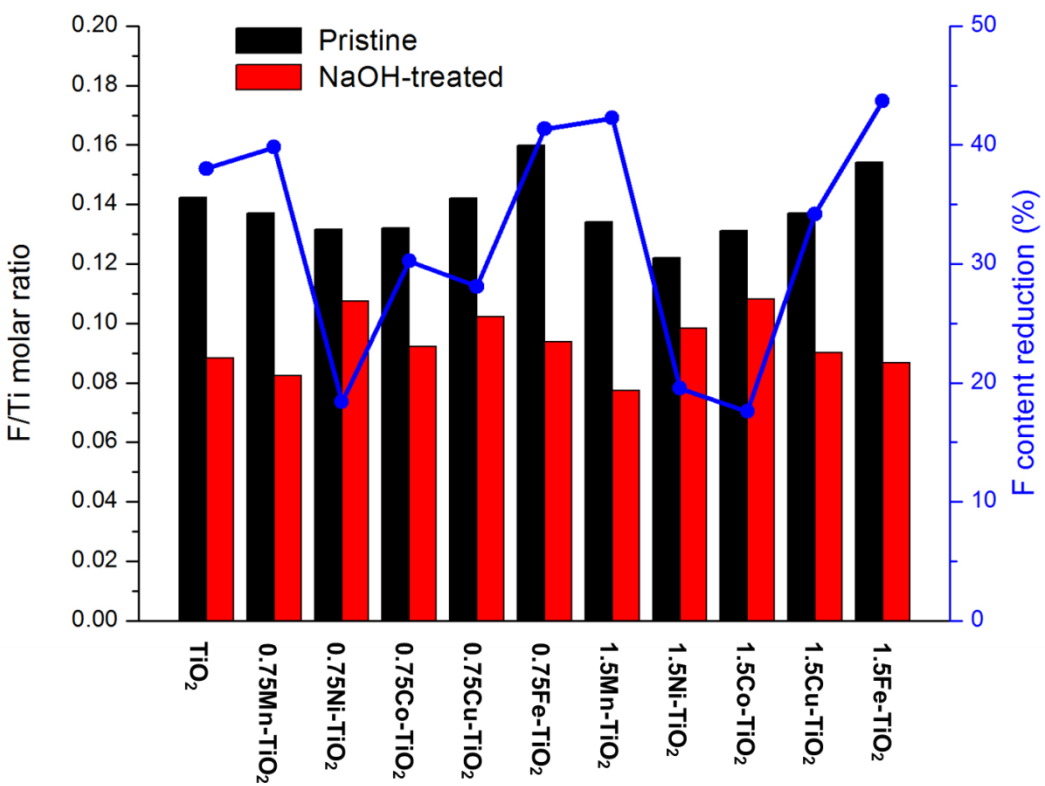


Fig. 4.11 F/Ti molar ratios calculated from the EDS analysis.

In agreement with the detection of F⁻ in washing solution, EDS analysis revealed a significant decrease in the content of fluorine after NaOH washing process. Nevertheless, the amount of F is still significant after removal of surface fluorides, suggesting that F is included also in the bulk of the TiO₂ nanosheets (or at least in the sub-surface layers). Undoped TiO₂, Mn-TiO₂ and Fe-TiO₂ materials released the highest fraction of F⁻ while this is lowest for Ni-TiO₂ materials.

4.7. Surface composition characterization

To thoroughly investigate the photocatalytic performance of the synthesized TiO₂ nanosheets, an XPS analysis was performed to analyse and determine the chemical composition on the surface of the synthesized products. The analysis has been performed mainly on the samples with the higher amount of dopant metals (**1.5M-TiO₂** samples). Nevertheless, the amount of dopant metals is always below the detection limit of the XPS technique.

The analysis of the Ti 2p region (Figure 4.12) highlighted the presence of the two bands, located at 4459.1 and 464.5 eV. These are attributed to the Ti 2p_{1/2} and Ti 2p_{3/2} energy levels, respectively^(2,13–15). The splitting difference of 5.8 eV between the two bands indicates the existence of the Ti⁴⁺ species in the samples. No significant modification of the Ti spectra has been observed by introduction of the dopant metals (differences are less than 0.1 eV). This result is probably related with the very low amounts of the dopant metals introduced during the nanosheets synthesis. On the other hand, when the F⁻ ions are removed from the surface of the samples by NaOH treatments, the binding energies of Ti 2p_{1/2} and 2p_{3/2} are slightly shifted to lower BE with respect to the correspondent pristine samples, even if a maximum shift of 0.4 eV is observed for **1.5Ni-TiO₂**. Notably, this is also the sample which gave the highest removal of fluoride form the material. The little shift in the binding energy of Ti may be due to the interference of the electron cloud between the F⁻ and Ti surface atoms: once the interaction between the Ti-F⁻ ions has been minimized, a higher electrical density on Ti is present.

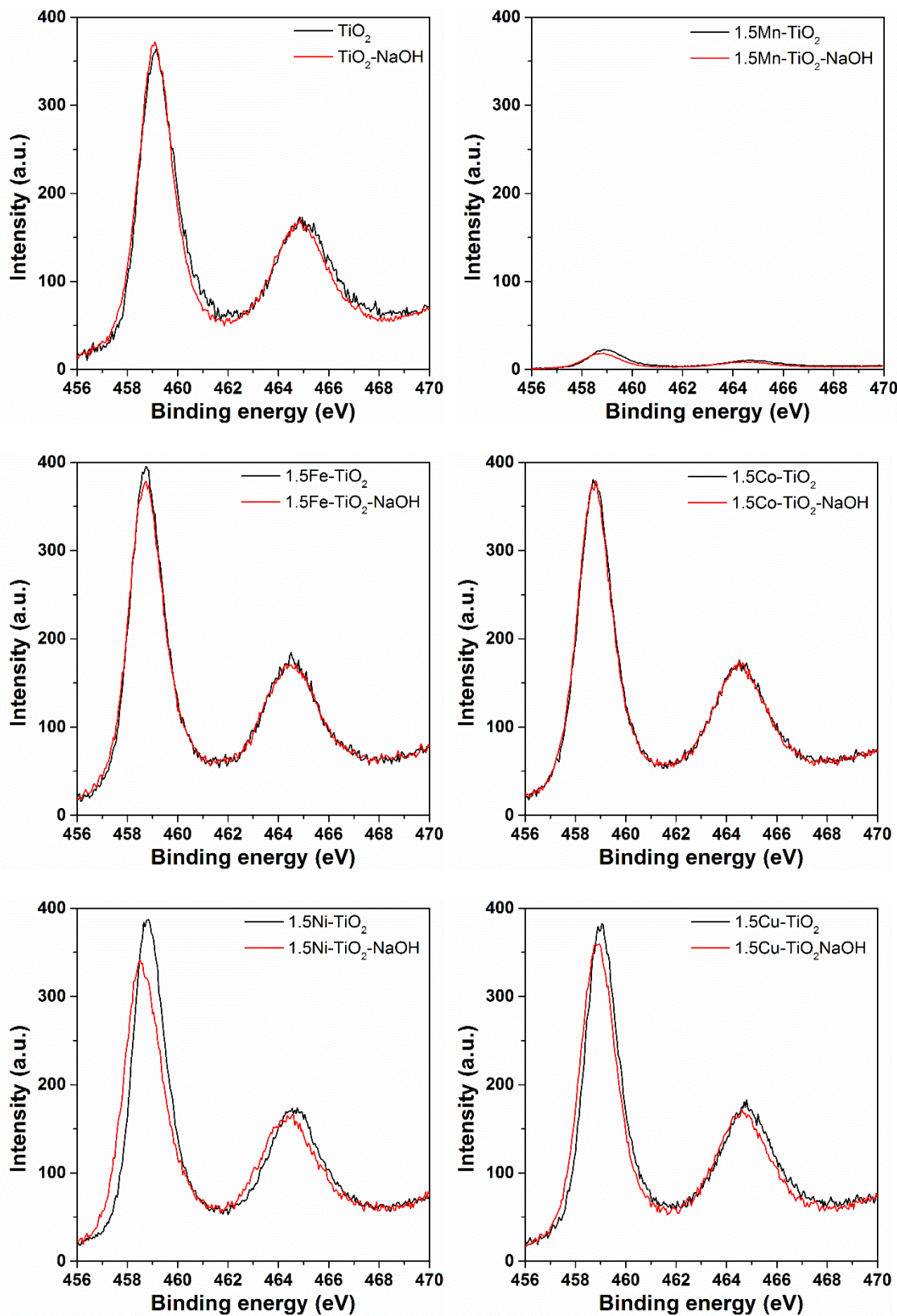


Fig.4.12. XPS spectra of Ti 2p region for the investigated samples.

Figure 4.13 shows the XPS spectra for the F 1s peak in the investigated samples. In the undoped TiO₂ samples, this signal is a single peak with a binding energy of 684.9 eV, typical for the fluorinated TiO₂ system, such as Σ Ti-F species on the TiO₂ crystal surface^(2,10,13,14,16,17). These measures confirm the effectiveness of the washing process in minimizing a significant quantity of the F⁻ ions on the surface of the photocatalysts. Furthermore, no signal for the F⁻ ion was found in the TiO₂ lattice (binding energy = 688.5-689.5 eV)^(10,13). Figure 4.13 shows that the binding energies of Ti 2p_{3/2} and Ti 2p_{1/2} are equal to that of the Ti⁴⁺ of bulk TiO₂.

The XPS spectra corresponding to the F 1s signal in the doped samples Mn-TiO₂, Ni-TiO₂, Co-TiO₂, Cu-TiO₂ and Fe-TiO₂ were characterized by 2 peaks. Notably, the overall intensities of F 1s signal in doped samples is significantly lower than that observed in the undoped TiO₂ sample. The one at lower BE is detected at approximately 684.5 eV, a value slightly lower than that observed in undoped TiO₂, and is ascribable to F-species adsorbed on the surface. The peak at higher BE can be reasonably associated with sub-surface or bulk F species, strongly bounded to the TiO₂ lattice^(11,18). The presence of this new feature could be related with the charge compensation mechanism deriving with the substitution of Ti⁴⁺ with the dopant metals.

After washing treatment with NaOH, the intensities of the surface F⁻ species (at BE = 684.5 – 689.0 eV) decreased, in agreement with detection of F⁻ ions in the washing solutions and with the decrease of the overall F content evidenced by EDS. Notably, the intensities of strongly bound F species in **1.5M-TiO₂** samples are not affected by washing treatment. In agreement with ionic chromatography analysis, the undoped TiO₂ material is the one that release the higher amount of F⁻ ions. The results from XPS clearly indicate that a fraction of superficial F cannot be removed from the surface of the materials, where it remains adsorbed.

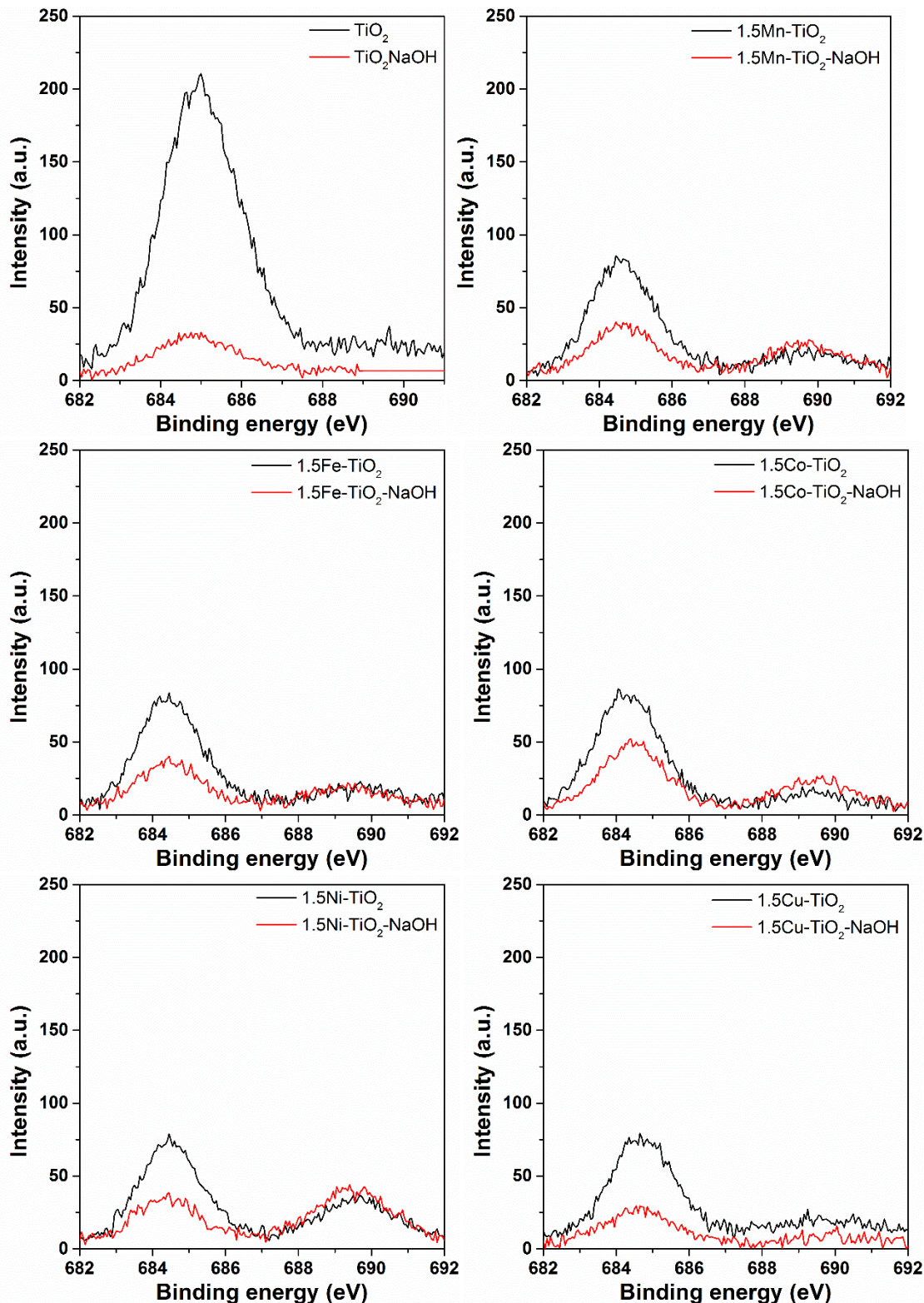


Fig.4.13 XPS spectra of F 1s region for the investigated samples.

The binding energy of the O 1s peak of TiO₂ is approximately 530.5 eV; this is ascribed to the O-Ti⁴⁺ interaction. When comparing the doped samples, it can be seen that the higher peaks shift to lower energy regions, in the order Mn>Ni=Co=Cu>Fe. This can be attributed to the different variations in electronegativity between the Ti- and dopant ions and it confirms the formation of an M-O-Ti complex in doped materials. The shoulder centred at 530.5 eV in all the samples is attributed to the OH groups that are absorbed onto the surface⁽¹³⁾.

Compared with the XPS spectra of the O 1s for the samples after washing with NaOH, Figure 4.14 shows that there is a substantial decrease of the band related to OH groups. This can be rationalized assuming that removed fluorides are replaced with H₂O adsorbed molecularly instead of in a dissociative way (and therefore forming new OH groups). In this case, adsorbed water will be removed from the surface of the materials during drying (after the NaOH washing treatments) and even during the conditioning treatment before XPS analysis.

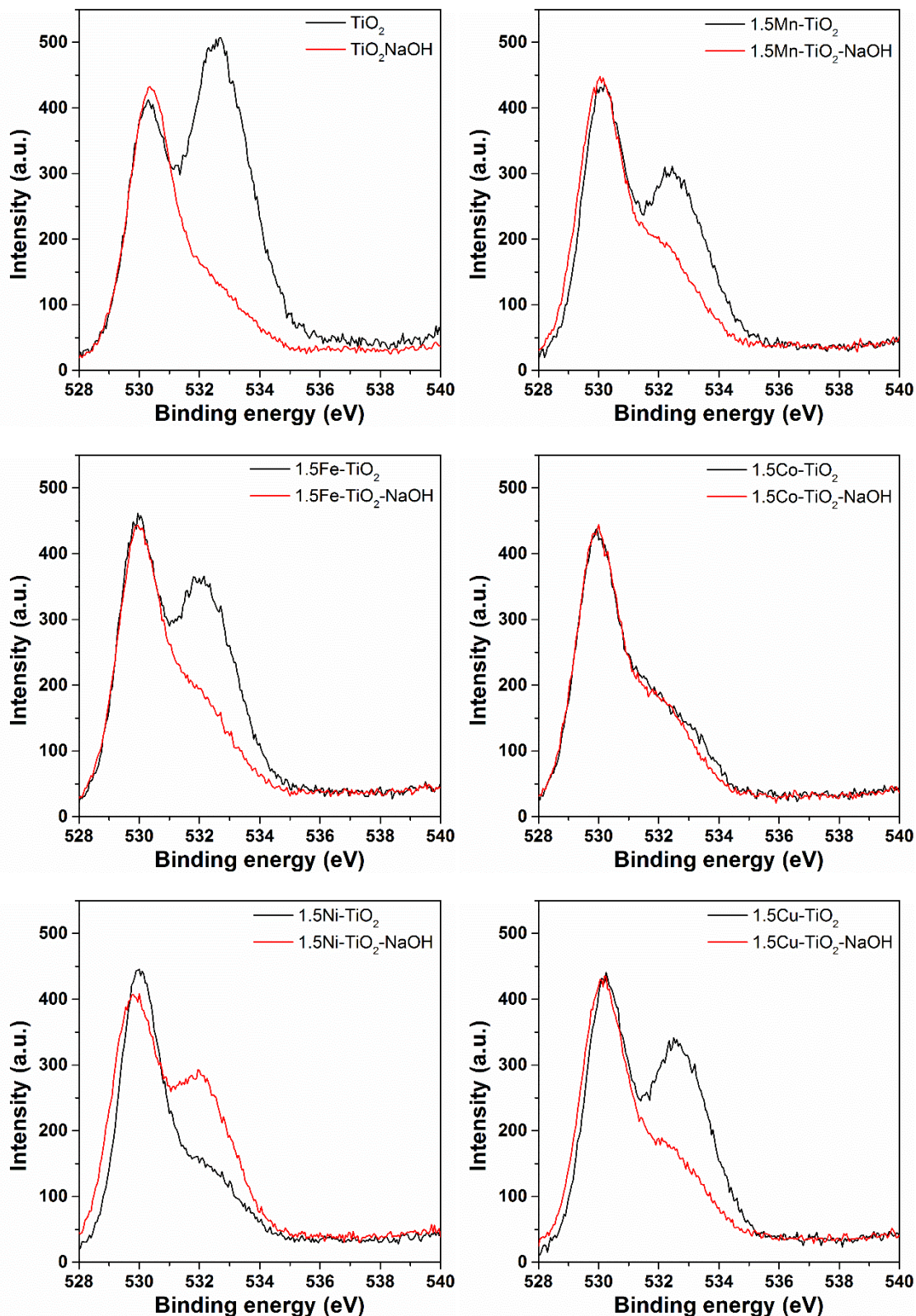


Fig.4.14 XPS spectra of O 1s region for the investigated samples.

4.5 Nitrogen adsorption-desorption isotherms: BET surface area and average pore size

Textural analysis was undertaken using the N₂ isotherm physisorption method. Figure 4.15 shows the physisorption curve for all studied samples.

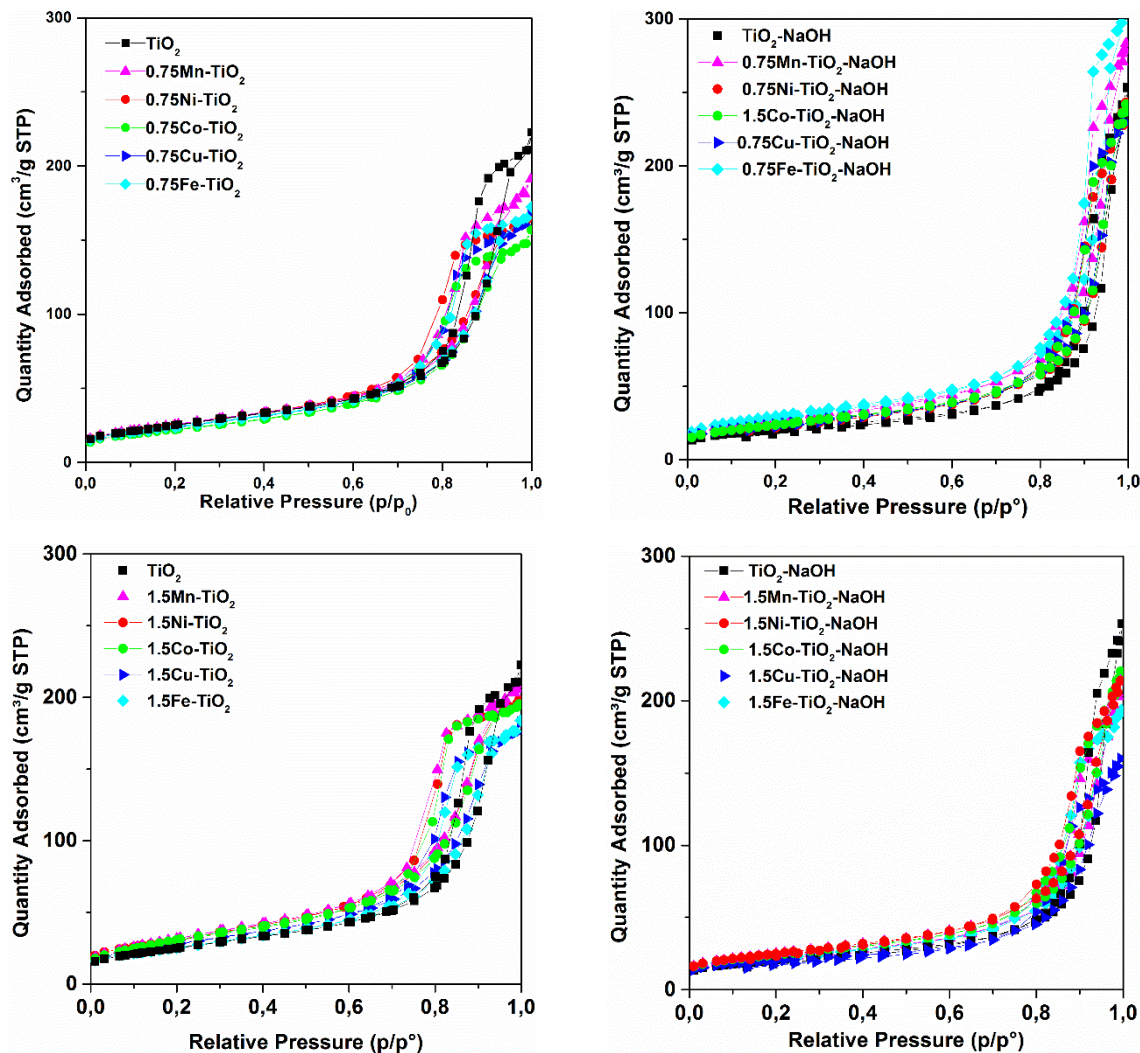


Fig. 4.15. Physisorption N₂ isotherm curve for the investigated samples

According to the IUPAC classification⁽¹⁹⁾, all the samples show Type IV. This type of curve is attributed to mesoporous solids (2 nm < pore size < 50 nm). The hysteresis loop (H1 from the IUPAC classification) is associated with the secondary process of capillary condensation, which results in the complete filling of the mesoporous solid at $p/p^0 < 1$. Type H1 hysteresis is characteristic of solids crossed by channels with uniform sizes and shapes. These physisorption curves were of the same type for all the samples and no variation was detected

between the TiO₂ nanosheets doped with different transition metals, nor when the amount of doped metal was increased. According to the literature^(2,7), the use of alcohol as a structural agent may be responsible for the construction of mesoporous structures during solvothermal synthesis.

Table 4.8 summarises the textural properties of the investigated materials. All the samples present high surface area (above 80 m²/g), with good pore volumes and pore sizes around 8–23nm. It must be underlined that, increasing the amount of dopant metal, surface area and pore volume significantly increases. This is reasonably in agreement with the slightly reduction of average length of nanosheets observed by TEM.

Table 4.8. Textural properties of the investigated samples.

Sample	BET surface area (m ² /g)	PV (cm ³ /g)	Average pore size (nm)
TiO ₂	87	0.28	13
0.75Mn-TiO ₂	94	0.28	13
0.75Fe-TiO ₂	88	0.26	12
0.75Co-TiO ₂	80	0.23	11
0.75Ni-TiO ₂	93	0.25	9
0.75Cu-TiO ₂	88	0.23	12
1.5Mn-TiO ₂	119	0.31	9
1.5Fe-TiO ₂	93	0.27	11
1.5Co-TiO ₂	80	0.29	11
1.5Ni-TiO ₂	113	0.30	11
1.5Cu-TiO ₂	103	0.27	11
TiO ₂ -NaOH	68	0.37	23
0.75Mn-TiO ₂ -NaOH	94	0.43	23
0.75Fe-TiO ₂ -NaOH	100	0.46	23
0.75Co-TiO ₂ -NaOH	81	0.37	19
0.75Ni-TiO ₂ -NaOH	80	0.37	13
0.75Cu-TiO ₂ -NaOH	81	0.35	23
1.5Mn-TiO ₂ -NaOH	77	0.32	19
1.5Fe-TiO ₂ -NaOH	75	0.29	19
1.5Co-TiO ₂ -NaOH	81	0.33	19
1.5Ni-TiO ₂ -NaOH	85	0.33	16
1.5Cu-TiO ₂ -NaOH	63	0.24	16

The pore size distributions, calculated by the BJH method from the desorption branch of the isotherms, are presented in Figure 4.16. The pore size distribution that was evaluated before and after NaOH washing shown a clear effect on

the samples XX-M-TiO₂-NaOH. Generally, results in an increase in the average pore diameter and a decrease in the BET specific surface area. This decrease is more pronounced for the samples TiO₂/TiO₂-NaOH and 1.5Cu-TiO₂/1.5Cu-TiO₂-NaOH

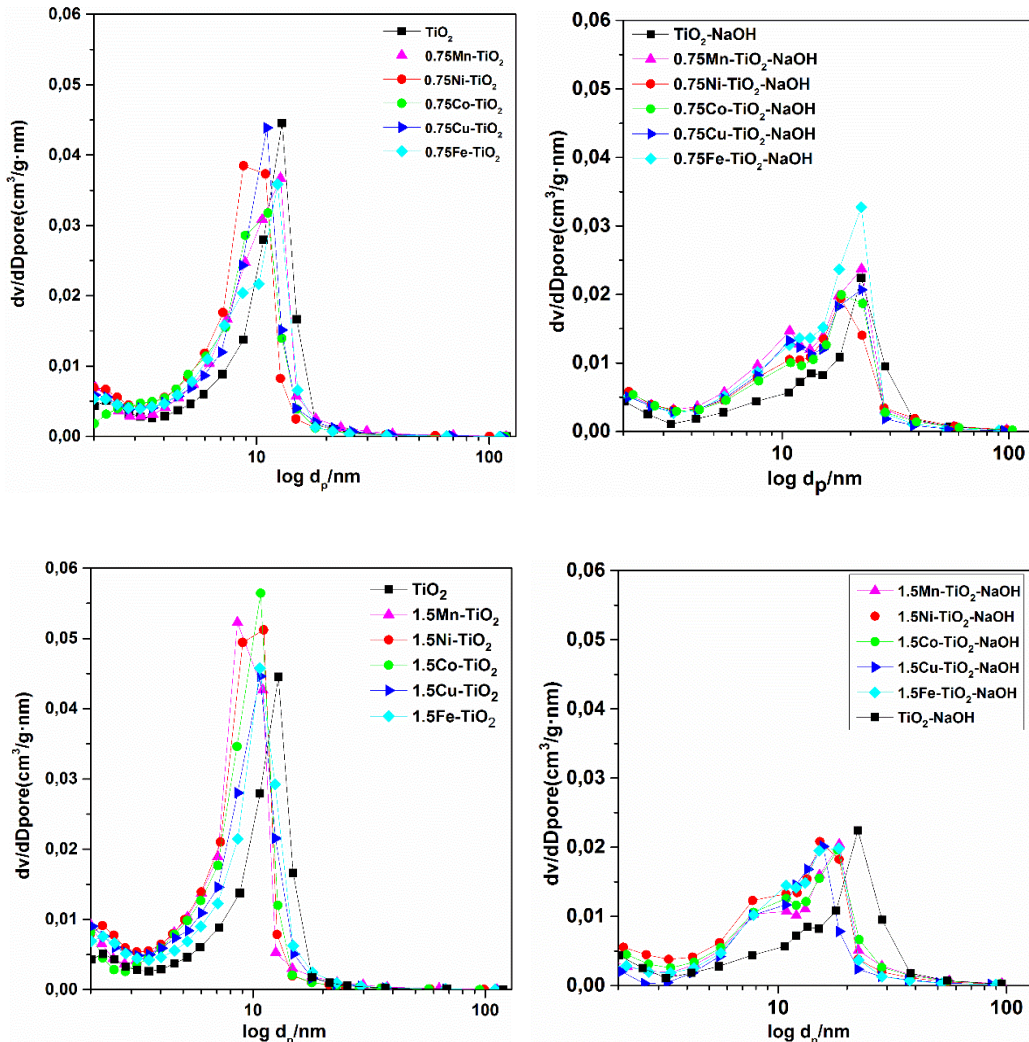


Fig. 4.16. Pore size distributions for the investigated samples

Comparing the surface area of both doped series, a substantial increment in the BET surface area is observed increasing the amount of dopant metal. This fact is more evident in the case of the **Co-TiO₂** nanosheets, followed by Mn, Cu, and Ni, and to a lesser degree the Fe-doped TiO₂ nanosheets. This increase can be explained considering that the correspondent metal nitrates have been used as precursors using during the synthesis to obtain the M-TiO₂ nanosheets. The (NO₃)⁻ ions could be adsorbed on the surface of the

nanosheets during the synthesis and competing for F⁻ ions responsible for the anisotropic growth of TiO₂ crystals⁽²²⁾. Increasing the amount of metal, an increase the amount of nitrate ions in the reaction medium is obtained and therefore anisotropic growth increases^(13,23). The addition of dopant precursors in the reaction medium may inevitably influence the nucleation and growth of anatase TiO₂ nanosheets so that no TiO₂ nanosheets with desirable properties could be synthesized⁽²⁴⁾.

In order to study how the (NO₃)⁻ ions influence the value of the surface area, the following experiment was carried out. The amount of (NO₃)⁻ present in the inorganic salt used as the metal precursor was calculated for both synthesized samples, **0.75M-TiO₂** and **1.5M-TiO₂**. Then, instead of using the inorganic salt, a similar amount of (NO₃)⁻ ions was added as HNO₃. The idea was to discover if increased quantities of (NO₃)⁻ ions in the reaction medium influenced the BET surface area. Figures 4.17 show the physisorption isotherms for the obtained materials, together with the corresponding values for the BET surface area.

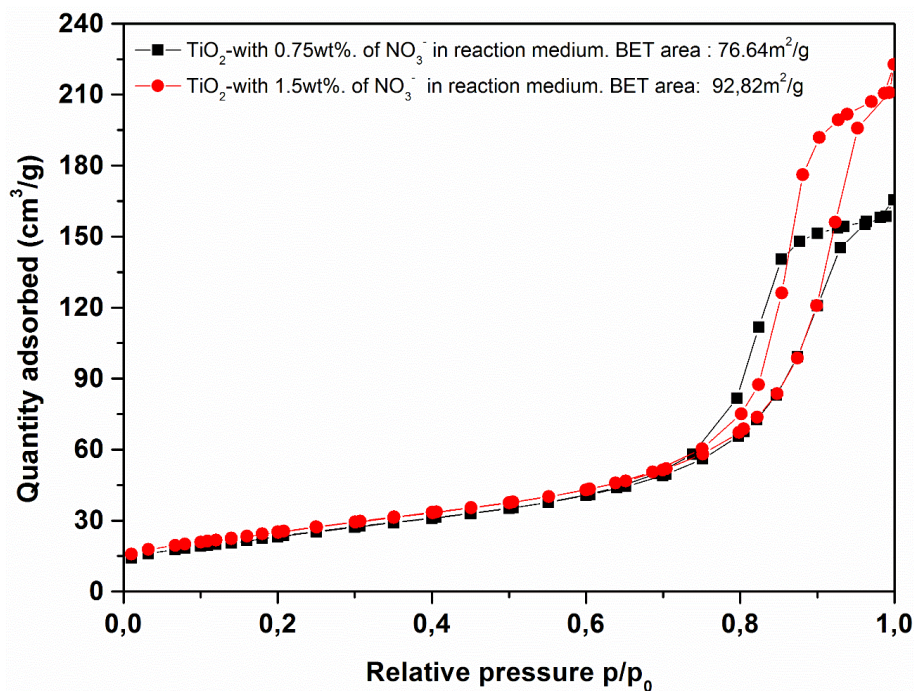


Fig.4.17. Physisorption N₂ isotherm curve for the undoped TiO₂ nanosheets with (NO₃)⁻ amounts equivalent to the quantity of (NO₃)⁻ present in 0.75 wt% doped samples and curve for the undoped TiO₂ nanosheets with (NO₃)⁻ amounts equivalent to the quantity of (NO₃)⁻ present in 1.5 wt% doped samples.

It can be seen that in the case where more (NO₃)⁻ ions are present in the reaction medium, the BET surface area is larger. This simple experiment is useful for demonstrating that the increase in the BET surface area is due to the presence of more (NO₃)⁻ ions in the reaction medium. This phenomena has been reported in previous studies⁽¹³⁾.

4.6 Estimating the band-gap value of the photocatalysts by means of the UV-Vis diffuse reflectance technique

The band-gap value was determined using the transformed diffuse reflectance technique according to the Kubelka–Munk theory^(25,26), as shown in Table 4.9. UV-Vis absorbance spectra for all the samples is represented in Figure 4.18. Figure 4.19 presents the Tauc Plot for indirect and direct band-gap of the studied samples. There is a significant increase in absorption at wavelengths around 350 nm-400 nm. The absorption spectrum for all the M-TiO₂ nanosheets reveals enhanced absorption in the visible light region. Observing the band-gap we can see that the values are below the nominal value for anatase TiO₂ (3.2eV)^(10,27–29). The band-gap value not only decreases for the samples with transition metals as dopants but also for the undoped ones. This fact can be explained by morphology. Our TiO₂ nanosheets are around 5 nm thick, as shown in Table 4.1. In accordance with the Brus equation, there is a band-gap change as a function of particle size due to the quantum size effect. The smallest band-gap value is for the Fe-TiO₂ nanosheets in both doped series, at least for indirect Eg value and almost for direct Eg value. For the other samples the band-gap value is similar and slightly below the values corresponding to the undoped TiO₂ sample. The low amount of doped metal in the TiO₂ lattice justifies the low reduction in the Eg values of the doped samples respect to the undoped TiO₂ nanosheets.

Table 4.9 Determination of the band gap values from a diffuse reflectance spectrum using the Tauc plot.

Sample	indirect band-gap value (eV)	direct band-gap value (eV)
TiO ₂	2.93	3.01
0.75Mn-TiO ₂	2.88	3.19
0.75Fe-TiO ₂	2.77	3.17
0.75Co-TiO ₂	2.87	3.24
0.75Ni-TiO ₂	2.87	3.19
0.75Cu-TiO ₂	2.86	3.22
1.5Mn-TiO ₂	2.87	3.22
1.5Fe-TiO ₂	2.84	3.11
1.5Co-TiO ₂	2.85	3.20
1.5Ni-TiO ₂	2.88	3.20
1.5Cu-TiO ₂	2.80	3.22

This increase in the amount of dopant is either accompanied by a slight decrease in the band-gap energy, or this remains constant. In this sense, the minimum band-gap value was found in the sample doped with iron in both series of doped samples. Another example where it is possible to see the correlation between the amount of dopant and the value of the band-gap is in the sample doped with Cu; for this sample, as in the case of the Fe-TiO₂ sample, increasing Cu involves a decrease in the band-gap energy. This effect is less remarkable for the Mn-TiO₂ sample and non-existent for the Co-TiO₂ and Ni-TiO₂ samples, where the band-gap value is equal for both series of doped samples.

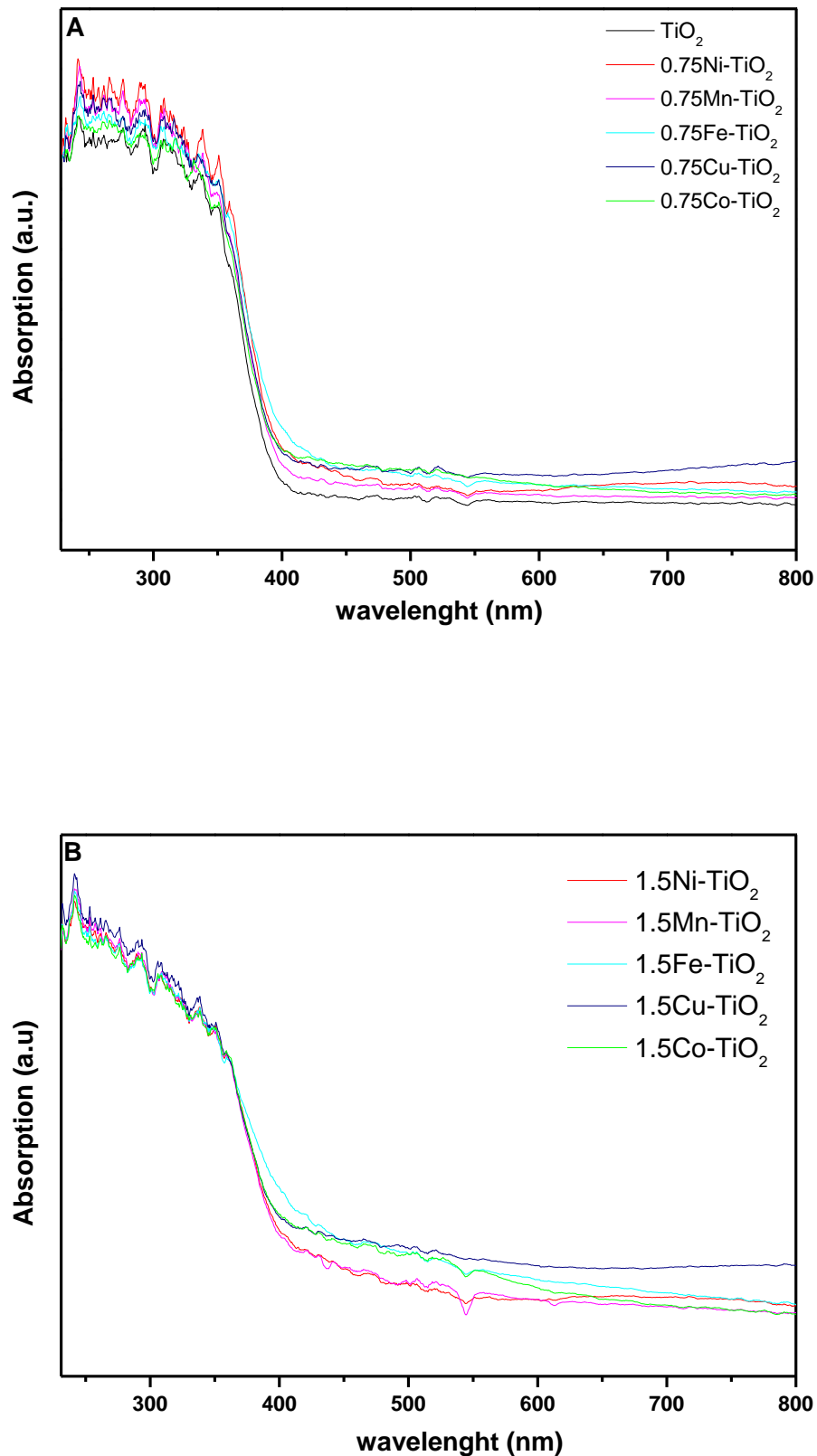


Fig 4.18. UV-Vis diffuse reflectance absorption spectroscopy of 0.75-TiO₂ nanosheets and undoped nanosheets(A), and 1.5M-TiO₂ nanosheets (B).

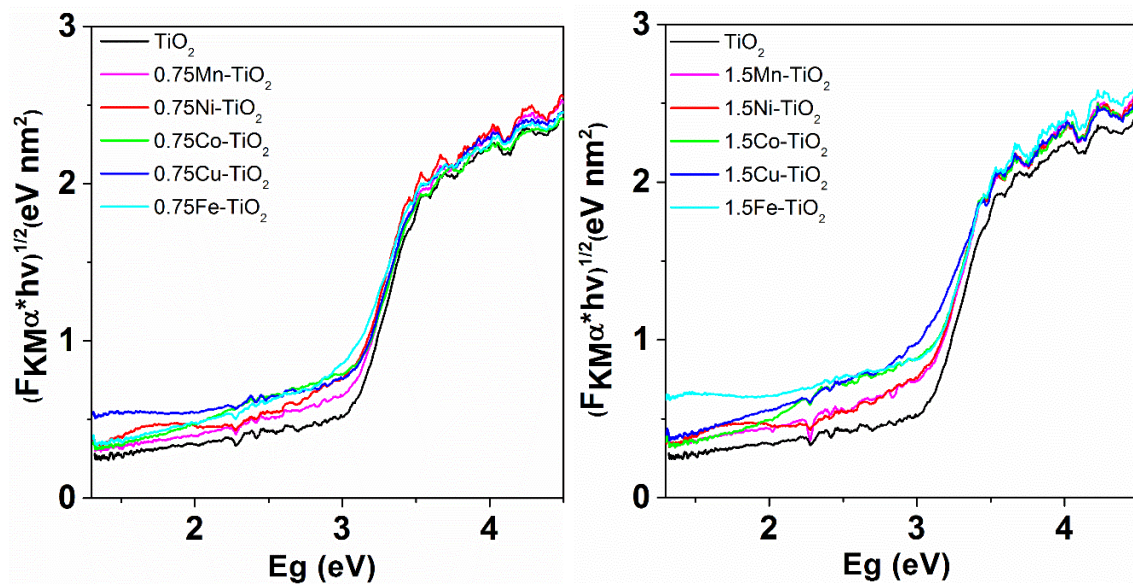
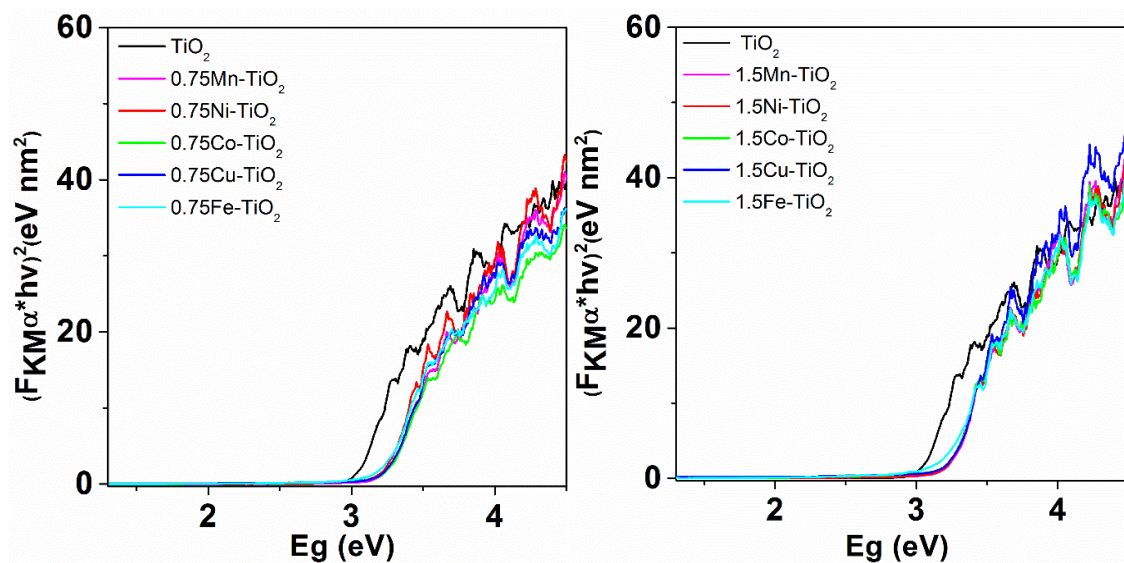
Indirect band-gap Tauc Plot ($h\nu - (h\nu F(R^\infty))^{1/2}$)Direct band-gap Tauc Plot ($h\nu - (h\nu F(R^\infty))^2$)

Fig 4.19. Tauc Plot for indirect and direct E_g calculated graphs. The value associated with the point of intersection of the line tangent to the plotted curve inflection point with the horizontal axis ($h\nu$ axis) becomes the band gap E_g value.

4.7 Size distribution of Pt nanoparticles

The size and distribution of the Pt nanoparticles have been analysed on the samples collected after photocatlaytic tests. Pt nanoparticles are formed on the surface of the photocatalysts by photodeposition from Pt²⁺ ions during the initial period of the H₂ production tests and act as co-catalysts for the process, favouring the h⁺/e⁻ separation and providing the catalytic sites for H⁺ reduction to adsorbed H and for their recombination to H₂. HAADF-STEM images of the samples are presented in Figure 4.20, where Pt nanoparticles can be recognized as small bright spots.

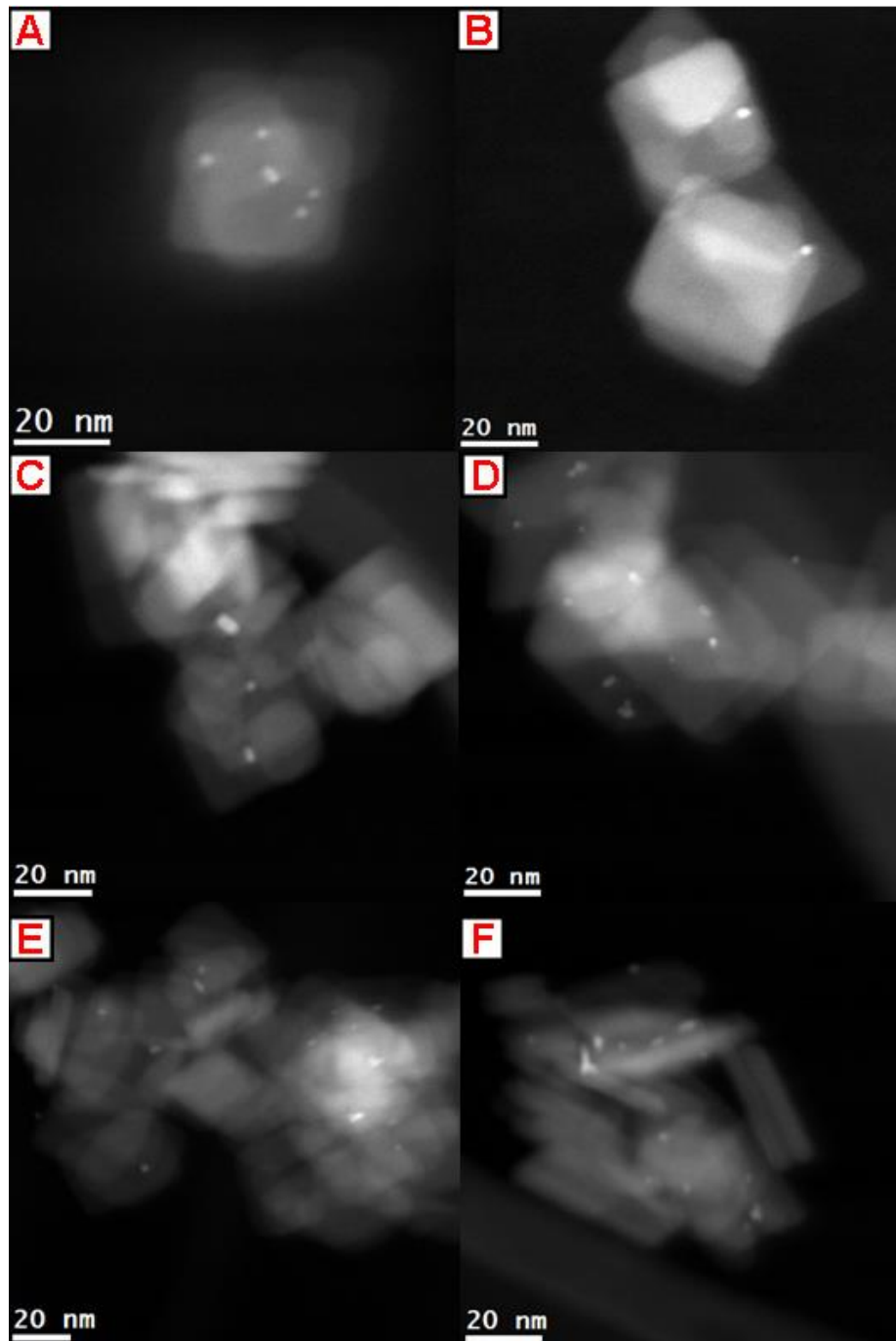


Fig. 4.20. HAADF images for the two doped series (0.75 wt% and 1.5 wt% of metal doped) for each transition metal used as a dopant with 0.2 wt% of Pt as co-catalyst.
A) 0.75Mn-TiO₂-NaOH B) 1.5Mn-TiO₂-NaOH C) 0.75Ni-TiO₂-NaOH D) 1.5Ni-TiO₂-NaOH
E) 0.75Co-TiO₂-NaOH F) 1.5Co-TiO₂-NaOH

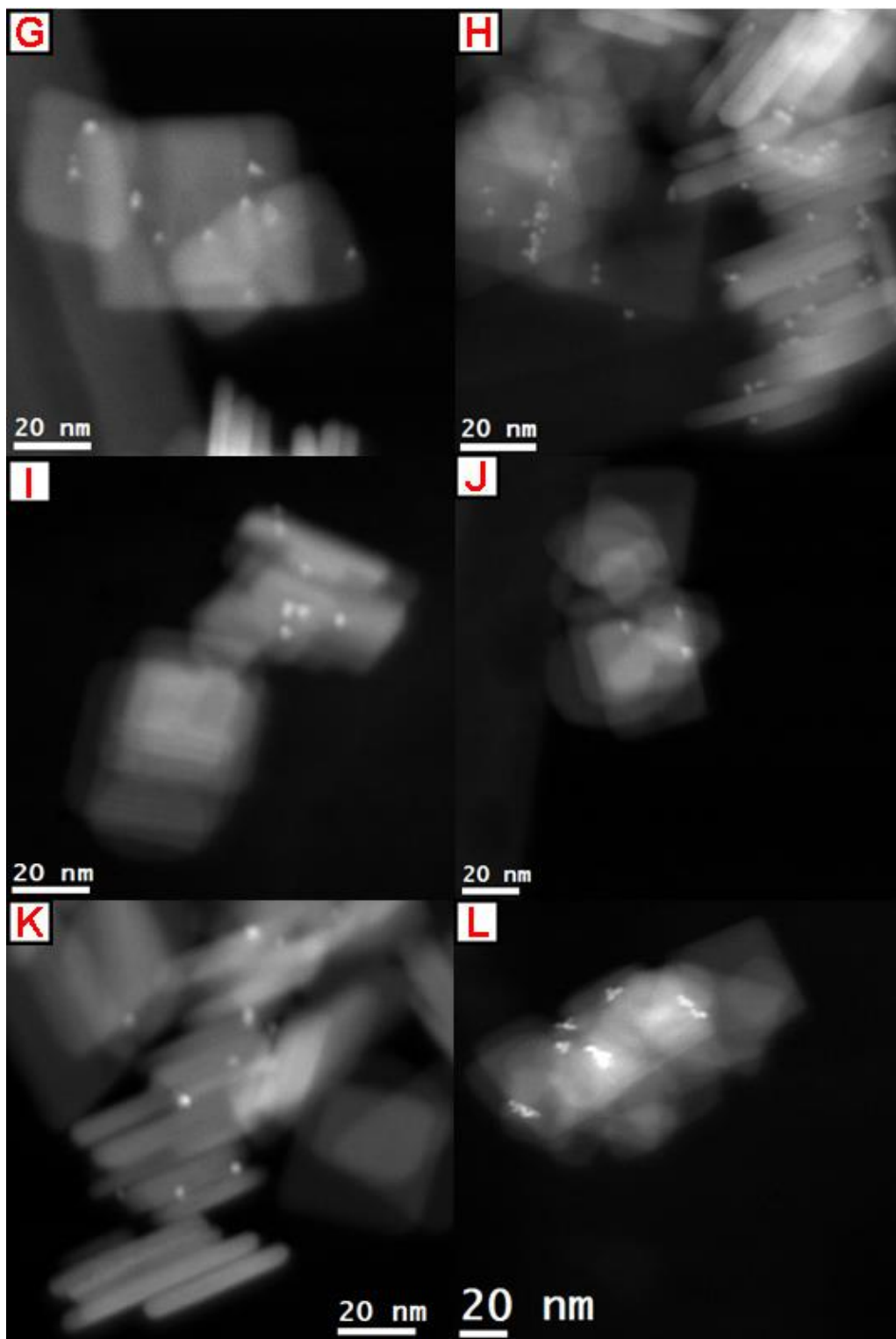


Fig. 4.20. (CONTINUATION) HAADF images for the two series of doped (0.75 wt% and 1.5 wt% of metal doped) for each transition metal used as a dopant with 0.2 wt% of Pt as co-catalyst. G)0.75Cu-TiO₂-NaOH H)1.5Cu-TiO₂-NaOH I)0.75Fe-TiO₂-NaOH J)1.5Fe-TiO₂-NaOH K) TiO₂-NaOH L) TiO₂-NaOH

The distribution of the Pt nanoparticles is not homogeneous and there are some agglomerates on the TiO₂ nanosheets studied. The size of the single Pt nanoparticles is around 2-4 nm, but the average size of the Pt agglomerates is different from the average size of single Pt-NPs. A possible explanation for this nanoparticle distribution over the TiO₂ nanosheets could be the innate nature of the nanosheets morphology that causes non-homogeneous photodeposition of Pt nanoparticles onto the nanosheets surface due to electronic repulsion related to the location of the active sites on the surface of the photocatalyst. The size distributions for Pt NPs photodeposited over the different samples are presented in Figure 4.21.

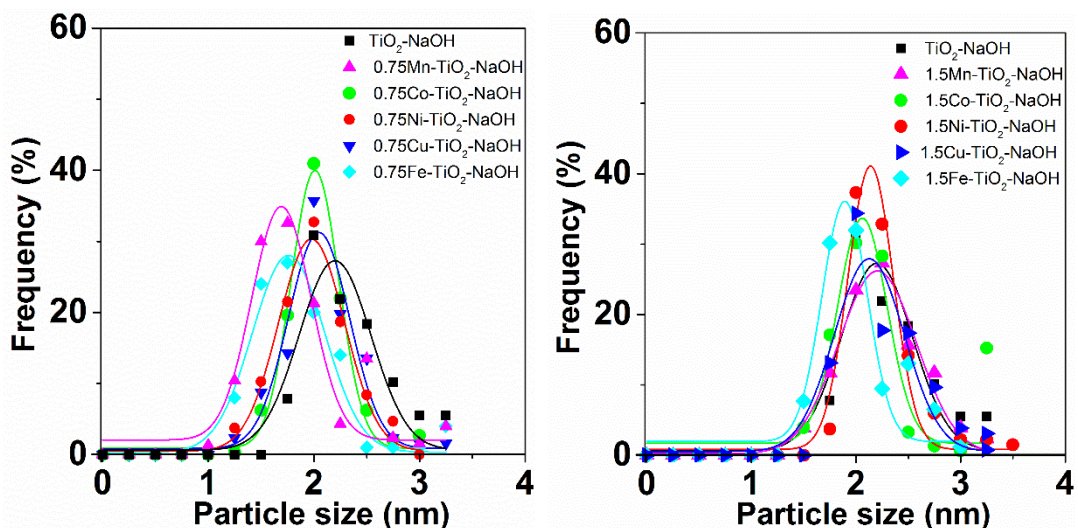


Fig. 4.21 Pt NPs size distributions histograms for undoped and doped TiO₂ nanosheets.

4.8 H₂ production from aqueous ethanol solution under solar simulated light.

Photocatalytic H₂ production experiments were performed sing the apparatus previously desrcied in detail in Chapter 2 “Methodology”. Briefly, 50 mg of dried TiO₂ powder was suspended in EtOH 96% (80 mL) and 20 µL of an aqueous solution of Pt(NO₃)₂ (5 mg Pt mL⁻¹) was added in order to obtain a final metal loading of 0.2 wt.%. The suspension was purged with an Ar flow and

irradiated with a Lot-Oriel Solar Simulator, equipped with a 150W Xe lamp and an Atmospheric Edge Filter with a cut-off at 300 nm. The intensity of the irradiation was 200 mW cm⁻², which is equivalent to 2 Suns.

The photocatalytic experiments evidenced that H₂ is produced mainly from dehydrogenation of ethanol, that is thermodynamically more favourable than water splitting. The aim of this experiment was to determine the effect on H₂ production of the presence of F⁻ ions on the surface of the TiO₂ nanosheets, how transition metals influence the photocatalytic activity, and additionally, the effect of their amount.

Generally speaking, H₂ production began immediately after switching on of the light source and a progressive increase in its production rate was observed during the initial 1 – 2 hours. This effect is mainly due to the activation of the photocatalysts by deposition of the Pt nanoparticles. After the initial activation, a progressive decrease in the H₂ production rate is observed. This deactivation has a different extent depending on the dopant metal.

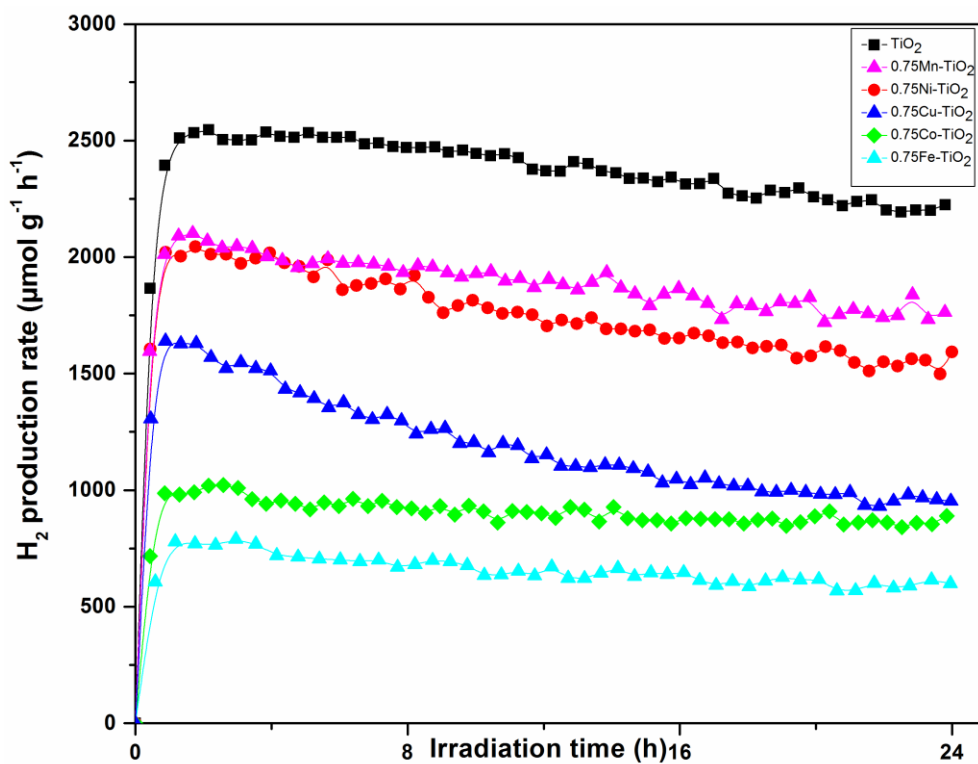


Fig. 4.22 Photocatalytic H₂ production from EtOH/H₂O solutions using **0.75M-TiO₂** samples.

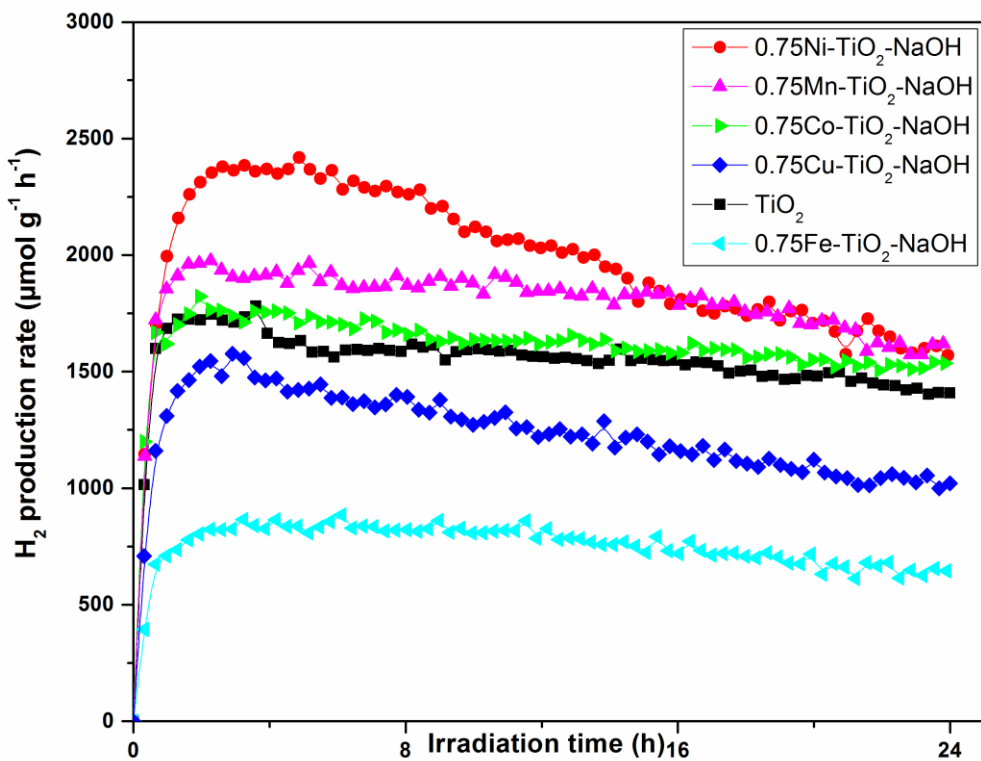


Fig. 4.23: Photocatalytic H₂ production from EtOH/H₂O solutions using **0.75M-TiO₂-NaOH** samples.

The comparison of the results presented in Figure 4.22 for the **0.75M-TiO₂** samples and in Figure 4.23 for the **0.75M-TiO₂-NaOH** samples allows to draw two conclusions. The first involves the undeniable influence of the F⁻ ions on the photocatalytic activity of the samples, and the second is the way transition metals influence the photocatalytic activity in combination or in the absence of F⁻ on TiO₂ nanosheet surface. In the literature, there are differences of opinion regarding the influence of F⁻ ions on this type of titania nanostructures. Some authors agree that fluoride negatively influences the photocatalytic activity of this type of sample^(30,31) as well as the fact that it acts as a poison for the Pt when this is present as a co-catalyst⁽³²⁾. In contrast, there are several studies in which F⁻ ions exert a positive effect on the photocatalytic activity of this type of sample^(17,33-37). In this work of thesis, the effect of the F⁻ ions depends on the chemical environment, as seen in the XPS analysis. In Figure 4.22 (fluorine samples), the undoped TiO₂ sample (black line) has a higher photocatalytic activity in comparison with the fluorine **0.75M-TiO₂**. For the samples with transition metals as dopants, the highest activity is, in ascending order:

undoped>0.75Mn-TiO₂>0.75Ni-TiO₂>0.75Cu-TiO₂>0.75Co-TiO₂>0.75Fe-TiO₂

In order to gain a better grasp on obtained results, it must be considered that the BET surface area and the value for the Eg are similar for all the samples in this series. In the particular case of 0.75Fe-TiO₂ the value for the Eg is the lowest of all the series but in contrast it has the lowest photocatalytic activity of all the samples. The photocatalytic activity cannot be explained only by physical properties in this case and must be due to the electronic structure. In the particular case of the undoped-TiO₂ nanosheets (black line), the F⁻ ion has a positive effect on the photocatalytic activity for H₂ production. In Figure 4.23, the photocatalytic activity for the undoped-TiO₂ decreases when the F⁻ ions are reduced. This confirms the fact that in absence of transition metals the F⁻ ions increase photocatalytic activity. In this same figure, which corresponds to the sample washed with NaOH to reduce the F⁻ ions on the surface, the photocatalytic activity is, in ascending order:

0.75Ni-TiO₂>0.75Mn-TiO₂>0.75Co-TiO₂>undoped >0.75Cu-TiO₂>0.75Fe-TiO₂

From these results, it can be deduced that the photoactivity of the doped samples increases when there are less fluorine ions on the surface of the titania nanosheets. If we compare the results in Figure 4.22(surface-fluorinated anatase TiO₂ nanosheets) with those in Figure 4.23 (low fluorine samples), the samples doped with Mn, Ni and, especially, the Co-doped sample have significantly better photocatalytic activity in the absence of F⁻ ions. The photoactivity of the sample doped with Cu and Fe does not vary greatly with/without fluorine, and in the case of the undoped sample, photocatalytic activity decreases significantly when F⁻ ions are removed from the surface. Our photocatalytic activity experiments demonstrated that the photoactivity of fluorine-metal-doped TiO₂ was inferior to that of fluorine undoped-TiO₂. It is clear, therefore, that there is a detrimental electronic interaction between the F⁻ ions and transition metals.

The undoped-F-TiO₂ nanosheets have more activity due to the fluorination of the surface. The surface bulk-Ti-F of the nanosheets reduces the recombination rate of the photo-generated electrons and holes, because the fluorinated samples act as electron trapping sites that hold the photo-generated

electrons⁽¹⁰⁾ due to the strong electronegativity of the fluorine. The presence of F⁻ ions on the surface of TiO₂ nanosheets results in a reduced recombination rate of electron-hole pairs, enhancing photocatalytic activity. The relevant literature also contains examples where the formation rates of free OH radicals on F-TiO₂ are much greater than surface-bound OH radicals on pure TiO₂⁽³⁶⁾. It is well known that the free OH radicals have a stronger oxidation ability and this improves the photocatalytic activity^(1,10,34,38–40). As verified experimentally, for the undoped sample, the photocatalytic activity decreased significantly when F⁻ ions were removed from the surface by the washing process described previously. It is obvious that the F⁻ ions play a key role in the photocatalytic activity of the undoped-TiO₂ nanosheets.

In the case of the transition metal doped TiO₂ nanosheets, as observed in the photocatalytic experiments, for 0.75Mn-TiO₂, 0.75Ni-TiO₂, 0.75Co-TiO₂ the presence of F⁻ ions has a detrimental effect. In the case of 0.75Cu-TiO₂ the effect of F⁻ ions is slightly positive, and for 0.75Fe-TiO₂ no influence of any type was detected. This last sample also presents the lowest photocatalytic activity. Considering these results, it is clear that the type of doping ion directly influences the electronic state of the doped TiO₂ nanosheets. For Mn-, Ni- and Co-TiO₂ nanosheets with low amounts of F⁻ ions, the charge transportation and separation rate is higher than for Cu and Fe doped samples. The electrons in these last two materials must be localized around the dopant, but the electrons from the Mn, Ni and Co dopant are delocalized^(41,42). This may explain why these samples exhibit higher photoactivity than the other samples when low amounts of F⁻ ions are present. The reason the Mn, Ni and Co samples increase their photocatalytic activity when the F⁻ ions are reduced from the titania nanosheet surface is the electronic interaction F-M. In the present case, the F-M combination favours the electron-hole recombination and this synergistic effect is detrimental to photocatalytic H₂ production, as seen in the experiments results.

Figure 4.24 presents the photocatalytic activity of unwashed 1.5M-TiO₂ nanosheets while Figure 4.25 shows the photocatalytic activity for 1.5M-TiO₂ nanosheets washed four times with NaOH.

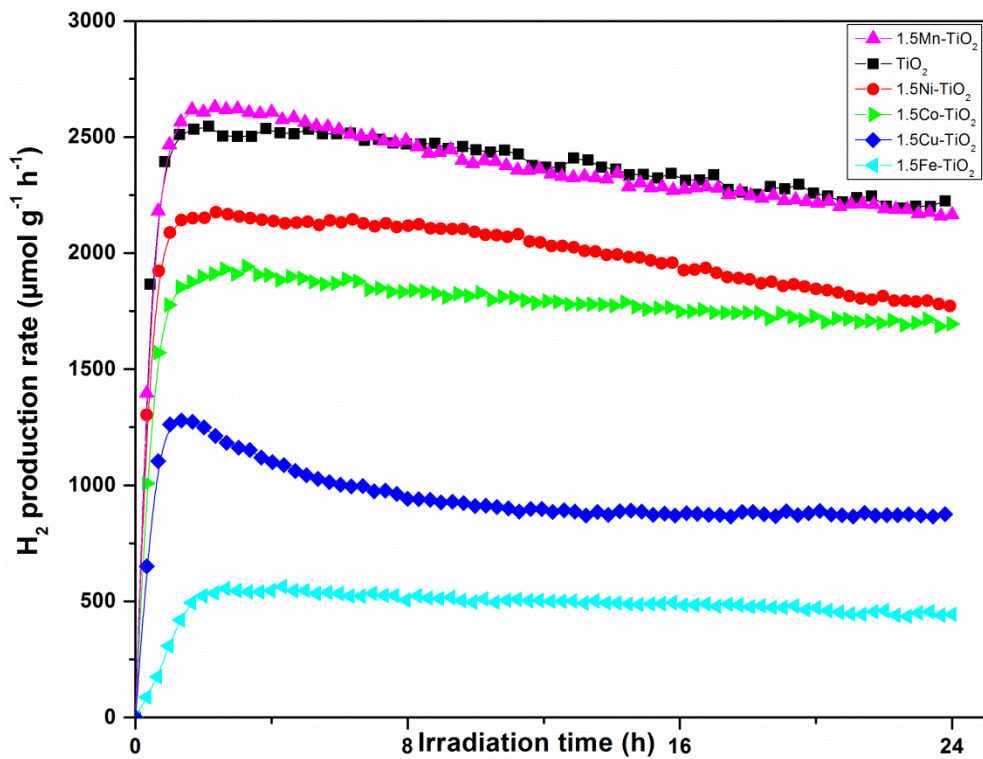


Fig. 4.24 Photocatalytic H₂ production from EtOH/H₂O solutions using 1.5M-TiO₂ samples.

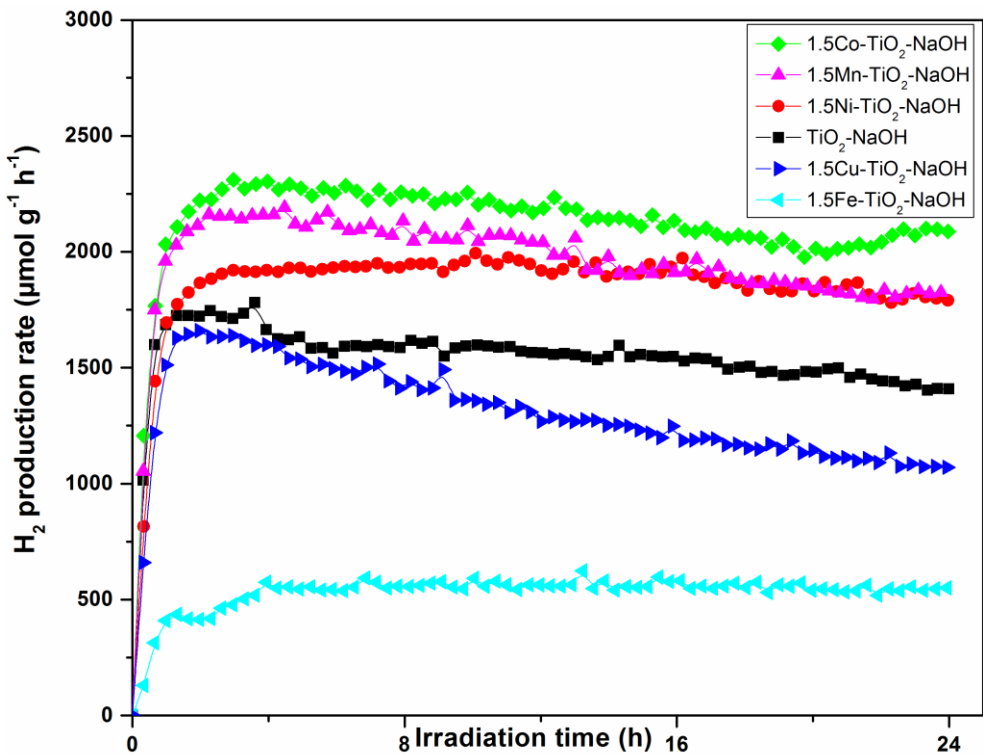
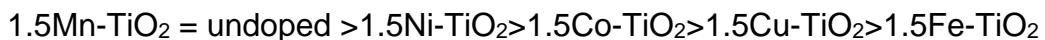


Fig. 4.25 Photocatalytic H₂ production from EtOH/H₂O solutions using 1.5M-TiO₂-NaOH samples.

Figure 4.24 presents the H₂ production under solar simulated light for the well-faceted TiO₂ nanosheets in which the amount of dopants has been increased to 1.5 wt%. The graph in Figure 4.24 shows that for fluoridated samples, the 1.5Mn-TiO₂ sample has the same H₂ production as the fluorine undoped TiO₂ samples and, furthermore, the production is higher than for the fluorine doped 0.75Mn-TiO₂ sample (Figure 4.22). In the case of the Co-doped sample the activity also is increased in the sample with more dopant (Figure 4.22). For the Ni-doped sample the photoactivity is slightly higher but for the Cu- and Fe-doped samples the photocatalytic activity decreases. In this case the photocatalytic activity in ascending order is:

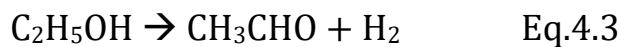


Analysing the results, we can see that as the amount of Fe and Cu dopant is increased, photocatalytic H₂ production decreases compared with the samples that contain less of these dopants. In this sense, the Fe and Cu has a detrimental effect on photoactivity in our system. In contrast, increasing Mn, Co and Ni has a positive effect, particularly in the case of Mn and Co. Analysing the graph in Figure 4.25, in which the samples were washed to reduce the amount of F⁻ ions, it is possible to see that for the Co-doped sample the photocatalytic activity increases significantly with respect to the fluoridated Co sample. This result is slightly better than the photocatalytic activity of the 0.75 Co-TiO₂ shown in Figure 4.23; thus, increasing the amount of Co has a positive effect on the photocatalytic activity. In Figure 4.25 it is also possible to observe that for the non-fluoridated sample of Cu the photocatalytic activity is slightly improved with respect to the fluoridated sample shown in Figure 4.24. The most striking result is for the non-fluoridated samples of Mn and Ni, which slightly decrease their photocatalytic activity with respect to the fluoridated samples in Figure 4.24. This result is contrary to those obtained for the samples with 0.75 wt% Mn and Ni.

As the metal cations act as trapping sites, they can influence the lifetime of charge carriers. The inhibitory effect is ascribed to a higher rate of electron-hole recombination as a result of increasing the concentration of conduction electrons. In our case, Fe and Cu behave as electron/hole recombination

centres and decrease the photoactivity of the TiO₂ nanosheets. In the case of Mn, Co and Ni, as seen for the 0.75M-TiO₂ samples, the photoactivity increases as they act as electron traps, decreasing electron-hole recombination. In this sense when the amount of these dopants is increased, the photoactivity also increases.

The following chemical reactions show the transformation of the EtOH. The dehydrogenation of the EtOH take places with the oxidation of the ethanol to acetaldehyde upon irradiation. Because to the low adsorption capability of acetaldehyde and to the high concentration of ethanol, subsequent oxidation of acetaldehyde is highly unfavourable.



The solution collected after photocatalytic experiments were analysed to detect by-products accumulated within them. The results of semi-quantitative analysis are presented in Table 4.10.

These data are in very good agreement with the H₂ production observed during the photocatalytic experiments. Obviously, the highest amounts of acetaldehyde and 1,1-diethoxyethane were detected in the liquid phases when more H₂ is produced during the photocatalytic experiment.

Table 4.10. Amount of acetaldehyde and 1,1-diethoxyethane present in the liquid phase after photocatalytic experiments.

Fluorinated samples	Acetaldehyde (a.u.)	1,1-diethoxyethane (a.u.)
0.75Mn-TiO ₂	0.28	10.11
0.75Ni-TiO ₂	0.24	8.30
0.75Co-TiO ₂	0.13	4.71
0.75Cu-TiO ₂	0.16	5.53
0.75Fe-TiO ₂	0.11	3.36
undoped	0.40	15.07
1.5Mn-TiO ₂	0.34	11.67
1.5Ni-TiO ₂	0.23	9.84
1.5Co-TiO ₂	0.25	9.27
1.5Cu-TiO ₂	0.13	4.93
1.5Fe-TiO ₂	0.08	2.67
Samples with low quantities of F⁻ ions on their surface after washing	Acetaldehyde (a.u.)	1,1-diethoxyethane (a.u.)
0.75Mn-TiO ₂	0.25	8.55
0.75Ni-TiO ₂	1.22	0.24
0.75Co-TiO ₂	0.21	7.47
0.75Cu-TiO ₂	0.16	5.66
0.75Fe-TiO ₂	0.12	3.81
undoped	0.21	7.26
1.5Mn-TiO ₂	0.23	7.95
1.5Ni-TiO ₂	0.23	8.22
1.5Co-TiO ₂	1.25	0.36
1.5Cu-TiO ₂	0.17	5.98
1.5Fe-TiO ₂	0.07	2.45

4.10 Conclusions

This experimental work reports a solvothermal synthesis route for morphology-controlled preparation of uniform and highly crystalline TiO₂ anatase nanosheets in which 2-propanol acts as a capping agent together with HF. The TiO₂ materials were doped with a series of transition metals and the photocatalytic activity was evaluated under simulated solar light irradiation in order to produce H₂ from ethanol dehydrogenation. Characterization using XRD, BET, TEM, HAADF, ICP, XPS and XRF has provided valuable information on the morphology of the TiO₂ nanomaterials and the modifications to their surfaces after washing that enables us to explain the photocatalytic results. The metal ions promote adsorption and improve the photocatalytic activity of doped TiO₂ nanosheets under irradiated solar light. Some doped metals (Mn, Ni and Co) appear to enhance the photocatalytic production of H₂ through the ethanol dehydrogenation reaction. It was seen that Fe has a detrimental effect on photocatalytic activity, even when it is present in low amounts in the photocatalyst.

The influence of the F⁻ ions adsorbed onto the surface during the synthesis of the nanomaterials has an undeniable effect on photocatalytic activity as demonstrated in this work. It has been seen that there are significant differences in photocatalytic activity between fluoridated samples and non-fluoridated samples. In the absences of doped metal, the photocatalytic activity is favoured by the presence of F⁻ ions on the photocatalytic surface. In contrast, when the photocatalysts are doped with transition metals, the presence of F⁻ ions negatively affects the photocatalytic activity.

Further work will be necessary to find a more effective doping method in order to increase the amount of metal doped into the samples. To this end, it could be interesting to test the TiO₂ nanomaterial samples with other transition metals in order to clarify the best doped system for the photocatalytic production of H₂.

References

1. Yang HG, Sun CH, Qiao SZ, Zou J, Liu G, Smith SC, et al. Anatase TiO₂ single crystals with a large percentage of reactive facets. *Nature*. 2008 May 29;453(7195):638–41.
2. Yang HG, Liu G, Qiao SZ, Sun CH, Jin YG, Smith SC, et al. Solvothermal synthesis and photoreactivity of anatase TiO₍₂₎ nanosheets with dominant {001} facets. *J Am Chem Soc. American Chemical Society*; 2009 Mar 25;131(11):4078–83.
3. Gordon TR, Cagnello M, Paik T, Mangolini F, Weber RT, Fornasiero P, et al. Nonaqueous synthesis of TiO₂ nanocrystals using TiF₄ to engineer morphology, oxygen vacancy concentration, and photocatalytic activity. *J Am Chem Soc*. 2012 Apr 18;134(15):6751–61.
4. Chu L, Qin Z, Yang J, Li X. Anatase TiO₂ Nanoparticles with Exposed {001} Facets for Efficient Dye-Sensitized Solar Cells. *Sci Rep. Nature Publishing Group*; 2015;5:12143.
5. Ong W-J, Tan L-L, Chai S-P, Yong S-T, Mohamed AR. Highly reactive {001} facets of TiO₂-based composites: synthesis, formation mechanism and characterization. *Nanoscale*. 2014 Mar 21;6(4):1946–2008.
6. Han X, Kuang Q, Jin M, Xie Z, Zheng L. Synthesis of titania nanosheets with a high percentage of exposed (001) facets and related photocatalytic properties. *J Am Chem Soc*. 2009 Mar 11;131(9):3152–3.
7. Grabowska E, Diak M, Marchelek M, Zaleska A. Decahedral TiO₂ with exposed facets: Synthesis, properties, photoactivity and applications. *Appl Catal B Environ*. Elsevier; 2014 Sep;156–157:213–35.
8. Luan Y, Jing L, Xie Y, Sun X, Feng Y, Fu H. Exceptional photocatalytic activity of 001-facet-exposed TiO₂ mainly depending on enhanced adsorbed oxygen by residual hydrogen fluoride. *ACS Catal*. 2013;3(6):1378–85.

9. Diebold U. The surface science of titanium dioxide. *Surf Sci Rep.* 2003;48(5):53–229.
10. Xiang Q, Lv K, Yu J. Pivotal role of fluorine in enhanced photocatalytic activity of anatase TiO₂ nanosheets with dominant (001) facets for the photocatalytic degradation of acetone in air. *Appl Catal B Environ.* 2010;96(3–4):557–64.
11. Lai Z, Peng F, Wang Y, Wang H, Yu H, Liu P, et al. Low temperature solvothermal synthesis of anatase TiO₂ single crystals with wholly {100} and {001} faceted surfaces. *J Mater Chem. The Royal Society of Chemistry;* 2012;22(45):23906.
12. Shannon RD. Revised effective ionic radii and systematic studies of interatomic distances in halides and chalcogenides. *Acta Crystallogr Sect A.* 1976;32(5):751–67.
13. Sun L, Zhai J, Li H, Zhao Y, Yang H, Yu H. Study of homologous elements: Fe, Co, and Ni dopant effects on the photoreactivity of TiO₂ nanosheets. *ChemCatChem.* 2014;6(1):339–47.
14. Liu M, Li H, Zeng Y, Huang T. Anatase TiO₂ single crystals with dominant {001} facets: Facile fabrication from Ti powders and enhanced photocatalytical activity. *Appl Surf Sci. Elsevier B.V.*; 2013 Jun;274:117–23.
15. Biyoghe L, Ndong B, Ibondou MP, Gu X, Lu S, Qiu Z, et al. Enhanced Photocatalytic Activity of TiO₂ Nanosheets by Doping with Cu for Chlorinated Solvent Pollutants Degradation. 2014;
16. Tay Q, Liu X, Tang Y, Jiang Z, Sum TC, Chen Z. Enhanced Photocatalytic Hydrogen Production with Synergistic Two-Phase Anatase/Brookite TiO₂ Nanostructures. *J Phys Chem C.* 2013 Jul 25;117(29):14973–82.
17. Dozzi M, Selli E. Specific Facets-Dominated Anatase TiO₂: Fluorine-Mediated Synthesis and Photoactivity. *Catalysts. MDPI AG*; 2013 May 16;3(2):455–85.

18. Sajan CP, Wageh S, Al-ghamdi AA, Yu J. TiO₂ nanosheets with exposed { 001 } facets for photocatalytic application. 2015;
19. Thommes M, Kaneko K, Neimark A V., Olivier JP, Rodriguez-Reinoso F, Rouquerol J, et al. Physisorption of gases, with special reference to the evaluation of surface area and pore size distribution (IUPAC Technical Report). Pure Appl Chem. 2015;0(0):1051–69.
20. Calatayud DG, Rodríguez M, Jardiel T. Controlling the morphology of TiO₂ nanocrystals with different capping agents. Boletín la Soc Española Cerámica y Vídr. SECV; 2015;54(4):159–65.
21. Ma Y, Chong R, Zhang F, Xu Q, Shen S, Han H, et al. Synergetic effect of dual cocatalysts in photocatalytic H₂ production on Pd–IrO_x/TiO₂: a new insight into dual cocatalyst location. Phys Chem Chem Phys. Royal Society of Chemistry; 2014 Jul 8;16(33):17734.
22. Sun L, Zhai J, Li H, Zhao Y, Yang H, Yu H. Study of Homologous Elements: Fe, Co, and Ni Dopant Effects on the Photoreactivity of TiO₂ Nanosheets. ChemCatChem. 2014 Jan 24;6(1):339–47.
23. Ma X, Dai Y, Lu J, Guo M, Huang B. Tuning of the surface-exposing and photocatalytic activity for AgX (X = Cl and Br): A theoretical study. J Phys Chem C. 2012;116(36):19372–8.
24. Liu G, Wang L, Yang HG, Cheng H-M, (Max) Lu GQ. Titania-based photocatalysts—crystal growth, doping and heterostructuring. J Mater Chem. 2010;20(5):831–43.
25. Tandon SP, Gupta JP. Measurement of forbidden energy gap of semiconductors by diffuse reflectance technique. Phys Status Solidi. 1970. p. 363–7.
26. Tauc J Phy. stat. sol. 15, 627 (1966).pdf.
27. Xu G-R, Wang J-N, Li C-J. Template directed preparation of TiO₂ nanomaterials with tunable morphologies and their photocatalytic activity research. Appl Surf Sci. Elsevier B.V.; 2013 Aug;279:103–8.

28. Liu G, Sun C, C. Smith S, Wang L, Lu GQ (Max), Cheng H-M. Sulfur doped anatase TiO₂ single crystals with a high percentage of {001} facets. *J Colloid Interface Sci.* 2010 Sep;349(2):477–83.
29. Tseng I-H, Chang W-C, Wu JCS. Photoreduction of CO₂ using sol-gel derived titania and titania-supported copper catalysts. *Appl Catal B Environ.* 2002 Apr;37(1):37–48.
30. Vohra MS, Kim S, Choi W. Effects of surface fluorination of TiO₂ on the photocatalytic degradation of tetramethylammonium. *J Photochem Photobiol A Chem.* 2003;160(1–2):55–60.
31. Lv K, Lu CS. Different Effects of Fluoride Surface Modification on the Photocatalytic Oxidation of Phenol in Anatase and Rutile TiO₂ Suspensions. *Chem Eng Technol.* 2008;31(9):1272–6.
32. Nie L, Zhou P, Yu J, Jaroniec M. Deactivation and regeneration of Pt/TiO₂ nanosheet-type catalysts with exposed (0 0 1) facets for room temperature oxidation of formaldehyde. *J Mol Catal A Chem.* Elsevier B.V.; 2014;390:7–13.
33. Fittipaldi M, Gombac V, Gasparotto A, Deiana C, Adami G, Barreca D, et al. Synergistic role of B and F dopants in promoting the photocatalytic activity of rutile TiO₂. *Chemphyschem.* 2011 Aug 22;12(12):2221–4.
34. Liu S, Yu J, Jaroniec M. Anatase TiO₂ with Dominant High-Energy { 001 } Facets : Synthesis , Properties , and Applications. 2011;4085–93.
35. Zheng Y, Lv K, Wang Z, Deng K, Li M. Microwave-assisted rapid synthesis of anatase TiO₂ nanocrystals with exposed {001} facets. *J Mol Catal A Chem.* Elsevier B.V.; 2012 Apr;356:137–43.
36. Mrowetz M, Sell E. Enhanced photocatalytic formation of hydroxyl radicals on fluorinated TiO₂. *Phys Chem Chem Phys.* 2005;7:1100–2.
37. Kim J, Choi W, Park H. Effects of TiO₂ surface fluorination on photocatalytic degradation of methylene blue and humic acid. *Res Chem Intermed.* 2010;36(2):127–40.

38. Monllor-Satoca D, Gómez R, González-Hidalgo M, Salvador P. The “Direct-Indirect” model: An alternative kinetic approach in heterogeneous photocatalysis based on the degree of interaction of dissolved pollutant species with the semiconductor surface. *Catal Today.* 2007;129(1–2 SPEC. ISS.):247–55.
39. Kim J, Monllor-Satoca D, Choi W. Simultaneous production of hydrogen with the degradation of organic pollutants using TiO₂ photocatalyst modified with dual surface components. *Energy Environ Sci.* 2012;5(6):7647.
40. Nakata K, Fujishima A. TiO₂ photocatalysis: Design and applications. *J Photochem Photobiol C Photochem Rev.* 2012;13(3):169–89.
41. Chen X, Mao SS. Titanium dioxide nanomaterials: synthesis, properties, modifications, and applications. *Chem Rev.* 2007 Jul;107(7):2891–959.
42. Umebayashi T, Yamaki T, Itoh H, Asai K. Analysis of electronic structures of 3d transition metal-doped TiO₂ based on band calculations. *J Phys Chem Solids.* 2002 Oct;63(10):1909–20.



TiO₂ nanosheets as a self-cleaning building materials

5. TiO₂ nanosheets as a self-cleaning building material

As it was discussed in the introduction, the interest in developing self-cleaning protective materials has dramatically grown in recent times due to the severe effects of air pollution on building deterioration. In this chapter, we will discuss the potential use of TiO₂ nanosheets as a component of nanocomposites with active photocatalytic self-cleaning properties. The effect of the synthesis procedure on the microstructure of the nanocomposite will be studied by TEM and related techniques. Special attention will be paid to determinate the distribution of the titania nanoparticles in the silica matrix. Self-cleaning tests were carried using limonite stone as a reference building material. Main part of the work was focused on determining the influence on the catalytic activity of the presence of F⁻ ions on the pre-synthesized TiO₂ nanosheets. Our results clearly demonstrate the advantages of using TiO₂ nanosheets as active photocatalyst in TiO₂-SiO₂ based nanocomposites.

5.1 Synthesis of TiO₂-SiO₂ nanocomposites

TiO₂ nanoparticles have been widely used to produce photoactive surfaces on a great variety of building materials, such as glass⁽¹⁾, ceramics⁽²⁾ roof tiles⁽³⁾ and especially in stones⁽⁴⁻⁸⁾. The most commonly used method consists on treating the surface with a suspension of TiO₂ in a solvent (water or volatile organic solvents). This approach leads to effective self-cleaning surface, but, as reported in the literature⁽⁹⁻¹²⁾, they exhibit low stability due to the poor adhesion of the film to building materials. In addition, the dispersion of the TiO₂ nanoparticles is commonly difficult and the accumulation of titania nanoparticles is often observed.

We can find in the literature a number of examples that use siloxanes to immobilize TiO₂ nanoparticles. This approach leads to durable and well-adhered photoactive coatings on concretes^(13,14). More recently, Mosquera et al. have developed a new synthesis based on obtaining a low-viscosity SiO₂ sol containing TiO₂^(10,15,16). This sol can penetrate into the pore structure of the substrates and its in situ gelling produces a crack-free TiO₂-SiO₂ nanocomposite⁽¹⁰⁾ which is firmly adhered to the substrates.

The synthesis used in this study is based in the work of Mosquera et al. and it is summarized in Figure 5.1. The first step consists on mixing TES40 (ethyl silicate) with either 1wt% or 4wt% of the TiO₂ nanoparticles. In this study, titania nanosheets and commercial P25 were used. Subsequently, N-octylamine (C₈H₁₉N) and H₂O were added in proportions of 0.36% v/v and 0.83% v/v, respectively. N-octylamine is used to prevent cracking through the coarsening of the pore structure in the gel network and because it acts as a basic catalyst for the sol-transition inside the pore structure of the rock⁽¹⁷⁾. The solution was kept under vigorous ultrasonic agitation for 10 minutes at 125W. After that, the sols were immediately sprayed onto one of the 5x5 cm faces of a 5x5x2 cm stone block. The samples were kept damp for 1 minute and any sol excess was removed by spraying with air. Finally, the treated stones were dried under laboratory conditions until they achieved a constant weight (commonly 2 weeks). Following this, the samples were weighed to calculate the uptake of products. The dry matter of the sol-gel in the final coated stone was 14.1±1.5 mg. The

weight differences are related with changes on the porosity of each stone block. In order to avoid this experimental problem and to obtain statistical significant results, all the syntheses were assayed in duplicate and tested individually.

The stone selected for evaluating the self-cleaning properties of the TiO₂-SiO₂ nanocomposites was a limestone which is commonly used as building material. This stone presents a homogeneous structure, composed of a micritic matrix of calcite and has an open porosity of around 12%. The white colour of this limestone is ideal for evaluating its colour changes.

The samples were labelled using the following nomenclature:

S%X

where S indicates the presence of SiO₂ sample; % is the percentage of TiO₂ in the nanocomposite; and X is the type of TiO₂: P25, NS and NSNaOH that correspond to Degussa P25, as synthetized nanosheets and washed TiO₂ nanosheets. A detailed description of the synthetic route and the washing method is included in chapter 4.

It should be noted that 100 grams of TES40 will provide, after complete hydrolysis, approximately 41 grams of silica. According to this, the final wt% of TiO₂ in the composite can be easily obtained by multiplying the initial concentration by a factor of 2.5. Therefore, the final content of TiO₂ in the sol-gel composite for the sample with an initial loading of 1 and 4 wt% will be 2.5 and 10 wt%, respectively.

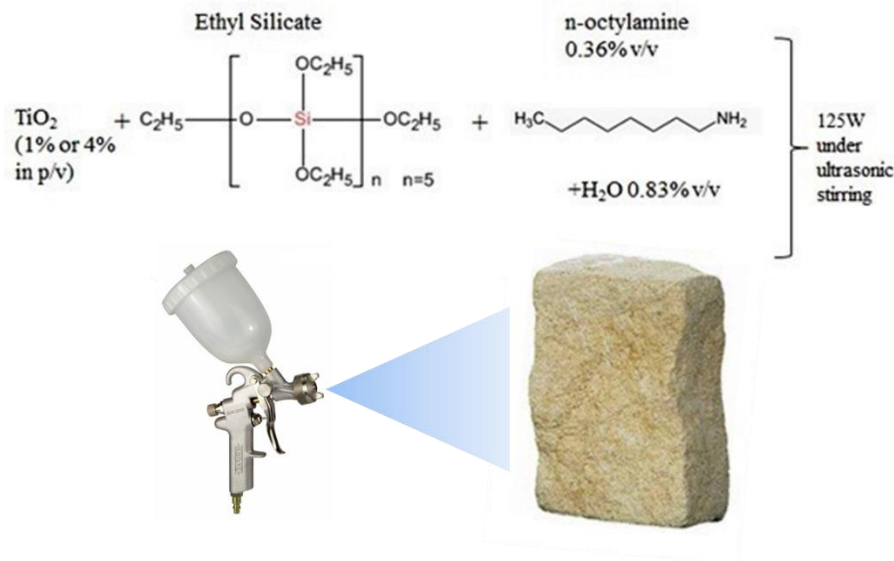


Fig.5.1 Sol gel synthesis pathway of the coated limestone samples.

5.2 Characterization of the sol-gel products

Some visual differences were observed depending on the titania nanoparticles used to obtain the sol. In the case of using P25, homogenous opaque white gels were obtained for all the loadings. The use of as synthesized nanosheets, which contain fluorine on the surface, is more complicate since the TiO_2 nanoparticles are not well dispersed during the synthesis process. These sols were slightly yellow and the nanoparticles of TiO_2 decant very quickly. In this case, the gels were more transparent than those in which the commercial Titania Degussa P25 was used to prepare the $\text{TiO}_2\text{-SiO}_2$ nanocomposite. These problems were not observed when we used washed TiO_2 nanosheets and the TiO_2 nanoparticles were dispersed without any problems and remained stable in the sols. However, these sols were also slightly yellow translucent. The problems on dispersing the as synthesized nanosheets particles can be related to the high content of fluorine in the sample. It is well known that fluorine on TiO_2 surface increase its hydrophobicity, leading to dispersion problems in hydrophilic solutions.

Immediately after the synthesis of the sols, their rheological properties were studied using a concentric cylinder viscometer (model DV-II+ with UL/Y adapter) from Brookfield. Thanks to a circulator, experiments were performed at a constant temperature of 25°C. All the sols showed a nearly Newtonian behaviour in the studied shear range. Thus, the viscosities can be calculated as the slope of shear stress vs. shear rate curves. The viscosity values obtained for the synthesized sols, as well as their gelation time, are presented in table 5.1.

Table 5.1 Viscosity and gelation time results of the sol-gels.

Sample	Viscosity (mPa·s)	Gelation Time (h)
S	4.62	8
S1P25	5.51	7
S4P25	7.17	12
S1NS	5.06	4.5
S4NS	5.57	6
S1NSNaOH	6.02	3.5
S4NSNaOH	6.28	3.5

All viscosity values are below 7.5 mPa·S and similar to those corresponding to commercial silica sols employed for protecting building materials (i.e. Tegovakon V100 from Evonik, one of the most popular commercial stone consolidants, has a viscosity of 5.25 mPa·s at 25°C)⁽¹⁰⁾. This result confirms their suitability to be applied by common procedures, such as spraying, brushing, as coatings of building materials, even under outdoor conditions. The lowest viscosity value corresponds to the sample without titania (S) and it increases by adding titania nanoparticles. Although the differences are small between the obtained sols, we can observe that the viscosity is higher when hydrophilic TiO₂ nanoparticles (P25 and NSNaOH) are used. This can be easily explained if we remember that using as synthesized nanosheets (hydrophobic) leads to flocculation and agglomeration of the titania nanoparticles due to a weak interaction between them and the synthetic solution.

Gelation time is also a key parameter for building materials application, because they must be applied in situ and short gelation times make difficulties to handle the material and inhibit sol penetration into the porous structure of the

substrate. The lowest gelation time was of 3.5 hours and it was observed when NSNaOH was used. This time is long enough to ensure a good distribution of the material. Therefore, all the obtained gels can be used in the catalytic studies. We observe how gelation time decreases by adding 1% of TiO₂. This can be related to the fact that the nanoparticles promote an early nucleation of silica around TiO₂ species⁽¹⁸⁾. In contrast, for the TiO₂-SiO₂ nanocomposite prepared with 4% TiO₂ P25 and NS, the gelation time increased with respect to the samples with 1%. This could be due to the acid nature of the nanoparticles, which would neutralize the catalytic effect of the n-octylamine.

5.3 Textural and chemical Characterization of Xerogels

Due to the unfeasibility of recovering the Xerogels from the treated stones, 3 ml of sols were deposited on plastic Petri dishes with a diameter of 85 mm and maintained at the same laboratory conditions that the treated stones until constant weight. The obtained xerogels were characterized to gain information of the sample porosity, nano-structure and chemical reactivity.

The pore volume (V_p), pore size distribution, and BET surface area of obtained Xerogels were characterized using the nitrogen physisorption technique. Figure 5.2 shows the N₂ physisorption isotherms of the samples analysed and table 5.2 summarize the main results. According to the latest revision of adsorption isotherms carried out by the IUPAC⁽¹⁹⁾, the all the isotherms represented in Figure 5.2 correspond to *Type IV(a)*, characteristic of mesoporous materials. The hysteresis loop is similar to *Type H1* for all the samples, although it is more obvious in the case of the samples containing P25, while the rest of the samples exhibit hysteresis loops closer to *Type H2(b)*. Our results are similar to those previously reported in the literature using P25⁽¹⁵⁾. According to the authors, this kind of hysteresis is attributed to materials consisting of agglomerated particles or compacted clusters of spherical particles arranged in a uniform way. The deviation from *Type H1* to *Type H2(b)* can be associated with pore blocking, but also with a size distribution of neck widths much larger.

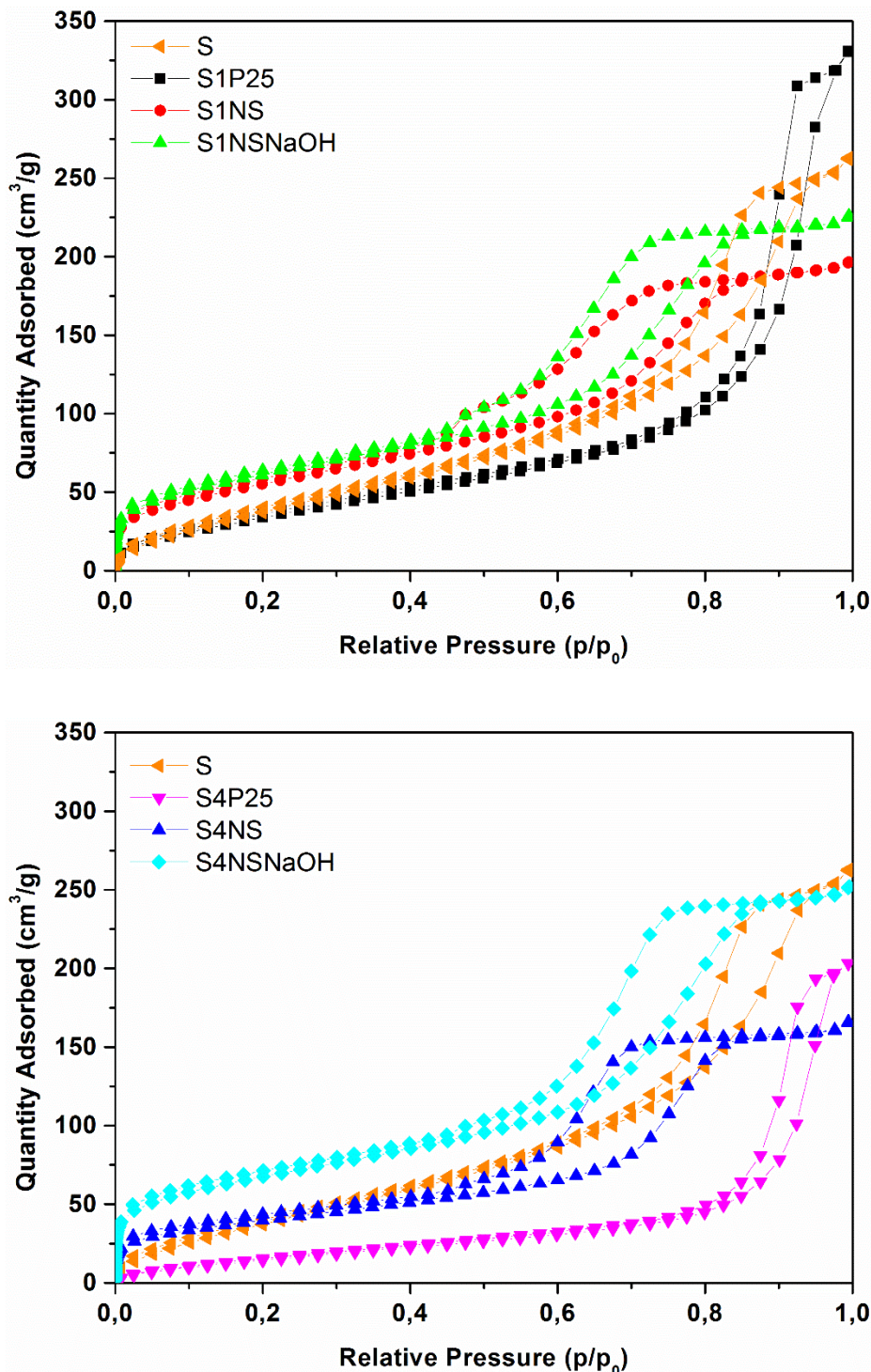


Fig. 5.2 N₂ physisorption curves of the obtained xerogels.

Table 5.2 BET surface area, pore size and pore volume (V_p) of all samples.

Sample	Surface (m ² /g)	V _p (cm ³ /g)	Pore size (nm)
S	150.8	0.560	6.1
S1P25	130.6	0.493	13
S4P25	66.0	0.298	12.8
S1NS	167.9	0.292	7.3
S4NS	139.8	0.237	5.2
S1NSNaOH	201.8	0.337	7.3
S4NSNaOH	235.5	0.363	5.7

The pure silica xerogel exhibited a relatively high surface of 150.8 m²·g⁻¹. The addition of P25 and NS nanoparticles decrease the surface of the final composite, although adding NSNaOH increase its surface. If we compare the BET of the TiO₂-SiO₂ xerogels with their gelation time, we realize that the samples with longer gelation time exhibit lower surface areas and bigger pore size. Therefore, we can consider that, as we previously discussed, the titania nanoparticles actively participate in the xerogel formation and determinate its microstructure. However, it is difficult to correlate the initial BET surface, hydrophobicity and reactivity of the TiO₂ nanoparticles with the SiO₂ formation. According to our results, P25 negatively affect to the growth of the SiO₂ xerogel and lead to slow formation rates and systems with big pores and low surface. This effect is more obvious when we increase the TiO₂ amount and it could be related with the adsorption of n-octylamine on the acid site located on P25. The addition of 1% of as synthetized nanosheets only introduce slightly changes in both BET surface and pore size. This can be related with the weak interaction between the gel matrix and these hydrophobic nanoparticles. Finally, the incorporation of titania nanosheets pre-treated with NaOH decrease the gelation time and increase the specific surface of the final Xerogel. In this case, increasing the amount of titania, enhances the BET surface. This result may be interpreted if we consider that the interaction of these nanoparticles with the synthesis mixture is higher than in the case of the NS and that NSNaOH catalyse the TES40

hydrolysis reducing the gelation time and generating more SiO₂ nucleation centres that leads to smaller particles and higher specific surface.

In order to gain information regarding the microstructure of the xerogels, the samples were intensively characterized by HAADF technique in combination with X-EDS analysis. This approach allows us to obtain composition maps of the different samples and determinate the distribution of the titania nanoparticles in the SiO₂ matrix. Figure 5.3 includes representative HAADF images and the elemental mapping for Ti and Si. The comparison of HAADF images and the elemental mapping demonstrate that there is a mesoporous SiO₂ matrix that surround the TiO₂ nanoparticles. Images corresponding to samples S1NS and S4NS, especially the latter, demonstrate the agglomeration of titania nanosheets embedded in a porous silica matrix. This result is in good concordance with the dispersion problems that was observed during the synthesis of the gels containing as synthesised nanosheets. In contrast, the titania nanosheets are well dispersed after treating them with NaOH to remove the fluorine, which increases the hydrophilicity

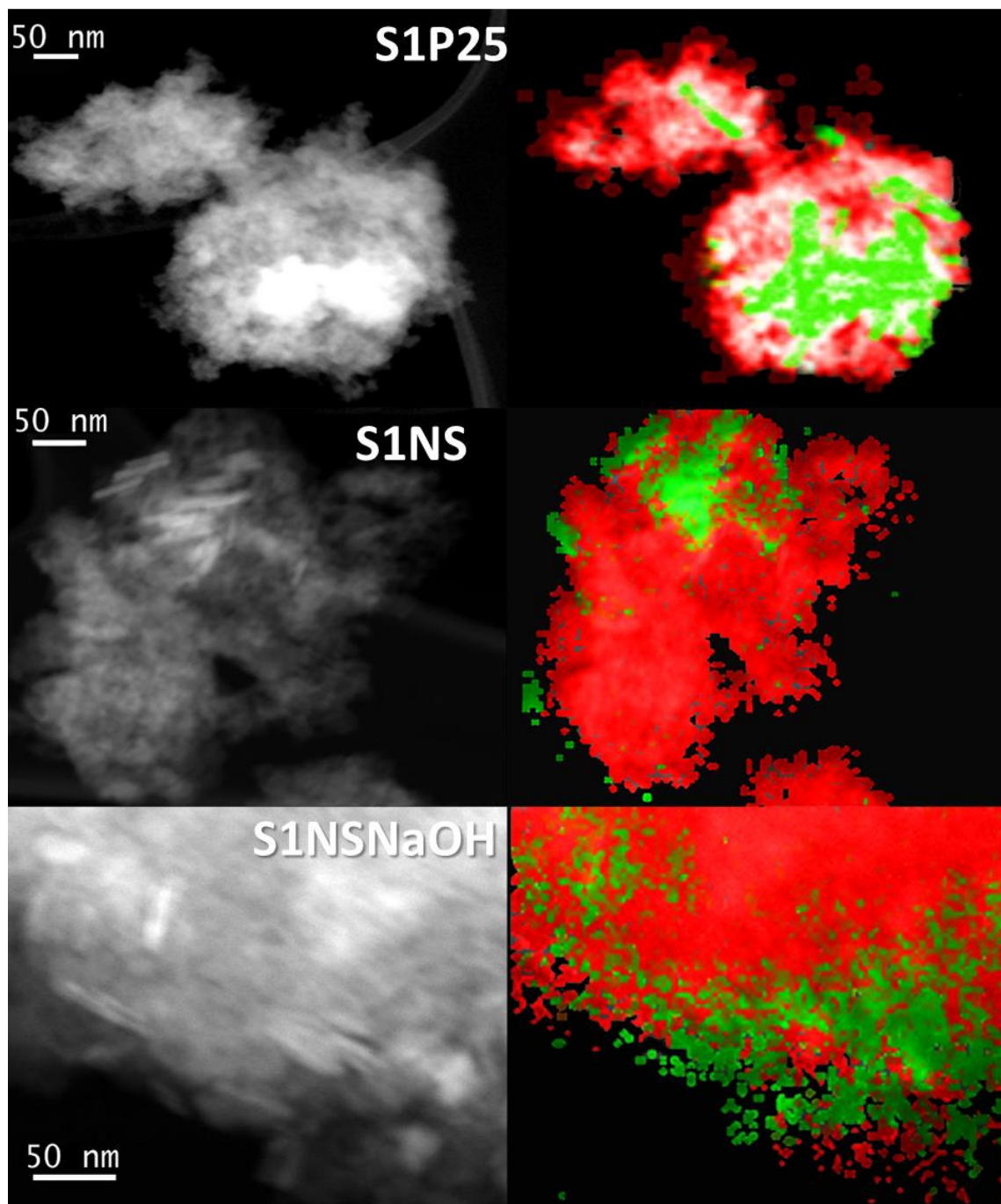


Fig. 5.3 Representative HAADF images (left) and elemental mapping (right) for Ti (green) and Si (red) of samples S1P25 (a), S1NS (b) and S1NSNaOH (c).

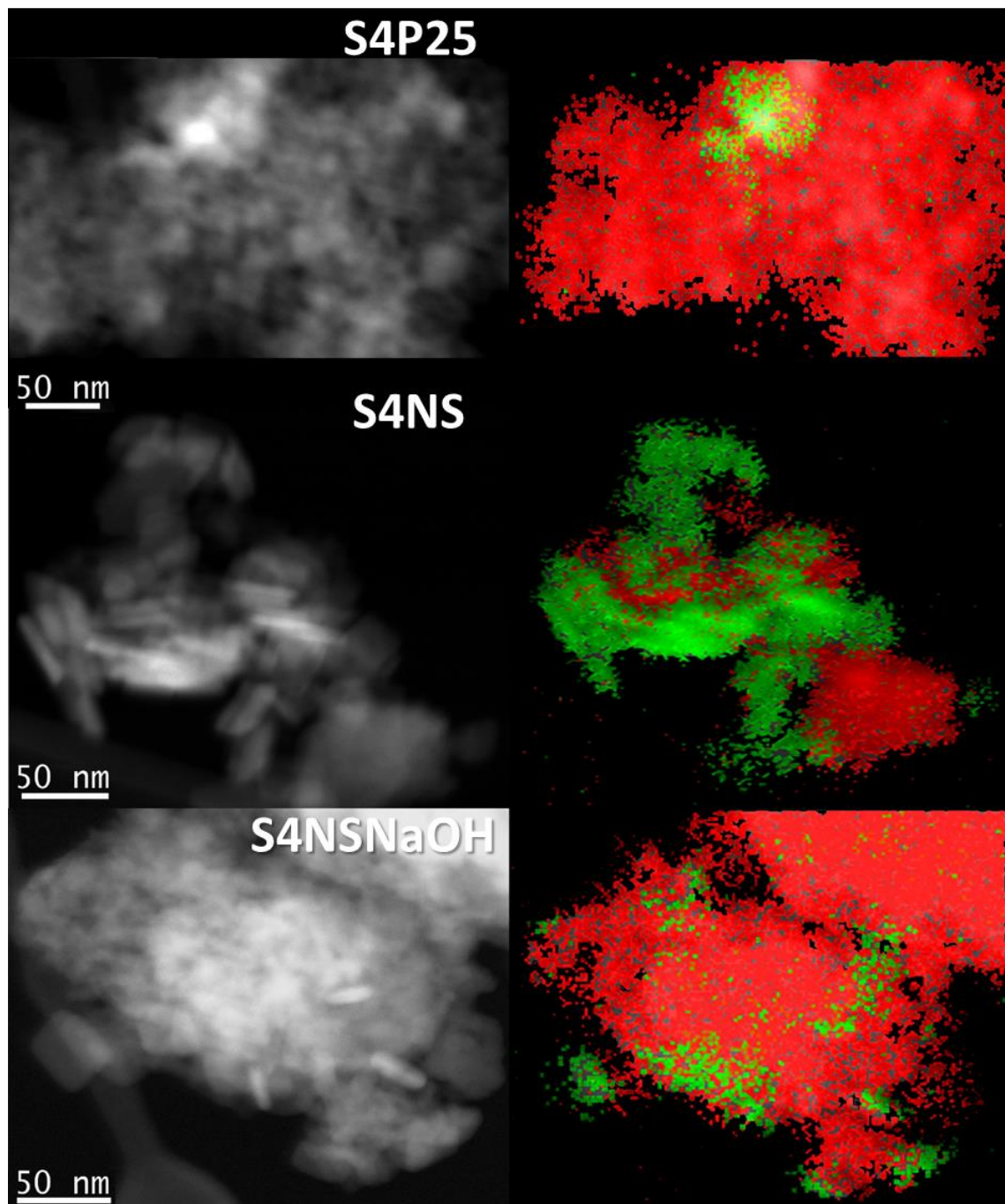


Fig. 5.3 (cont) Representative HAADF images (left) and elemental mapping (right) for Ti (green) and Si (red) of samples S4P25 (a), S4NS (b) and S4NSNaOH (c).

5.4 Evaluation of the photo-induced self-cleaning activity

As we previously describe, the freshly prepared products were sprayed onto one of the biggest faces of a 5x5x2 cm limestone block. In order to evaluate the self-cleaning activity of the coated samples, we carried out methylene blue photo-degradation tests using the experimental procedure describe in section 2.9. Summarizing, 0.25 ml of a 1 mM solution of methylene blue (Panreac) in ethanol was deposited, drop by drop, on the treated faces of the samples. Subsequently, the coated stones were irradiated in a solar degradation chamber, Solarbox 3000eRH, equipped with a 2500 W xenon arc lamp. The conditions in the chamber were 500 W/m² of irradiance, 55 °C of temperature and 60 mg/m³ of absolute humidity. The evolution of colour and diffuse reflection spectra with time were determined by using the previously described spectrophotometer and by acquiring pictures with a 13 MP camera.

Figure 5.4 shows the pictures of the samples during the catalytic test. The included inset of each frame corresponds to a digital reproduction of the average colour of the surface of the rock from the colour coordinates measured by the colorimeter. We should point out that the MB is better dispersed on the untreated stones, probably due to its higher porosity since after the treatment some pores are totally or partially blocked. We observe how no visual changes were observed in the untreated sample during the experiment, while the surface of all the treated samples gradually get discoloured. On the other hand, if we compare the results obtained with pure SiO sol (S) and TiO₂ containing sols, it is also clear the positive effect of adding titania nanoparticles to the sols. It is noteworthy to mention the notable decolouration obtained in the case of the samples treated with S4NS and S4NSNaOH. In those cases, the stone clearly recovered its initial white colour in most part of the surface after 120 minutes. We also can conclude that increasing the titania concentration, the abatement of MB is bigger.

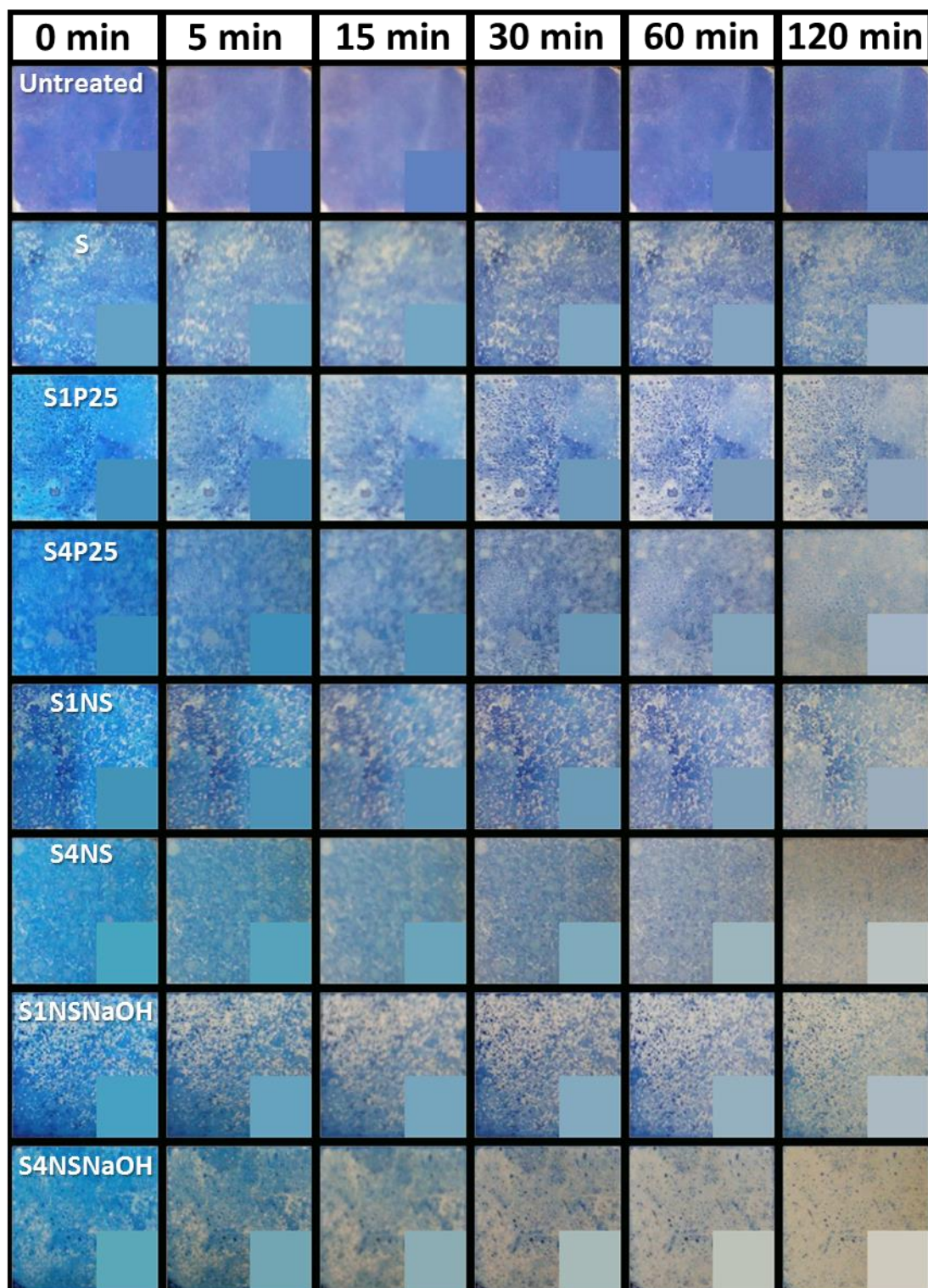


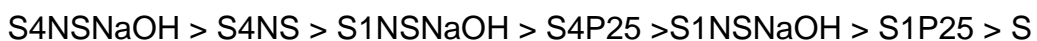
Fig. 5.4 Evolution of MB decolourization by photographs during the first 120 minutes of the photo-degradation test. The insets include the digital reproduction of the stone color from the color coordinates.

In order to obtain quantitative results, the colour and the diffuse reflectance were obtained by using a solid reflection *Colorflex* spectrophotometer from *Hunterlab* (more details can be found in Chapter 2 of this work). The methodology consists on acquiring the reflectance spectra of the samples during the catalytic test and also before starting the experiment and also of the treated stones before MB deposition. The spectra of the sample without MB was subtracted from the spectra of samples with MB. The reflectance spectra were converted into absorption spectra applying the Kubelka-Munk equation that can be used to model the light absorption of a thin layer of dye deposited on a non or low-absorbent substrate:

$$F_{KM}(R) = \frac{(1-R)^2}{2R} \quad Eq. 5.1$$

Where F_{KM}(R) is the Kubelka-Munk function that in our case is equivalent to absorbance and R is the absolute diffuse reflectance.

Figure 5.5 includes the evolution of the absorbance (KM) normalized with respect to the initial absorbance (KM₀), both obtained at highest value of the absorption spectra. This curves allow us to determinate the decay of concentration of MB over time and we can easily compare the activity of the studied samples. We confirm the poor self-cleaning properties of the untreated sample that according to the literature⁽²⁰⁾, can be related with the spontaneous degradation of MB by simple light exposure due to purely photochemical mechanisms. It is also clear that after treating the sample with all the synthetized sols, the MB abatement is greatly improved. In addition, the photocatalytic degradation of MB is clearly enhanced by adding TiO₂ nanoparticles. In fact, the performance of the sols increases by increasing the amount of titania nanoparticles. The observed order in the self-cleaning activity of the products is the following:



If we consider the activity of the samples with the same amount of added titania nanoparticles, we can conclude that titania nanosheets exhibit better photocatalysis activity than the P25. On the other hand, the activity of the as synthetized nanosheets is improved by a pre-treatment with NaOH. The

comparisons of the photocatalytic performance with the specific surface of the xerogels (table 5.2) demonstrate that there is not any obvious correlation between them. We can observe, as example, that the sample S4P25 exhibits almost half of the surface of the S1P25, but the catalytic performance of the first is better. A similar result is observed by adding as synthetized TiO₂ nanosheets and the surface of the sample with less titania have a higher surface, but it is less active in the degradation of MB. When NSNaOH is used, the surface slightly changes (15%) by increasing the titania content, but the remaining MB is the double when we use the lower concentration. Therefore, we can conclude that the nature of the TiO₂ nanoparticles and the loading determinates the photocatalytic activity. P25 contains a mixture of anatase and rutile phases in a ratio of about 3 and an average particle sizes of 85 and 25 nm, respectively. As it was described in chapter 4, the NS and NSNaOH samples consists on pure anatase TiO₂ with exposed {001} and an average size of 40 nm. It has been previously reported that the coexistence of rutile and anatase has a beneficial on the catalytic tests^(21,22). On the other hand, recent research using morphologically controlled TiO₂ nanoparticles demonstrates that anatase {001} facets are highly reactive^(23,24) in the oxidation of organic pollutants. The high density of surface undercoordinated Ti atoms on the {001} facets improve the reactivity for the dissociative adsorption of reactant molecules, such as water, methanol and formic acid, compared to the {101} facets⁽²⁵⁻³⁰⁾. In addition, theoretical calculations indicate the presence of large Ti–O–Ti bond angles at the surface, producing very reactive 2p states on surface oxygen atoms. Therefore, high photocatalytic efficiency is expected for anatase particles with large percentage of {001} facets⁽³¹⁾, though present information about their photocatalytic activity is still scarce and sometimes controversial. Our results show that the nanosheets with a high content of {001} facets exhibits a better catalytic performance than P25. If we compare the performance of P25 and the washed nanosheets (Figure 5.5), we can observe that the MB abatement is 4.5 times higher when washed nanosheets are used.

The effect of surface fluorination is also controversy, although it is commonly accepted that it affects the reactants adsorption, charge separation and transfer, and the kinetics and mechanism of surface photocatalytic reactions. Recent studies^(30,32,33) demonstrate that depending on the oxidation mechanism, the rate

of photocatalytic oxidation reactions may either increase or decrease by surface fluorination. In the literature we can find examples that indicate that fluorination improves the photocatalytic degradation of a number of simple organic compounds, such as phenol^(34,35), benzoic acid⁽³³⁾, cyanide⁽³⁶⁾ and also a variety of organic dyes^(30,33,37) in the aqueous media. This positive effect on the photocatalytic degradation was directly associated with a •OH radical-mediated mechanism, as demonstrated through spin trapping EPR experiments⁽³²⁾. However, a negative effect has been observed when the photocatalytic oxidation mainly occurs by direct interaction of the substrate with the holes photoproduced in the semiconductor valence band. The explanation was related to the hindered adsorption of the substrates on the fluorinated surface and hindered direct hole transfer⁽³⁸⁾. Our results suggest that the reaction mechanism corresponds with the latter option and implies the direct adsorption on the catalyst surface.

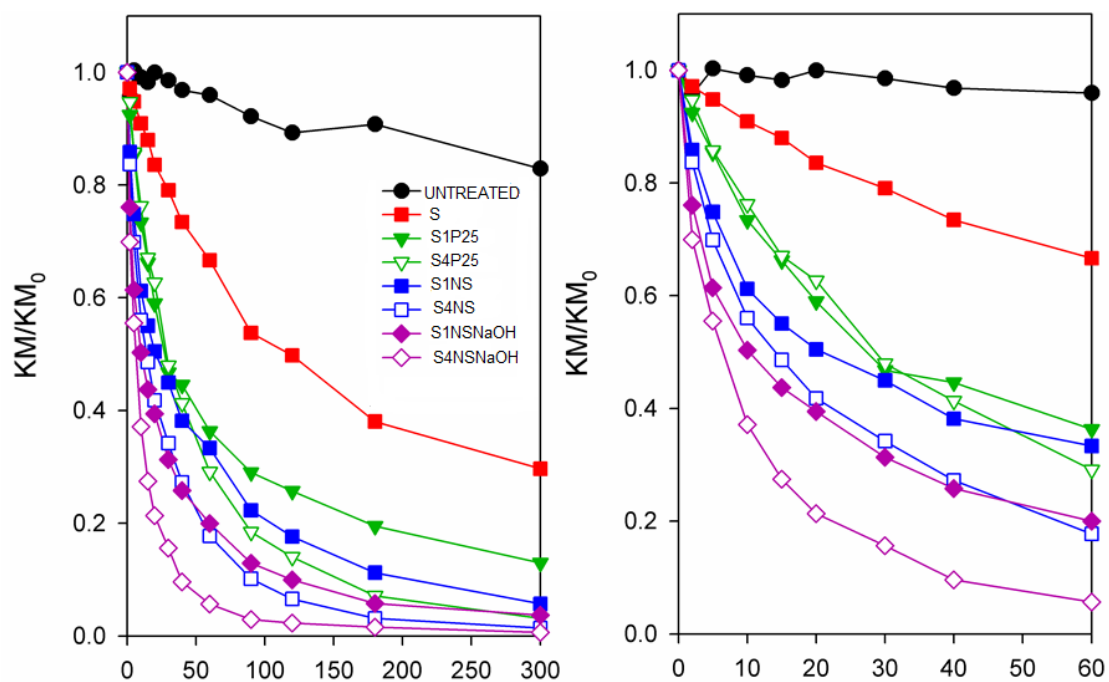


Fig. 5.5 KM/KM_0 over time for all the studied samples.

5.5 Kinetic models

The photo-degradation of dyes on solid surfaces has been theoretically postulated as a combination of first-order kinetic processes^(9,13,39). In this work, the evolution of methylene blue absorbance was proposed by a combination of two different first-order kinetics: A MB fraction was degraded in a fast process (Eq. 5.2) and the remaining MB was removed in a slower process (Eq. 5.3), and the total reaction rate was the addition of both processes (Eq. 5.4). In addition, we can obtain an expression (Eq. 5.5) that establishes a relationship between the initial concentration of MB degraded by each process and the total initial concentration of MB by using x as the MB fraction that degraded according to the slow process. Finally, using the Kubelka-Munk equation and considering that the parameter s (the surface scattering coefficient) was constant, we obtained equation 5.5 that characterizes the change of KM over time.

$$C_1 = C_{10} e^{-k_1 t} \text{ Eq. 5.2}$$

$$C_2 = C_{20} e^{-k_2 t} \text{ Eq. 5.3}$$

$$C = C_{10} e^{-k_1 t} + C_{20} e^{-k_2 t} \text{ Eq. 5.4}$$

$$\frac{C}{C_0} = \frac{KM}{KM_0} = (1 - x)e^{-k_1 t} + xe^{-k_2 t} \text{ Eq. 5.5}$$

Where k_1 is the speed constant for the MB degradation which occurs through relatively quick processes; k_2 is the speed constant for slow degradation processes; and x is the portion of MB that is degraded slowly. Table 5.3 presents the parameters, of each sample, for the kinetic model and the adjusting coefficient between the experimental data and the model, R^2 . Table 5.3 includes the results of applying this model to the KM/KM₀ curves included in Figure 5.5. We can observe an excellent adjustment to this model for all the data obtained in the case of all the treated samples. Only the untreated stone doesn't fit into the proposed equation.

Table 5.3 Parameters and adjusting coefficients for the kinetic model.

Sample	k ₁ (min ⁻¹)	k ₂ (min ⁻¹)	x	r ²
Untreated	0.00896	0.00044	0.94556	0.87427
S	0.01673	0.00212	0.54490	0.99728
S1P25	0.05533	0.00425	0.43244	0.99834
S4P25	0.04226	0.01012	0.45298	0.99894
S1NS	0.16270	0.00982	0.58814	0.99760
S4NS	0.21083	0.02027	0.62626	0.99922
S1NSNaOH	0.28351	0.01581	0.53359	0.99503
S4NSNaOH	0.32636	0.04157	0.52744	0.99604

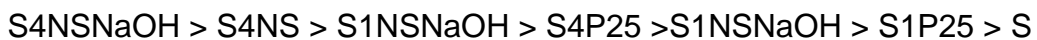
Based on the data in Table 5.3, we observe that both, k₁ and k₂ are strongly affected by the amount of titania nanoparticles and their nature. The value of k₁ and k₂ are higher when the samples are treated and specially when titania is added. Both parameter increase when the amount of titania is increased. The only exception is the value of k₁ when P25 is used. The portion of MB that is degraded through the slow reaction path, decrease from 0.99, in the case of the untreated sample, to 0.43-0.59 when the stone is treated. If we consider the effect of the nature, the order of both k₁ and k₂ values is the following:

$$\text{NS-NaOH} > \text{NS} > \text{P25}$$

5.6 Conclusions

The results included in this chapter demonstrates that titania nanosheets can be used to obtain SiO₂-TiO₂ sols with the adequate viscosity, gelation time and self-cleaning properties to be used as self-cleaning protective material. However, dispersing as synthetized nanosheets particles was difficult due to the high content of fluorine on the sample's surface. It is well known that fluorine on TiO₂ surface increases its hydrophobicity, leading to dispersion problems in hydrophilic solutions. This was corroborated by the characterization of the samples by STEM and the agglomeration of TiO₂ nanosheets was observed.

The obtained materials exhibit excellent photocatalytic properties and improves the results achieved with P25. The observed order in the self-cleaning activity of the synthetized products is the following:



We demonstrated that the surface fluorination negatively affects the photocatalytic activity and that the activity of the titania nanosheets increases after washing with NaOH.

References

1. Watanabe T, Nakajima a, Wang R, Minabe M, Koizumi S, Fujishima a, et al. Photocatalytic activity and photoinduced hydrophilicity of titanium dioxide coated glass. *Thin Solid Films*. 1999;351:260–3.
2. Xiaohong W, Zhaohua J, Huiling L, Xuandong L, Xinguo H. TiO₂ ceramic films prepared by micro-plasma oxidation method for photodegradation of rhodamine B. *Mater Chem Phys*. 2003;80(1):39–43.
3. Radeka M, Markov S, Lončar E, Rudić O, Vučetić S, Ranogajec J. Photocatalytic effects of TiO₂ mesoporous coating immobilized on clay roofing tiles. *J Eur Ceram Soc*. 2014;34(1):127–36.
4. Gherardi F, Colombo A, D'Arienzo M, Di Credico B, Goidanich S, Morazzoni F, et al. Efficient self-cleaning treatments for built heritage based on highly photo-active and well-dispersible TiO₂ nanocrystals. *Microchem J*. Elsevier B.V.; 2016;126:54–62.
5. Liu Q, Liu Q, Zhu Z, Zhang J, Zhang B. Application of TiO₂ photocatalyst to the stone conservation. *Mater Res Innov*. 2015;19(S8):S8-51-S8-54.
6. Moradzaman M, Mohammadi MR. Development of an aqueous TiO₂ paste in terms of morphological manipulation of nanostructured photoanode electrode of dye-sensitized solar cells. *J Sol-Gel Sci Technol*. Springer US; 2015;75(2):447–59.
7. Bergamonti L, Alfieri I, Lorenzi A, Predieri G, Barone G, Gemelli G, et al. Nanocrystalline TiO₂ coatings by sol???gel: photocatalytic activity on Pietra di Noto biocalcarenite. *J Sol-Gel Sci Technol*. 2015;75(1):141–51.
8. Quagliarini E, Bondioli F, Goffredo GB, Licciulli A, Munafò P. Smart surfaces for architectural heritage: Preliminary results about the application of TiO₂-based coatings on travertine. *J Cult Herit*. Elsevier Masson SAS; 2012;13(2):204–9.
9. Ollis D. Photocatalyzed and photosensitized conversion of organic dyes on porous and non-porous air-solid surfaces: Kinetic models reconsidered. *Appl Catal B Environ*. Elsevier B.V.; 2015;165:111–6.

10. Pinho L, Elhaddad F, Facio DS, Mosquera MJ. A novel TiO₂-SiO₂ nanocomposite converts a very friable stone into a self-cleaning building material. *Appl Surf Sci.* Elsevier B.V.; 2013;275:389–96.
11. Rao KVS, Subrahmanyam M, Boule P. Immobilized TiO₂ photocatalyst during long-term use: Decrease of its activity. *Appl Catal B Environ.* 2004;49(4):239–49.
12. Calia A, Lettieri M, Masieri M. Durability assessment of nanostructured TiO₂ coatings applied on limestones to enhance building surface with self-cleaning ability. *Build Environ.* Elsevier Ltd; 2016;110:1–10.
13. Mendoza C, Valle A, Castellote M, Bahamonde A, Faraldos M. TiO₂ and TiO₂-SiO₂ coated cement: Comparison of mechanic and photocatalytic properties. *Appl Catal B Environ.* 2015;178:155–64.
14. MacMullen J, Radulovic J, Zhang Z, Dhakal HN, Daniels L, Elford J, et al. Masonry remediation and protection by aqueous silane/siloxane macroemulsions incorporating colloidal titanium dioxide and zinc oxide nanoparticulates: Mechanisms, performance and benefits. *Constr Build Mater.* Elsevier Ltd; 2013;49:93–100.
15. Pinho L, Mosquera MJ. Titania-Silica Nanocomposite Photocatalysts with Application in Stone Self-Cleaning. *J Phys Chem C.* 2011 Nov 24;115(46):22851–62.
16. Zhu S, Liang S, Gu Q, Xie L, Wang J, Ding Z, et al. Effect of Au supported TiO₂ with dominant exposed {001} facets on the visible-light photocatalytic activity. *Appl Catal B Environ.* Elsevier B.V.; 2012;119–120:146–55.
17. Pinho L, Mosquera MJ. Photocatalytic activity of TiO₂-SiO₂ nanocomposites applied to buildings: Influence of particle size and loading. *Appl Catal B Environ.* 2013 May;134–135:205–21.
18. V.A. American Society of Civil Engineers. Concreep 10. 2015;10:877.

19. Thommes M, Kaneko K, Neimark A V., Olivier JP, Rodriguez-Reinoso F, Rouquerol J, et al. Physisorption of gases, with special reference to the evaluation of surface area and pore size distribution (IUPAC Technical Report). *Pure Appl Chem.* 2015;0(0):1051–69.
20. Mills A, Wang J. Photobleaching of methylene blue sensitised by TiO₂: an ambiguous system? *J Photochem Photobiol A Chem.* 1999;127(July):123–34.
21. Romero Ocaña I, Beltram A, Delgado Jaén JJ, Adami G, Montini T, Fornasiero P. Photocatalytic H₂ production by ethanol photodehydrogenation: Effect of anatase/brookite nanocomposites composition. *Inorganica Chim Acta.* 2015;431:197–205.
22. Beltram A, Romero-Ocaña I, Delgado Jaen JJ, Montini T, Fornasiero P. Photocatalytic valorization of ethanol and glycerol over TiO₂ polymorphs for sustainable hydrogen production. *Appl Catal A Gen.* 2015;
23. Yang HG, Sun CH, Qiao SZ, Zou J, Liu G, Smith SC, et al. Anatase TiO₂ single crystals with a large percentage of reactive facets. *Nature.* 2008 May 29;453(7195):638–41.
24. Ong W-J, Tan L-L, Chai S-P, Yong S-T, Mohamed AR. Highly reactive {001} facets of TiO₂-based composites: synthesis, formation mechanism and characterization. *Nanoscale.* 2014 Mar 21;6(4):1946–2008.
25. Lazzeri M, Vittadini A, Selloni A. Structure and energetics of stoichiometric TiO₂ anatase surfaces. *Phys Rev B - Condens Matter Mater Phys.* 2001;63(15):1554091–9.
26. Vittadini A, Selloni A, Rotzinger FP, Grätzel M. Structure and Energetics of Water Adsorbed at TiO₂ Anatase (101) and (001) Surfaces. *Phys Rev Lett.* 1998;81(14):2954–7.
27. Gong X, Selloni A. Reactivity of Anatase TiO₂ Nanoparticles : The Role of the Minority (001) Surface Reactivity of Anatase TiO₂ Nanoparticles : The Role of the Minority (001) Surface. *J Phys Chem B.* 2005;(1):1–4.

28. Arrouvel C, Digne M, Breysse M, Toulhoat H, Raybaud P. Effects of morphology on surface hydroxyl concentration: A DFT comparison of anatase-TiO₂ and γ -alumina catalytic supports. *J Catal.* 2004;222(1):152–66.
29. Herman GS, Dohnalek Z, Ruzycki N, Diebold U. Experimental investigation of the interaction of water and methanol with anatase-TiO₂(101). *J Phys Chem B.* 2003;107(12):2788–95.
30. Tilocca A, Selloni A. Methanol adsorption and reactivity on clean and hydroxylated anatase(101) surfaces. *J Phys Chem B.* 2004;108(50):19314–9.
31. Selloni A. Crystal growth: Anatase shows its reactive side. *Nat Mater.* 2008;7(8):613–5.
32. Mrowetz M, Selli E. Enhanced photocatalytic formation of hydroxyl radicals on fluorinated TiO₂. *Phys Chem Chem Phys.* 2005;7:1100–2.
33. Mrowetz M, Selli E. H₂O₂ evolution during the photocatalytic degradation of organic molecules on fluorinated TiO₂. *New J Chem.* 2006;30(1):108–14.
34. Minero C, Mariella G, Maurino V, Pelizzetti E. Photocatalytic Transformation of Organic Compounds in the Presence of Inorganic Anions. 1. Hydroxyl-Mediated and Direct Electron-Transfer Reactions of Phenol on a Titanium Dioxide–Fluoride System. *Langmuir.* 2000;16(6):2632–41.
35. Minero C, Mariella G, Maurino V, Vione D, Pelizzetti E. Photocatalytic transformation of organic compounds in the presence of inorganic ions. 2. Competitive reactions of phenol and alcohols on a titanium dioxide-fluoride system. *Langmuir.* 2000;16(23):8964–72.
36. Chiang K, Amal R, Tran T. Photocatalytic oxidation of cyanide: Kinetic and mechanistic studies. *J Mol Catal A Chem.* 2003;193(1–2):285–97.
37. Selli E. Effects of surface modification and doping on the photocatalytic activity of TiO₂. 2010;13(3):305–12.

38. Monllor-Satoca D, Gómez R, González-Hidalgo M, Salvador P. The “Direct-Indirect” model: An alternative kinetic approach in heterogeneous photocatalysis based on the degree of interaction of dissolved pollutant species with the semiconductor surface. *Catal Today.* 2007;129(1–2 SPEC. ISS.):247–55.
39. Chatterjee D, Patnam VR, Sikdar A, Joshi P, Misra R, Rao NN. Kinetics of the decoloration of reactive dyes over visible light-irradiated TiO₂ semiconductor photocatalyst. *J Hazard Mater.* 2008;156(1–3):435–41.

6. Conclusions

In the present work of thesis, the growth of the TiO₂ nanosheets with highly reactive {001} facets and TiO₂ nanorods was controlled by means of solvothermal and hydrothermal reactions. The main goal of the present work was the synthesis of TiO₂ nanomaterials with different morphologies and their enhancement of the photocatalytic performance by modification of their response in the visible spectrum through the use of Pt as co-catalyst and transition metals as dopants. As a result of the effective preparation and modification of TiO₂ nanostructures, the obtained TiO₂ nanomaterials are useful in different applications in heterogeneous catalysis. In this experimental work, the attention was set in two heterogeneous photocatalytic applications: H₂ production by ethanol photo-dehydrogenation under simulated solar light irradiation and the photocatalytic degradations of organic compounds deriving from environmental pollution.

In Chapter 3, highly crystalline anatase/brookite nanocomposites were successfully synthesized by hydrothermal treatment of Na-titanate precursor. In this study, the anatase/brookite ratio of the photocatalyst was modulated changing the synthetic parameters, such as precursor/water mass-to-volume ratio and time of the hydrothermal treatment. The Pt NPs photo-deposited as co-catalyst is affected by the multiphasic composition of the titania nanocomposites. The studies of the H₂ production under simulated solar irradiation revealed that the nanocomposites of anatase/brookite that present the smaller Pt NPs have the higher photoactivity. This result was found to be related with a better electron-hole separation in this multiphasic nanocomposites. The photoactivity of the anatase/brookite nanocomposites was compared with a reference samples synthesized by a conventional sol-gel method concluding that our synthesized nanocomposites showed a higher H₂ production normalized to the surface area.

Following with the experimental work carried out in the present thesis, in Chapter 4 highly crystalline TiO₂ anatase nanosheets were synthesized with

controlled morphology and metal doping, accompanied by a detailed study with several chemical and morphological characterization techniques of the TiO₂ nanosheets. The mains goals of this chapter were the study of the influence of transition metals as dopants on TiO₂ nanosheets and the influence of the fluorine ion adsorbed during the synthesis reaction on the nanosheets surfaces evaluating the H₂ photocatalytic production under simulated solar irradiation. It was found an undeniable effect on photocatalytic activity of the fluorine ions. The presence of fluorine ions in the TiO₂ nanosheets has a positive effect in the photocatalytic activity in the absence of transition metal as dopant on titania nanomaterial. It was observed that the photocatalytic H₂ production was affected when the fluorine ions and transition metal are present in the TiO₂ nanosheets.

The influences of the transition metals as dopants vary according to the chemical element. For Mn, Ni and Co a positive effect in the H₂ production by ethanol dehydrogenation reaction was found but for the TiO₂ nanosheets doped with Fe, the effect in the photocatalytic activity was detrimental. Continuing with the conclusions of this chapter, we cannot fail to mention the difficult to doped the TiO₂ nanosheets with transitions metals. ICP-AES analysis revealed that the real amount of dopants was far from nominal amount. This highlighted the difficult to introduce the transition metals into TiO₂ lattice. This complexity to dissolve the transition metals into TiO₂ lattice is due to the high crystallinity of the TiO₂ nanosheets. For future works, it is necessary to develop new routes for doping in order to increase the presence of the dopants into TiO₂ lattice and to further improve the photocatalytic activity of this type of photocatalyst. In this way, the future work in this field could help to understand what is the effect of the different transition metals on the TiO₂ nanosheets and be able to modulated the photocatalytic response of this type of nanomaterials.

In Chapter 5, the potential use of TiO₂ nanosheets synthesized in Chapter 4 was studied as a component of nanocomposites with active photocatalytic self-cleaning properties. An effective synthesis method was developed for producing titania-silica nanocomposite coatings for stone conservation by self-cleaning. Composite coatings were prepared by dispersion of TiO₂ nanosheets in a mesoporous silica matrix in the presence of a non-ionic surfactant (n-octylamine). Sol-gel transition occurs spontaneously, producing an

effective nanocomposite coating on the building stone. For comparison, another set of photocatalytic commercial materials was also tested. The obtained materials exhibit excellent photocatalytic properties and improves the results achieved with commercial Degussa P25. Finally, was demonstrated as in the studied case on Chapter 4, that the surface fluorination negatively affects the photocatalytic activity and that the activity of the titania nanosheets increases after washing with NaOH.

It is right to conclude that the design of TiO₂ morphologies provides suitable nanomaterials for maximizing the photocatalytic efficiency with respect common TiO₂ nanomaterials. In this work of thesis, we have highlighted TiO₂-based photocatalysts with well-defined morphology (nanorods and nanosheets) and with Pt as co-catalyst (Chapter 3 and Chapter 4) and doped with transition metals (Chapter 4) that significantly contribute to improve the performance in important photocatalytic process in photocatalysis, such as light absorption in the visible region, the electron-hole recombination rate, high surface area, and enhanced light harvesting. The doping and heterostructuring plays a critical role in improving the kinetics of the charge carriers, that is, the separation of electrons and holes pairs, and the extension of light absorption to visible light region, thereby enhancing the photoefficiency of TiO₂ nanomaterials.

In conclusion, the results of this experimental work was to provide a comprehensive background of TiO₂ photocatalysts with controlled morphology and a study for structural design of nanoscale catalysts for solar-to-fuel conversion purposes and to produce clean and renewable fuel and environmental remediation.

ACKNOWLEDGEMENTS

First of all, my sincere thanks to my dear mentors, Prof. Paolo Fornasiero for give me the opportunity to enjoy this exciting PhD thesis in his group. Thanks for your guidance in this years. I would also like to express my thanks to Dr. Tiziano Montini, this thesis work it would never have been possible without your guidance and help during all the period of the thesis, from minute one to the last second. Last but not least, all my gratitude to Dr. Juán José Delgado from University of Cádiz, I have learned important things by your side.

Secondly, I would like to express my gratitude to my co-workers at the University of Trieste, Dr. Valentina Gombac, Dr. Miquele and Matteo Monai. I would particularly like to express appreciation of the efforts made by Alessandro Bertran helping me in the experiments. Many thanks to all of you.

Third, I would like to thank to all my co-workers and technicians of the SCCYt at the University of Cádiz (Spain) for your help and for the good time that we spend together. Specially thanks to my dear co-workers J.J. Relinque for all your help and coffees that we have taken together and to Daniel Goma. My special thanks to Susana Fernandez for to encourage me every day.

And finally I would like to express some words in my mother language to my family. Papá, gracias por haberme inculcado el amor por los libros desde pequeño y enseñarme la importancia del esfuerzo y la constancia, si hoy he llegado aquí es por ti. Mama, gracias por haberme enseñado a caminar por la vida, por levantarme del suelo cuando era un niño y aprendía andar y por levantarme en la vida y no dejarme caer cuando me he tropezado, gracias. Gracias a mis hermanos Javi, Iván y Dani por ser los mejores amigos que un hermano pueda tener. Gracias a Lorena Martos Santamarta, por tu apoyo económico y moral, “porque la vida da vueltas, pero sabe lo que hace”.

Y por último gracias a mi pequeña Milagrosita, eres mi razón de ser, eres mi vida.

Publications in the PhD period

- 1.- **Romero Ocaña, I.**, Beltram, A., Delgado Jaén, J.J., Adami, G., Montini, T., Fornasiero, P. "Photocatalytic production by ethanol photodehydrogenation: Effect of anatase/brookite nanocomposites composition" **Inorganica Chimica Acta**, 431, (2014) pp. 197-205
- 2.- Cecconi, B., Manfredi, N., Ruffo, R., Montini, T., **Romero-Ocaña, I.**, Fornasiero, P., Abbotto, A. "Tuning Thiophene-Based Phenothiazines for Stable Photocatalytic Hydrogen Production" **ChemSusChem**, 8 (24), (2015) pp. 4216-4228
- 3.- Manfredi, N., Cecconi, B., Calabrese, V., Minotti, A., Peri, F., Ruffo, R., Monai, M., **Romero-Ocaña, I.**, Montini, T., Fornasiero, P., Abbotto, A. "Dye-sensitized photocatalytic hydrogen production: Distinct activity in a glucose derivative of a phenothiazine dye" **Chemical Communications**, 52 (43), (2016) pp. 6977-6980.
- 4.- Montini, T., Monai, M., Beltram, A., **Romero-Ocaña, I.**, Fornasiero, P. "H₂ production by photocatalytic reforming of oxygenated compounds using TiO₂-based materials" **Materials Science in Semiconductor Processing**, 42, (2016) pp. 122-130.
- 5.- Beltram, A., **Romero-Ocaña, I.**, Josè Delgado Jaen, J., Montini, T., Fornasiero, P. "Photocatalytic valorization of ethanol and glycerol over TiO₂ polymorphs for sustainable hydrogen production" **Applied Catalysis A: General**, 518, pp. (2016) 167-175.
- 6.- Naldoni, A., Montini, T., Malara, F., Mróz, M.M., Beltram, A., Virgili, T., Boldrini, C.L., Marelli, M., **Romero-Ocaña, I.**, Delgado, J.J., Dal Santo, V., Fornasiero, P. "Hot Electron Collection on Brookite Nanorods Lateral Facets for Plasmon-Enhanced Water Oxidation". **ACS Catalysis**, 7 (2), (2017) pp. 1270-1278.

Works presented in congresses and specialized events

1. “**Contribution of Electron Microscopy to the characterization of ceria based catalysts**”, J.J.Delgado ;T.Montini ;S. Collins ;X. Chen ;A. Bonivardi ;H. Pan ;J.J. Calvino ;E. Del Río ;M. López-Haro ;**Ismael Romero-Ocaña** ;P. Fornasiero, **General Meeting Cost Action Reducible oxides, European Cooperation in Science and Technology**, Barcelona (Spain) (2014) .
2. “**Exceptional activity for methane oxidation with catalysts prepared by modular assembly of subunits**” M. Cargnello ;J. J. Delgado Jaén ;J. C. Hernández Garrido ;**Ismael Romero-Ocaña** ;K. Bakmutsky ;T. Montini ;J. J. Calvino Gamez ;R. J. Gorte ;P. Fornasiero. **Advanced Electron Microscopy for Catalysis and Energy Storage Materials, Department of Inorganic Chemistry, Fritz Haber Institute of the Max Planck Society**, Munich, Alemania. (2015).

